UNIVERSIDAD DE CONCEPCIÓN
FACULTAD DE CIENCIAS FÍSICAS Y MATEMÁTICAS
DOCTORADO EN CIENCIAS FÍSICAS

EMISSION LINE STARS IN LOW METALLICITY ENVIRONMENTS

Autor

HERNÁN ENRIQUE GARRIDO VERTEL

Tesis para optar al grado académico
de Doctor en Ciencias Físicas

Profesor Guía

Dr. RONALD MENNICKENT CID

Profesor Co-Guía

Dr. CHRISTOPHE MARTAYAN

CONCEPCIÓN - CHILE
NOVIEMBRE 2015

UNIVERSIDAD DE CONCEPCIÓN
FACULTAD DE CIENCIAS FÍSICAS Y MATEMÁTICAS
DOCTORADO EN CIENCIAS FÍSICAS

EMISSION LINE STARS IN LOW METALLICITY ENVIRONMENTS

Autor

HERNÁN ENRIQUE GARRIDO VERTEL

Tesis para optar al grado académico
de Doctor en Ciencias Físicas

Profesor Guía

Dr. RONALD MENNICKENT CID

Profesor Co-Guía

Dr. CHRISTOPHE MARTAYAN

CONCEPCIÓN - CHILE
NOVIEMBRE 2015

"Como no estás experimentado en las cosas del mundo, todas las cosas que tienen algo de dificultad te parecen imposibles. Confía en el tiempo, que suele dar dulces salidas a muchas amargas dificultades".

—Don Quijote de la Mancha

Acknowledgments

Cuando se esta al final de un proyecto de muchos años y esfuerzos, a menudo es interesante mirar hacia el pasado y hacer un balance del camino recorrido, antes de mirar hacia delante para volver a retomar el viaje hacia un futuro cercano. Al hacer una reflexión de este tipo te das cuenta que el viaje en realidad no fue tan largo, gracias a muchos lugares y personas que hoy quiero agradecer, en primer lugar a las tierras Cordobesas y sus cálidos atardeceres desbordados de alma. Este mágico lugar construyo en mi vida un doble tiempo, desde aquí viví, soñé y aprendí a pintar la locura en un retrato. Mi boca aprendió a imitar el vuelo de garzas blancas sobre el valle donde corre el río, en este lugar mi sonrisa reflejó un peligroso corazón que siempre guarda la fragilidad de un niño. Nacer en el Caribe es lo más grande que me ha pasado en la vida, no sólo por sus tradiciones y cultura, sino también por estas letras que siempre siento tan mías. Lo más grande no es ser poeta o científico, lo más grande es ser Caribe. Pedazo de encanto es la perla del Sinú, tierra que me llama y me hechiza el alma. Ella es sólo un pedazo infinito del mundo, la tierra Caribe del poeta, orgulloso me siento de esta tierra mágica que me vio nacer.

Volviendo a estos orígenes en primer lugar quisiera agradecer en este bello lugar a mi Padre y a mi Madre querida que un 10 de Octubre además de parir un río caudaloso, también dio a luz un hijo. Ella me ha acompañado durante 30 años en este viaje y me enseño entre sus manos, que los poemas son artificios menos diabólicos cuando se les atribuye un dueño. Adicionalmente, ella me brindo los primeros instrumentos con los cuales vería explotar el universo lleno de colores y de nostalgias, con ellos he vivido los minutos de claridad que pasan entre los años de oscuros racionamientos, estas instantáneas han sido siempre agujas frías que atraviesan el tiempo. Sin estos ojos, las siguientes 100 páginas jamás hubieran sido escritas, ni imaginadas, por eso hay que agradecerlas a ella. Por otra parte, agradecer a mi hermana por sus años de compañía en Colombia y Chile, también dejarle constancia en estas letras, que el éxito de un gran sueño, siempre se alcanza con mucha paciencia y siempre con un pie muy temprano fuera de la cama.

En el Caribe Colombiano, me gustaría aprovechar esta oportunidad para agradecerles a mis primeros forjadores en ciencias, los cuales jugaron un papel importante y decisivo en la enseñanza de la Física en la Universidad de Córdoba, sin duda alguna entre ellos muy especialmente agradecerle al Dr. Roger Maya Taboada por despertar en mi el placer por la Astronomía y también por ser el dador del segundo instrumento a través del cual el universo se expandía un poco más ante mis ojos.

En la capital del país a mis amigos incondicionales: Edilberto Suáres Torres, Alfonso Rodríguez, Zyren Cordero Kerguelen, Diana Rojas, Gloria Rojas, John Fabio Aguilar y a todas las personas que constituyen un pequeño hogar llamado Observatorio Astronómico Nacional en la Universidad Nacional de Colombia, sin todos ustedes esto tampoco hubiera sido posible.

Quisiera agradecer a muchas personas e instituciones que brindaron todo su apoyo para mí crecimiento académico y personal entre ellos: A mis directores y mis mentores los Doctores Ronald Mennickent Cid, Christophe Martayan, Dietrich Baade, Maja Vuckovic, Javier Rodón, Linda Schmidtobreick, Willem-Jan de Wit, Thomas Rivinius, y Stan Stefl (Q.E.P.D), por ser los inspiradores de grandes ideas y motivadores de excelentes preguntas. Además de ser maestros, son amigos y los pilares siempre para mirar y volar más alto.

A mis colaboradores, en especial a Gojko Djurašević por la aplicación de sofisticados modelos a las curvas de luz de las estrellas binarias en esta tesis, a Sandro Villanova por la determinación de abundancias para ELHC 10, a Z. Kołaczkowski y Dareck Graczyk por llevar a cabo parte de las observaciones usadas en esta investigación. A Eva Niemczura por proveer la grilla de espectros sintéticos para estrellas calientes, N. Mennekens por proporcionar la grilla de modelos evolutivos para estrellas binarias y a Joanne Dawson por facilitarme las máscaras de las super burbujas en la LMC.

A mis compañeros de Doctorado en la UDEC y a mis amigos del Observatorio Europeo Austral por todas sus sonrisas, discusiones académicas y amistad entre ellos especialmente a: Francesco Mauro, Reneé Mateluna, Daniela Barría, Emerson Tenorio, Diego Molina, Marcelo Ipinza, Gustavo Orellana, Roy Slater, Gustavo Aguayo, Amy Tyndall, Florian Gourgeot, Vera Patrício, Matt Shultz, Loredana Lovisi, Bruno Dias, Matías Jones, Jens-Kristian Krogager, Taehyun Kim, Joanne Breitfelder, Myriam Rodrigues, Andrea Mehner, Kora Muzic, Fernando Selman, George Hau, Valentina Rodríguez, Rebeca Aladro, Julien Girard, Claudio Melo, Dave Jones, Giovanni Carraro, Sergio Martin Ruiz, Emanuela Pompei, Dimitri Gadotti, Steffen Mieske, Esteban Osorio, Gustavo Hahn, Basilio Kublik y Valentin Christiaens.

A esas personas que han sido importantes en cada uno de mis días de verano ó invierno en Chile y que son parte especial en mi corazón entre ellos muy especialmente a: Marcela Sanhueza, Marllory Fuentes, Victor Mora, Ruth Sandoval, Ricardo Caroca, Soledad Daroch, Cynthia Rojas, Ronald Burgos, Libertad Manque, María José Jerez y a todos aquellos que no he nombrado y que directa o indirectamente hicieron posible este trabajo.

Esta tesis Doctoral fue posible gracias al soporte económico entregado por el Studentship Programme del Observatorio Europeo Austral (ESO), así como de los proyectos FONDECYT 1110347 y BASAL Centro de Astrofísica y Tecnologías Afines (CATA) PFB- 06/2007.

A todos infinitas gracias y nos vemos en un futuro cercano.

Hernán Enrique Garrido Vertel

Octubre 10 de 2015, Concepción-Chile.

Abstract

The Large Magellanic Cloud (LMC) is an excellent laboratory to study the stellar evolution and the ongoing stellar formation in low metallicity environments. Its distance is relatively well known and there is only a small interstellar extinction toward the LMC.

We present in this thesis the observational study of a sample of Emission-line stars (ELSs) in the LMC, for which we examine star formation episodes associated with advancing ionization fronts and expanding supergiant shells (SGSs) in local and larger scales.

SGSs are the largest and most energetic shells in the LMC, and are therefore expected to have a dramatic effect on the Interestellar Medium (ISM). Their regions of influence are large enough to accumulate the amount of material needed for molecular cloud formation. On the other hand, the cumulative energy input from stellar winds, supernovae, and ionizing radiation is able to form molecular clouds via the accumulation, compression, and cooling of the interstellar medium in giant ($100 \sim 1000$ pc) supershells around OB clusters. Thus, advancing ionization fronts and expanding supergiant shells or giant shells compress nearby clouds, increasing their density and causing the collapse of deeply embedded cores, leading to new star formation.

In this thesis, we investigate this issue in the open cluster NGC 1850 and within its vicinity. Here, we found a possible relationship between the location of ELS and the ionized gas structures with the SGS complex. In addition to this and to make a more relevant study on this hypothesis and to determine the influence of SGS on new star-formation and evolutionary stage of these stellar populations, we used the instrument Wide Field Imager (WFI) in its slitless spectroscopic mode, as well as photometry from different database in order to identify the Hα emission-line objects (from low to high mass, not evolved to evolved) in the LMC star-formation region NGC 1850 and its surrounding field. In this region 64 Hα emission-line stars were identified and these ELS are concentrated inside or around the SGS borders.

We present the results of a detailed spectroscopic and photometric study of two cases of interacting binaries in the LMC bar, including the analysis of high-resolution spectra and the application of a sophisticated light curve model for the systems.

In the first case, new high-resolution spectroscopic data were obtained for OGLE 05155332−6925581, one of the brightest members in the LMC of the enigmatic group of the Double Period Variables (DPV). We found that the system is best modelled with a geometrically thin and optically thick disc around the primary star. The analysis of the photometric data has allowed us to derive improved orbital parameters and stellar parameters for this DPV system. Taking advantage of our new and improved system and stellar parameters, we explored the evolutionary stage of OGLE 05155332−6925581 with the aid of published grids of evolutionary routes for binary systems of similar masses, considering conservative and non-conservative evolution. A comparison with these synthetic binary-star evolutionary models indicates that the system has an age of 4.76×10^7 yr, and is in the phase of rapid mass transfer, the second one in the life of this binary. This evolutionary stage is consistent with the existence of the circumprimary accretion disc found for the system, but the model that best fits the observations shows the system with a relatively large mass transfer rate of $\dot{M} = 3.1 \times 10^{-6}$ M$\odot$ yr^{-1}. However,

the orbital period remains relatively stable during almost 15 yr. We speculate that outflows could be extracting angular momentum from the system, keeping constant the orbital period. Furthermore, we show that under certain conditions of mass and angular momentum loss, the system orbital period can be kept constant even in high mass transfer rate regimes.

In the second case, we establish the true nature of the luminous star ELHC 10, concluding that it is a long-period eclipsing binary composed of a post-asymptotic giant branch (post-AGB) star showing signatures of s-process nucleosynthesis, and an unseen early B-type stellar companion surrounded by an eclipsing circumstellar disc. Additional to this, we discovered line splitting of metallic lines in ELHC 10, characterized by discrete absorption components observed alternatively at the blue and red side of the photospheric line profiles during the orbital cycle, which can be interpreted as evidence for gas streams, leading to the formation of a circumstellar disc and a circumbinary disc in the system. Our study provides evidence that circumbinary discs can be formed by binary star interaction and outflows in post-AGB stars. It also suggests that low-mass post-AGB stars can be formed by an evolutionary channel different from single stars, specifically by depletion of an initially massive star by mass transfer in a semi-detached binary system.

As a result of this thesis, three papers were produced, one of them is already published “Physical parameters and evolutionary route for the Large Magellanic Cloud interacting binary OGLE 05155332−6925581”, one has been submitted “The complex eclipsing binary ELHC 10 to post-AGB candidate in the Large Magellanic Cloud” and other is in the final stage of preparation “The LMC NGC 1850 region history: Emission-line stars as tracers of stars formation episodes.”

Resumen

La Gran Nube de Magallanes (LMC) es un excelente laboratorio para estudiar la evolución estelar y la formación estelar en curso en ambientes de baja metalicidad. Ya que su distancia es relativamente bien conocida, sólo hay una pequeña extinción interestelar hacia la LMC.
Se presenta en esta tesis el estudio observacional de una muestra de estrellas con líneas de emisión (ELS) en la LMC, para la cual examinamos episodios de formación estelar asociados con el avance de frentes de ionización y la expansión de super burbujas (SGS) a escala local y grandes escalas.
SGS son las burbujas más grandes y más energéticas de la LMC, y por lo tanto se espera que tenga un efecto dramático en el medio interestelar. Sus regiones de influencia son lo suficientemente grandes para acumular la cantidad de material necesario para la formación de nubes moleculares. Por otro lado, la energía acumulada desde los vientos estelares, supernovas, y la radiación ionizante es capaz de formar nubes moleculares a través de la acumulación, compresión y enfriamiento del medio interestelar en super-burbujas gigantes (100 $\sim$ 1000 pc) alrededor de cúmulos OB. Así, el avance de los frentes de ionización y la expansión de super-burbujas o burbujas gigantes comprimen nubes cercanas, aumentando su densidad y causando el colapso de núcleos profundamente integrados, conduciendo a la formación de nuevas estrellas. En esta tesis, abordamos este problema en el cúmulo abierto NGC 1850 y sus alrededores. Aquí, encontramos una posible relación entre la localización de las ELS y las estructuras de gases ionizados con el complejo de SGS. Además de esto hacemos un estudio más relevante de esta hipótesis y determinamos la influencia de la SGS sobre la nueva formación estelar y el estado evolutivo de esta población estelar, hemos usado la cámara de ancho campo (WFI) en modo espectroscópico slitless y fotometría de diferentes bases de datos con el fin de identificar objetos con emisión en línea Hα (desde baja a alta masa, no evolucionado a evolucionado) en la región de formación estelar LMC NGC 1850 y alrededor de su campo. En esta región 64 estrellas con línea de emisión en Hα fueron identificadas y están concentrandas en el interior o alrededor de los bordes de la SGS.
Presentamos también el detallado estudio de dos sistemas binarios interactuantes en la barra de la LMC, incluyendo el análisis de espectros de alta resolución y la aplicación de un sofisticado modelo de curva de luz para los sistemas.
En el primer caso, nuevos datos espectroscópico de alta resolución fueron obtenidos para OGLE 05155332−692558, uno de los miembros más brillantes en la LMC del enigmático grupo de las variables de doble período (DPV). Se encontró que el sistema es mejor modelado con un disco geométricamente delgado y ópticamente grueso alrededor de la estrella primaria. El análisis de los datos fotométricos nos ha permitido derivar mejores parámetros orbitales y parámetros estelares para este sistema DPV. Aprovechando nuestro nuevo y mejorado sistema y los parámetros estelares, exploramos la etapa evolutiva de OGLE 05155332−692558 con la ayuda de grillas publicadas de rutas evolutivas para sistemas binarios de masas similares, considerando evolución conservativa y no conservativa para el sistema. Una comparación con estos modelos evolutivos sintéticos para estrellas binarias indica que el sistema tiene una edad de 4.76×10^7 años, y está en fase de rápida transferencia de masa, la segunda en la vida de esta binaria. Esta etapa evolutiva es consistente con la existencia del disco

de acreción circumprimario encontrado para el sistema, pero el modelo que mejor ajusta las observaciones muestra el sistema con una tasa de transferencia de masa relativamente grande de $\dot{M} = 3.1 \times 10^{-6}$ M$\odot$ yr^{-1}. Sin embargo, el período orbital permanece relativamente estable durante casi 15 años. Por ende, especulamos que flujos salientes podrían estar extrayendo momento angular del sistema, manteniendo constante el período orbital. Además, se muestra que bajo ciertas condiciones de pérdidas de masa y momento angular, el período orbital del sistema puede mantenerse constante incluso en regímenes de alta transferencia de masa.

En el segundo caso, se establece la verdadera naturaleza de la estrella luminosa ELHC 10, concluyendo que es una binaria eclipsante de largo período compuesta por una estrella gigante localizada en el diagrama HR después de la rama gigante (post-AGB) que muestra señales de procesos lentos de captura de neutrones (procesos-S), y una compañera estelar invisible de tipo B temprano rodeado de un disco circunestelar eclipsante. Adicional a esto, descubrimos líneas metálicas con extra-componentes en ELHC 10, caracterizadas por componentes de absorción discretas observadas alternativamente en el lado azul y rojo de los perfiles de línea fotosféricos durante el ciclo orbital, lo cual puede interpretarse como evidencia de corrientes de gas, las cuales conducen a la formación de un disco circumstellar y otro disco circumbinario en el sistema. Nuestro estudio proporciona evidencia de como discos circumbinarios pueden formarse por la interacción de estrellas binarias y outflows en estrellas post-AGB. También sugiere que estrellas post-AGB de baja masa pueden formarse por un canal evolutivo diferente a estrellas individuales, específicamente por la reducción por trasferencia de masa de una estrella inicialmente masiva en un sistema binario semi-separado.

Como resultado de esta tesis, tres papers fueron producidos, uno de ellos ya fue publicado “Physical parameters and evolutionary route for the Large Magellanic Cloud interacting binary OGLE 05155332−6925581”, el segundo ya fue enviado para su aprobación “The complex eclipsing binary ELHC 10 to post-AGB candidate in the Large Magellanic Cloud” y el tercero se encuentra en fase final de preparación “The LMC NGC 1850 region history: Emission-line stars as tracers of stars formation episodes.”

Contents

List of Figures

List of Tables

Chapter 1

Introduction

Stars with emission lines in their spectrum are present everywhere in the HR diagram. Among them, one can find evolved and unevolved objects such as Wolf-Rayet stars (WR), Luminous Blue Variables (LBV), Herbig Ae/Be star (HAeBe), T Tauri (TTau), massive and low-mass objects like Classical Be stars (cBe), M flare stars, Post-Asymptotic giant branch (post-AGB stars), etc. The emission lines usually arise from the stellar wind (e.g. O stars, B[e] stars), and/or from the circumstellar material: accretion (HAeBe stars), decretion disk (cBe stars), or envelope created during an eruption (LBV, B[e] stars) (Lamers et al. 1999; van Winckel 2003; Rivinius et al. 2013).

On the other hand, at low metallicity, typically in the Magellanic Clouds, OB type stars rotate faster than their counterparts in the Milky Way (MW). This has consequences, such as modifying the stellar evolution of some stars and their appearance. It was noticed that there are more classical Be stars in the L/SMC than in the MW, the more massive ones appearing at a different stage than in the MW. Due to the very fast rotation kept during the evolution (only possible at low metallicity due to the lower efficiency of the stellar radiatively driven winds and to the corresponding lower angular momentum loss), it seems that the massive stars can follow the quasi chemically homogeneous evolution (Maeder 1987; Yoon et al. 2006) instead of the usual way of standard evolution, especially in the SMC. Martins et al. 2009 indicated that several SMC WR properties could be explained by such evolution. It is possible that due to such special stellar evolution some of those stars could finish their life in a gamma ray burst (Yoon et al. 2006; Martayan et al. 2010c). However, if the stars follow the usual way to evolve, in particular in the LMC, the metallicity of the evolved stars (supergiant, LBV, etc) should be higher than solar (Maeder & Meynet 2001). If the stars are not binaries, with the stellar parameters and the current chemical composition, one could be able to determine which stellar/chemical evolution these stars follow at different metallicity regimes.

Additionally in this thesis we studied two important cases of peculiar emission-line stars (ELSs) in the LMC. In the first, we have obtained indirect evidence, suggesting non-conservative evolutions in Double Period Variables (DPVs) and we have speculated that systemic angular-momentum losses (and thus mass losses) must be involved to reproduce the current state of some observed DPV systems. This hypothesis is consistent with the presence of the disc-like and spiral-like features found in these systems. In the second case, we found observational evidence that circumstellar material is completely or partly, trapped in a stable, circumbinary or circumstellar disc. The orbital parameters found, imply that a strong interaction between both components took place in the system.

In the following pages we summarize some theoretical aspects and open questions which will be developed in detail in later chapters.

1.1 Effects of the Massive Stars on Star formation

Star formation is one of the most important astrophysical processes, but because it takes place on small physical scales and behind heavy optical darkening, observations of its early phases have generally been limited to the Milky Way (MW). Recent studies have focused on studying how star formation started and propagated in the Small Magellanic Cloud (SMC) and the Large Magellanic Cloud (LMC), studying both the young cluster and field population (e.g., Meschin et al. 2014; Cignoni et al. 2011; Hennekemper et al. 2008). It appears that the LMC went through recent episodes of star formation 2 Gyrs, 500 Myrs, 100 Myrs, and 12 Myrs ago according to Harris & Zaritsky (2009). In the LMC only few open clusters are studied in detail regarding the aforementioned aspect. The starburst region 30 Doradus (NGC 2070) in the LMC is one example of a star forming region with unusual stellar-mass and spatial segregation: more massive and evolved stars are found in the outer parts of the region (Selman et al. 1999; Evans et al. 2011). However, this region is quite difficult to interpret due to possible cluster interactions that may have led to various star formation episodes and mixed populations (Sabbi et al. 2012; Dufton et al. 2013).

In this thesis, we will explore systematically a way in which the star formation can be propagated in LMC by means of ionization fronts, which are produced by multiple supernova explosions, occurring in a quasi-continuous manner over the entire epoch. A single giant molecular cloud survives for the required length of time and could develop numerous sites of massive star formation over this period to lengthen their extent and interaction zones. So, the star formation in the LMC can be around the large shell structures with sizes approaching 1 kpc. These supergiant shells (SGSs) or giant shells (GSs) are thought to be forming also, due to the mechanisms described previously, fast stellar winds and supernova explosions of multiples generations of massive stars. A supernova explosion in the galactic disc, for example, creates a hot ($T \gtrsim 10^6$ K) cavity of low-density ($n \lesssim 10^{-2}$ cm^{-3}) coronal gas that may persist for $\gtrsim 10^6$ yr, much longer that the time scale $\sim 3 \times 10^4$ yr for which the remnant is visible in radio or optical ranges. Cox & Smith (1974) recognized that these cavities would persist for times more that about 10^6 yr and therefore might occupy a significant fraction of the galactic disc volume, ideas that were developed in quantitative theories by McKee & Ostriker (1977) and then by McCray & Kafatos (1987).

Therefore, the expansion of an SGS can shock and sweep up interstellar gas, altering the physical conditions and distribution of the Interestellar Medium (ISM). As a result or consequence of this, SGS may puncture the galactic gas disc and vent hot gas into the galactic halo, while its expansion in the galactic disk can compress ambient gas, thus the gravitational instability of the SGS or GS provides a physical mechanism for induced star formation and may account for bursts of star formation, especially in irregular galaxies, where spiral density waves are not produced.

Elmegreen (1998), suggested two methods in which star formation can be triggered in SGS due to their expansion. First, when the SGS expands, it sweeps up and collects the ambient ISM in its shell, and when the dense shell gas cools, it may become gravitationally unstable and collapse to form stars, as has been mentioned before or alternatively, the shock fronts may also contribute to the random, turbulent structure of the ISM in the galaxies. Such motions may compress pre-existent dense clouds around its edge, causing these clouds to collapse and maintaining pressure equilibrium between different ISM phase. With this in mind and due to the proximity of the LMC (49.97 ± 0.19 kpc, Pietrzyński et al. 2013), Kim et al. (1998, 1999) surveyed the LMC in H I at high spatial resolution with the Australia Telescope Compact Array (ATCA) and catalogued many H I holes and supergiant shells in the ATCA map. She found good association between H I and H II regions, and some evidence for regions of star formation providing direct mechanical input into the expansion of the shells and, therefore, the evacuation of the H I supergiant shell.

Meanwhile, Yamaguchi et al. (2001a,b) studied the effect of the SGSs on the formation places of molecular

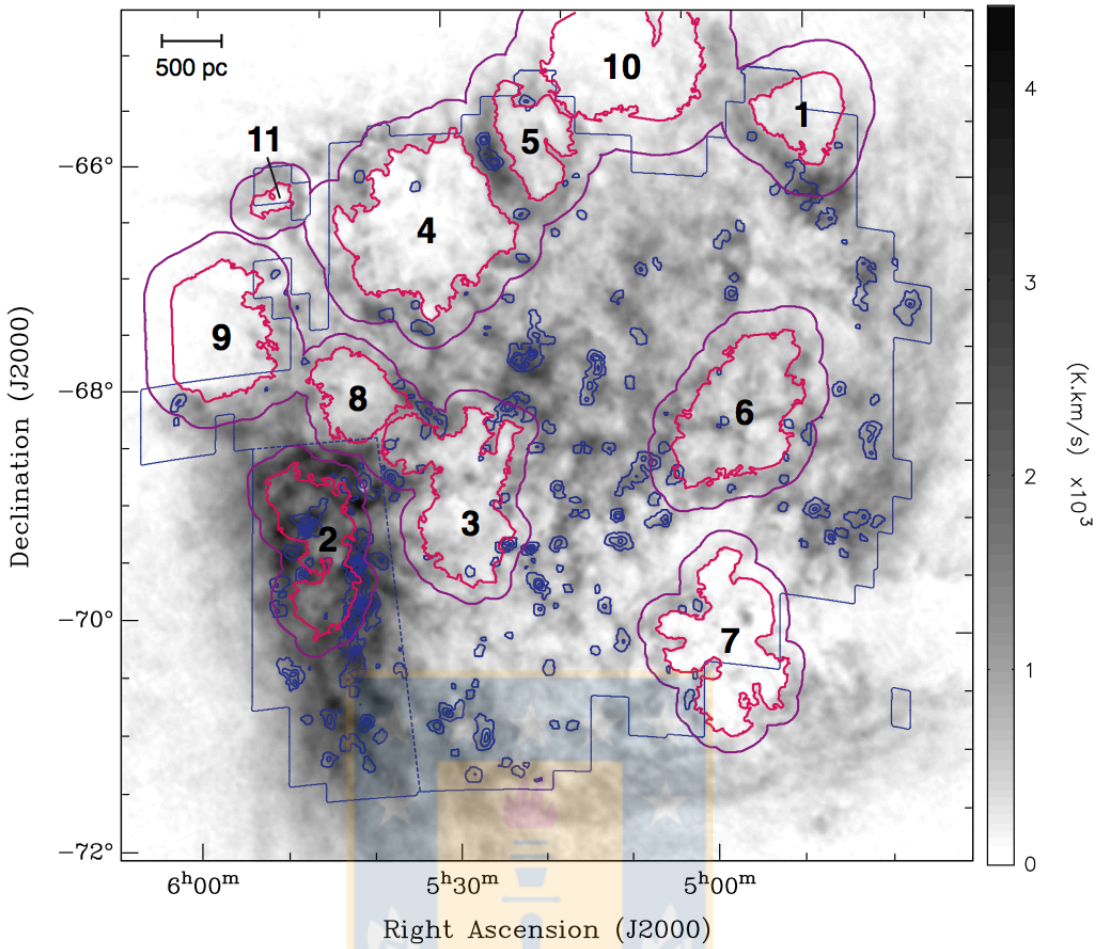

Figure 1.1: Supergiant shells and shell complexes in the LMC. Image reproduced from Dawson et al. (2013).

clouds and young stellar clusters in nine Hα SGSs identified by Meaburn (1980) in the LMC. They found that young stellar clusters are more actively formed by a factor 1.5 – 2 on the side of the molecular clouds near the rims of SGS, particularly where the Hα filaments are adjacent to the molecular Cloud. Furthermore, they found that 70 per cent of the clusters located within the boundary of the SGSs have likely been formed due to dynamical effects of the SGSs. These results suggest that the SGSs do play an important role in both the formation of molecular clouds and the dynamical triggering of recent star formation areas.

In this thesis, we have used the SGS and shell complexes defined by Dawson et al. (2013) to study their possible relationship with the areas of star formation, especially in the NGC 1850 region. These SGSs are organized into 11 spatially distinct complexes occupying $\sim$ 40% of the area of the main H I disk of the LMC, see Fig. 1.1. Our region of interest coincides with the complex labeled 6, for which we studied the effect of the SGS on star formation.

1.2 Eclipsing Binaries

Binary stars are of immense importance to astronomers as they allow the masses of stars to be determined. Actually most stars are in binary systems. Perhaps more than 50% of the stars are grouped into binaries or

multiple systems comprised of two or more stars gravitationally bound (Hilditch 2001). This factor however, is restricted to the present level of measurement accuracy and thus small or distant companions which have not been detected so far can significantly increase the number of binary/multiples system, (Poveda et al. 1982; Duquennoy & Mayor 1991; Tokovinin 1997). Nowadays even if the available data are far from complete, it has been suggested (al least as illustrative factors) that 30% of stars are single, 60% are binaries and 10% are multiple system (Eggleton 2006). Under this scenario, binaries are at least twice as common as single stars and thus they represent the largest population of astrophysical objects in the universe.

So, many stars show a periodic change in their apparent magnitude.[1] This can be due to two main reasons:

1. **Intrinsic changes**, in which variation is due to physical changes in the star or stellar system.

2. **Extrinsic changes**, in which variability is due to the eclipse of one star by another or the effect of stellar rotation

Thus, Variable stars are frequently divided into five main classes: the intrinsic pulsating, cataclysmic and eruptive variables, and the extrinsic eclipsing binary and rotating stars.
The variable stars that we deal in this thesis are eclipsing binaries. The first identification of eclipsing binaries is generally credited to John Goodricke in 1783 for his interpretation of Algol (β Persei), also known as the "*Demon star*", possibly due to the particular form of variations in brightness of the star caused by the mutual eclipses of the two components.
Goodricke (1783) demonstrated that the brightness of Algol decreased to a minimum at about two magnitudes below its normal level over an interval of 3.5 hours and then increased again over the same time interval, and that variability was periodic, with $P_0 \approx 2$ days (20.8 hours). He went on to propose that "if it were not perhaps too early to hazard even a conjecture on the cause of this variation, I should imagine it could hardly be accounted for otherwise than either by the interposition of a large body revolving around Algol, or some kind of motion of its own, by which part of its body, covered with spots or such like matter, periodically turned towards the earth". So we see that he was not entirely convinced that the light variations had to be due to Algol being an eclipsing system. In fact, modern studies have demonstrated that Goodricke was correct in one of his hypotheses and the starspots are indeed located on the cool secondary component of the Algol binary system.
Before addressing specific evolutionary scenarios in Algol-type binaries, we will present the generic features of binary evolution that lead to the formation of these binaries system.

1.3 Evolution in close binary stars

Close binary stars are a group of binaries where two stellar components are so close that they may influence each other's evolution. This is commonly effectuated by tidal forces by which the stars are deformed. A binary system is described by the orbital separation r, and the mass ratio of the components $q = M_s/M_p$ where M_p and M_s are the mass of the primary and secondary star, respectively, such that $M_p \geq M_s$. When the orbital separation between the two binary components is comparable to the radius of the largest stars, the dynamics of the system can no longer be described by a scheme of two point masses. In this case the internal structure of the star(s) has to be taken into account. So, the gravitational potential of the binary system is described by the Roche model where each star dominates the gravitational potential inside regions called *Roche lobes*. The two Roche lobes meet at the inner Lagrange point along the line joining the two stars.

Figure 1.2 shows equipotential surfaces in the orbital plane for a binary with $q = 0.4$. If the volume of either star exceeds the effective volume of its Roche lobe, then it is said to fill its Roche lobe (Hilditch 2001;

[1] https://www.aavso.org/types-variables

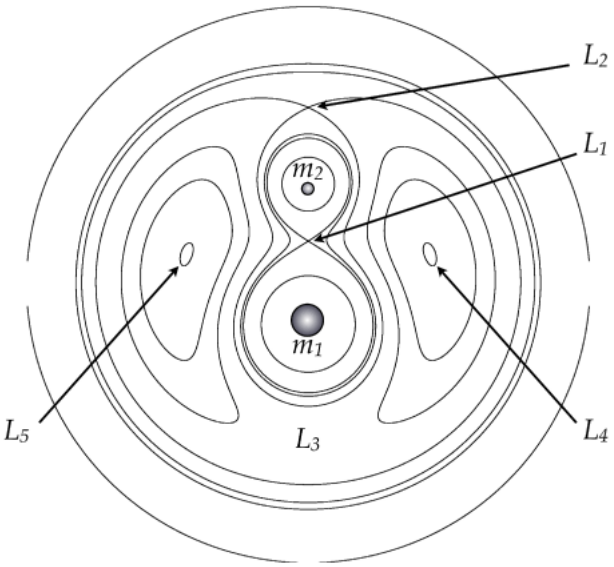

Figure 1.2: A schematic view of the cross section of equipotential surfaces in the orbital plane of a binary with $q = 0.4$. Image reproduced from Benacquista & Downing (2013).

Benacquista & Downing 2013). Matter will stream from a Roche lobe filling star through the inner Lagrange point to the other star in a process known as Roche lobe overflow (RLOF). Once the material crosses this point it is rapidly accelerated to supersonic speeds due to the gravitational attraction of the companion. As the mattter flows, it carries orbital angular momentum and depending on the size of the companion, the transferred material can directly impact onto the star or, if the star is compact enough, will form an accretion disc before being accreted by the companion. So, RLOF can be triggered by the evolution of the binary properties or by evolution of the component stars. Therefore, the orbital separation of the binary can change so that the Roche lobe can shrink to within the surface of one of the stars.

Also is possible that stellar evolution may eventually cause than one of the stars to expand and fill its Roche lobe. When both stars in the binary are main-sequence stars, the latter process is more common. Since the more massive star will evolve first, it will be the first to expand and fill its Roche lobe. At this stage, the mass exchange can be conservative (no mass is lost from the binary) or non-conservative (mass is lost). Based on the Roche lobe model, binaries can be classified according to three different situations:

Detached systems: The two binary components lie well inside their Roche lobes.

Semidetached systems: If one of the stars completely fills its Roche lobe (RLOF), while its companion lies inside its Roche lobe volume.

Contact systems: Both components fill, or even overfill, their critical Roche surfaces.

In addition to the RLOF mechanism a generally less efficient type of mass transfer is observed in close binaries where one star has a very strong and outward flowing stellar wind. Here, as the companion moves through the ejected matter, a fraction of the wind may be gravitationally accreted by the companion star, a phenomenon known as wind accretion. This process tends to be found in binaries where the mass losing component is a high mass star ($> 10\,M_\odot$) where strong winds driven by radiation pressure are observed. Slower winds can be found in detached binaries involving an AGB stellar component where the accretion process is

remarkably distorted by the Coriolis effect and must be investigated by numerical models (van Winckel 2003; Van Winckel 2007; Frankowski & Jorissen 2007).

1.4 Mass transfer

In this section we give a review of mass-tranfer process, as found in the literature of mass exchanging semidetached binaries, for more details see Hilditch (2001).
The natural evolution of a star involves an expansion of its outer layers, when a star lives in a close binary its maximum volume is restricted to its Roche lobe radius. Beyond this critical volume the star can transfer material via RLOF. A fraction of the transferred material can then be accreted by the companion while the rest will be shed into the surroundings. Although there are still many unanswered theoretical questions about the nature of the mass transfer phase, the basic properties of the evolution of a binary due to mass transfer can easily be described. The rate at which a star can adjust to changes in its mass is governed by three time scales. The *dynamical* time scale is the time required for a star to respond to departures from hydrostatic equilibrium, and can be approximated by the free fall time across the radius of the star,

$$t_{\rm dyn} \simeq \left(\frac{2R^3}{GM}\right)^{1/2} \sim 40, \left[\left(\frac{R}{R_\odot}\right)^3 \frac{M}{M_\odot}\right]^{1/2} \text{min}, \tag{1.1}$$

where M and R are the mass and radius of the star. For RLOF mass transfer process, the quick adiabatic response of a deep convective donor star causes the star to grow beyond its shrunken Roche lobe and causes runaway mass transfer on a dynamical time scale (so-called dynamical mass transfer).
The thermal equilibrium of the star is restored over a longer period given by the *thermal* time scale

$$t_{\rm th} \simeq \frac{GM^2}{RL} \sim 3 \times 10^7 \left(\frac{M}{M_\odot}\right)^2 \frac{R_\odot}{R} \frac{L_\odot}{L} \text{ yr}, \tag{1.2}$$

where L is the luminosity of the star. Mass transfer can occur on a thermal time scale when the donor star remains inside its Roche lobe after the quick adiabatic expansion. The mass transfer is then driven by the natural response of the star to reach the thermal equilibrium expanding beyond its Roche lobe. This type of RLOF occurs when the donor star has a predominantly radiative envelope.
Finally, the main-sequence lifetime of the star itself provides a third time scale, which is also known as the *nuclear* time scale:

$$t_{\rm nuc} \sim 7 \times 10^9 \frac{M}{M_\odot} \frac{L_\odot}{L} \text{ yr}. \tag{1.3}$$

Nuclear time scale mass exchange occurs when the donor star is less massive than the accreting (gainer) star. In this case, the mass transfer process can only be sustained by the evolutionary expansion driven by nuclear fusion reactions in the donor core. This is the slowest mode of mass transfer and is observed in the later phases of mass transfer when the mass ratio of the system has been reversed.
During the RLOF mass transfer process, the gainer star is severely perturbed by the rapid accretion of the transfered material. As the matter falls down from L_1 it carries a significant amount of kinetic energy which is mostly dissipated at or near the surface of the gainer star increasing its temperature considerably. Furthermore, the orbital angular momentum carried by the accretion stream can act to accelerating the accreting star. If the gainer is still on the main sequence, mass accretion will change its structure, causing it to behave like a more massive normal main-sequence star. If the accreting star has already left the main sequence, mass transfer can strongly affect its evolution and the star may never evolve to become a red supergiant but explode as a blue

supergiant (Podsiadlowski & Joss 1989). It is likely that the gainer star will swell up to or beyond its Roche lobe during a dynamical time scale mass transfer phase. In this case, the binary evolves into a contact system with a common envelope around the two Roche lobes.
Different modes of mass transfer can occur during the RLOF, depending on whether the mass transfer process is stable or not.

1.4.1 Conservative mass transfer

Conservative mass transfer occurs when there is no mass loss from the system, and therefore all mass lost from one star is accreted by the other star. During conservative mass transfer, the orbital elements of the binary can change. Consider a system with total mass $M = M_1 + M_2$ and semi-major axis a. The total orbital angular momentum

$$J = \left[\frac{GM_1^2 M_2^2 a}{M}\right]^{1/2} \tag{1.4}$$

is a constant, and we can write $a \propto (M_1 M_2)^{-2}$. Using Kepler's third law and denoting the initial values by a subscript i, we find:

$$\frac{P}{P_i} = \left[\frac{M_{1i}\, M_{2i}}{M_1 M_2}\right]^3. \tag{1.5}$$

Differentiating Eq. (1.5) and noting that conservative mass transfer requires $\dot{M}_1 = -\dot{M}_2$ gives:

$$\frac{\dot{P}}{P} = \frac{3\dot{M}_1(M_1 - M_2)}{M_1 M_2}. \tag{1.6}$$

Note that if the more massive star loses mass, then the orbital period decreases and the orbit shrinks. If the less massive star is the donor, then the orbit expands. Usually, the initial phase of RLOF takes place as the more massive star evolves. As a consequence, the orbit of the binary will shrink, driving the binary to a more compact orbit.
In an initially detached close binary the more massive star will evolve faster because of its own nuclear evolution and it will be the first to expand to its Roche lobe. The orbital separation thus decays in response to the mass transfer to a less massive component. The Roche lobe of the mass-losing star (hereafter donor) will shrink as well and, the resulting evolution of the binary will depend on the response of the donor to the loss of surface matter. If the donor star has a deep convective envelope the temperature gradient is steeper and as the material is lost from its surface a rapid adiabatic expansion takes place in order to restore the hydrostatic equilibrium. Hotter material is then brought to the surface and the star is now bigger than its thermal equilibrium configuration. This situation is intrinsically unstable because the larger the mass loss, the stronger the adiabatic expansion and the larger the donor extension beyond its Roche lobe. On the other hand, if the envelope of the donor star is mainly radiative the temperature gradient is less steep and the adiabatic expansion causes the star to be smaller than its thermal equilibrium size.

1.4.2 Non-conservative mass transfer

If part of the mass transferred from the donor star is not accreted by the gainer and leaves the system, the evolution of the binary will be non-conservative. Different mechanisms of mass loss have been observed in particular binaries such as systems with mass transfer/loss caused by a stellar wind, RLOF events occurring in a dynamical time scale, sudden catastrophic mass loss like a nova or supernova explosion of one of the binary components, among others. If the donor star is losing mass by wind-driven mass transfer and by RLOF at a

rate of $\dot{M}_1$, some fraction of that mass will be accreted by the gainer at a rate $\dot{M}_2$, and the rest $\dot{M}$, will be lost from the system. Thus, the total orbital angular momentum lost by the system because of the escaping matter, will be given by the fraction of orbital angular momentum lost by the donor and that contributed by any other mechanisms (K),

$$\frac{\dot{J}}{J} = \frac{M_2}{M_1}\frac{\dot{M}_1}{M_1 + M_2} + K. \tag{1.7}$$

An alternative form of the total orbital angular momentum lost by the binary can be found upon differentiation Eq. (1.4), which yields,

$$\frac{\dot{J}}{J} = \frac{\dot{M}_1}{M_1} + \frac{\dot{M}_2}{M_2} + \frac{\dot{a}}{2a} - \frac{\dot{M}}{2(M_1 + M_2)}. \tag{1.8}$$

Moreover, Kepler's third law can be differentiated to give,

$$\frac{\dot{P}}{P} = \frac{3\dot{a}}{2a} - \frac{\dot{M}}{2(M_1 + M_2)}. \tag{1.9}$$

The combination of equations (1.7), (1.8) and (1.9) gives a final equation to estimate a relation between the change in the orbital period and the rate of mass transfer and mass loss:

$$\frac{\dot{P}}{P} = -\frac{2\dot{M}}{(M_1 + M_2)} - \frac{3\dot{M}_2(M_1 - M_2)}{M_1 M_2} + 3K. \tag{1.10}$$

The K term allows the introduction of an additional angular-momentum loss mechanism, for instance via magnetic breaking (van't Veer & Maceroni 1992) or by gravitational-wave radiation (Landau & Lifshitz 1962).

1.4.3 Mass transfer cases

Depending upon the orbital separation, the onset of RLOF can occur any time during the evolution of the star. Mass transfer can be divided into three cases related to the timing of the onset of RLOF (see Hilditch 2001 for more details):

Case A: The initial orbital period of the binary is enough for the donor star to fills its Roche lobe while still on the main sequence. The thermal equilibrium of the donor is then strongly perturbed and a rapid phase of thermal time scale mass exchange takes place until the mass ratio is more than reversed and the evolution slows down to a nuclear time scale. The donor star is now an overluminous core hydrogen burning subgiant.

Case B: The donor star is burning hydrogen in a shell when it first fill its Roche lobe. Depending on the stratification of the donor's envelope, the initial phase of mass transfer can occur on a dynamical time scale or on a thermal time scale until the mass ratio is reversed. After that, a slower phase of mass transfer begins, which proceeds either on a thermal time scale or on a nuclear time scale depending on the initial mass of the mass losing star. Donors originally more massive than $3M_\odot$ will terminate the mass exchange when the star ignites helium in the core shrinking inside its Roche lobe. Donors with masses less than $3M_\odot$ will finish the rapid phase of mass transfer with the onset of electron degeneracy in the highly compressed helium core. The subsequent slow mass transfer rate generates binaries with a small mass ratio such as 1/5 or 1/10. The main sequence gainer star is now brighter than its less massive (overluminous) subgiant companion. This case is observed in *Algol-type binaries*. The mass transfer will end when the hydrogen envelope of the donor will be depleted. The donor then shrinks within its Roche

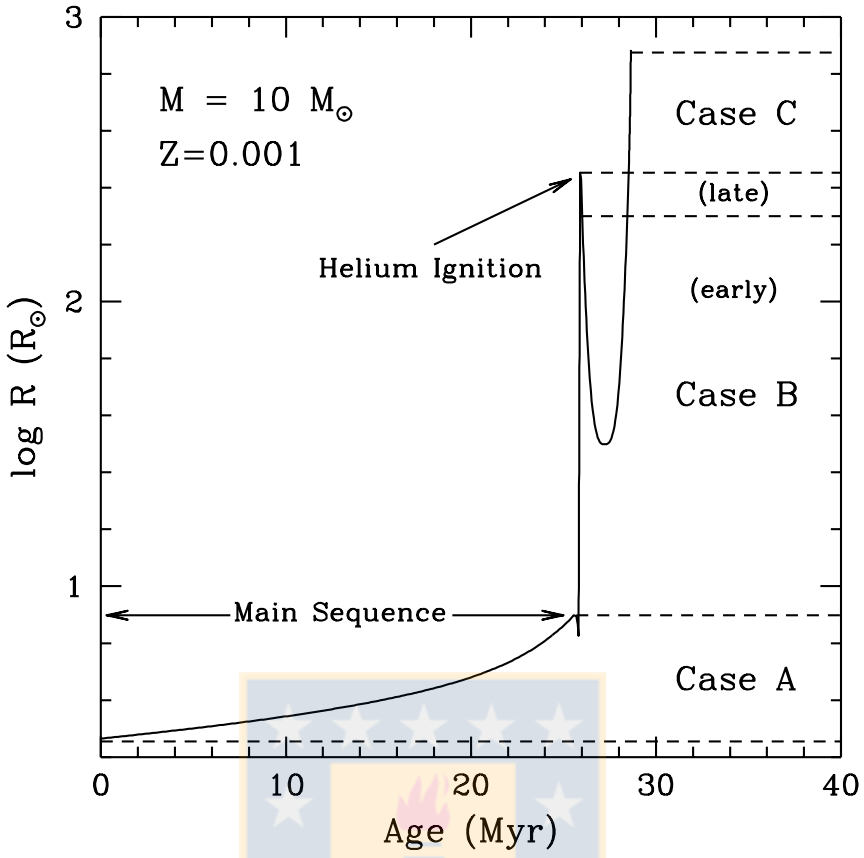

Figure 1.3: Evolution of the radius foo a a $10M_{\odot}$ star with a metallicity of $Z = 0.001$. Image taken from Pfahl et al. (2002).

lobe and becomes a low-mass helium white dwarf. Typical initial orbital periods for Case B binaries lie in the range of several to a hundred days.

Case C: When the initial orbital period of the binary exceeds a hundred days, the donor has enough volume to evolve through the supergiant stage, and completes core helium burning with a very extended envelope when it first fills its Roche lobe.

Figure (1.3) show the typical evolution of the radius expansion for a low metallicity star. Case-A mass transfer occurs during the slow growth, Case-B during the first rapid expansion, and Case-C during the final expansion phase. The nature of the remnant depends upon the state of the primary during the onset of RLOF and the orbital properties of the resultant binary depend upon the details of the mass transfer (Pfahl et al. 2002).

1.5 Double Period Variables

Double Period Variables (DPVs) are intermediate-mass semidetached Algol-type binaries, which show two closely related photometric periodicities. The shorter period reflects the binary period in the range of 1 and 16 days. The longer one is not exactly cyclic, lasting roughly 33 times the orbital period. DPVs were discovered in the Small Magellanic Cloud after a photometric search for Be stars in the OGLE-II database (Mennickent

et al. 2003, 2005). Heretofore, 114 systems have been identified in the Magellanic Clouds and 13 in our Galaxy (Poleski et al. 2010; Mennickent & Rosales 2014). Only four of these systems have been studied in detail in our galaxy (e.g., AU Mon, V393 Sco, DQ Vel, HD 170582) and one in the Magellanic Clouds (OGLE 05155332−6925581, see Chapter 3) which their stellar and orbital parameters have been derived and their line-profile variations at the maximum and at the minimum of the long-term cycle have been analysed (Desmet et al. 2010; Mennickent et al. 2012b; Garrido et al. 2013; Barría et al. 2013, 2014; Mennickent et al. 2015). Few DPVs have been studied in detail, so far. But however, from these representative cases, it was possible to derive insights and an overall picture about this class of objects.

Cumulative information from photometric and spectroscopic data, indicate that DPVs are intermediate-mass interacting binaries with a component filling their Roche lobe and transferring mass to the primary component. Complex and variable Balmer and Helium profile have been found in the five well analysed DPV system. Balmer profiles (sometimes also He I) usually consist of a central absorption surrounded by emission shoulders of variable intensity. These broad and variable He I lines probably probe an accretion disc, which has been modelled with sophisticated photometry algorithm, which have provided the most realistic set of parameters in the literature, because they incorporate in the model not only the stellar components but also the Hα emitting circumprimary accretion disc (Djurašević et al. 2010) .

Additionally, the determination of the stellar parameters for these systems has allowed the comparison with those predicted by evolutionary tracks for binary stars, which include epochs of non-conservative evolution given by van Rensbergen et al. (2008a). The evolutionary history for four of the cases previously mentioned has been checked using these models with remarkable results: AU Mon was found inside an episode of mass transfer with age 196 million years, indicating that the system has a donor exhausted of hydrogen in its core, transferring mass at the relatively high rate of 7.5×10^{-6} $M_\odot$ yr^{-1} (Mennickent 2014), V393 Sco has been found immediately after a burst of a high mass loss, arguing that the recently high amount of mass transferred has not been fully accumulated by the still critically rotating gainer star, and thus is consistent with the existence of a circumprimary accretion disc (Mennickent et al. 2012a, hereafter M12a), the older system DQ Vel has been found in a state of low mass transfer, where the gainer had time to slow down, allowing the formation of an extended accretion disc (Barría et al. 2014). Finally, OGLE 05155332−6925581 which is the case we will discuss in detail in Chapter 3, was found also inside a burst of mass transfer where the donor star is transferring an amount of 3.1×10^{-6} $M_\odot$ yr^{-1} (Garrido et al. 2013). One notable observation obtained from the comparison with the models is that the considering the relatively high mass transfer rate should produce changes in the observed orbital period. Mennickent calculated for AU Mon that the period should change 15 seconds per year due to mass transfer and the same happens with the period of OGLE 05155332−6925581, which should change 4.7 seconds per year (see, Section 3.4.2), which is definitely not observed in any of the two systems. There is photometric and spectroscopic evidence, that give support for the mass and angular momentum losses for these systems (Mennickent et al. 2008; Desmet et al. 2010; Peters 1994), but then why are no changes are observed in the period?. This inconsistency between the relatively large mass transfer rate and the constancy of the orbital period in the non-conservative regime, leads us to ask: Is the mass loss modulated by some still unknown process, which produces a constant orbital period in the DPV systems?. Answering this question will be one of main goals to answer with this thesis work in the Chapter 3 and of course, our contribution to the knowledge of the DPV systems in low metallicity enviroments.

Hereinafter, we use interchangeably the words primary (*gainer*) and secondary (*donor*) for the components of the binary system as usual in the literature of mass exchanging semi-detached binaries.

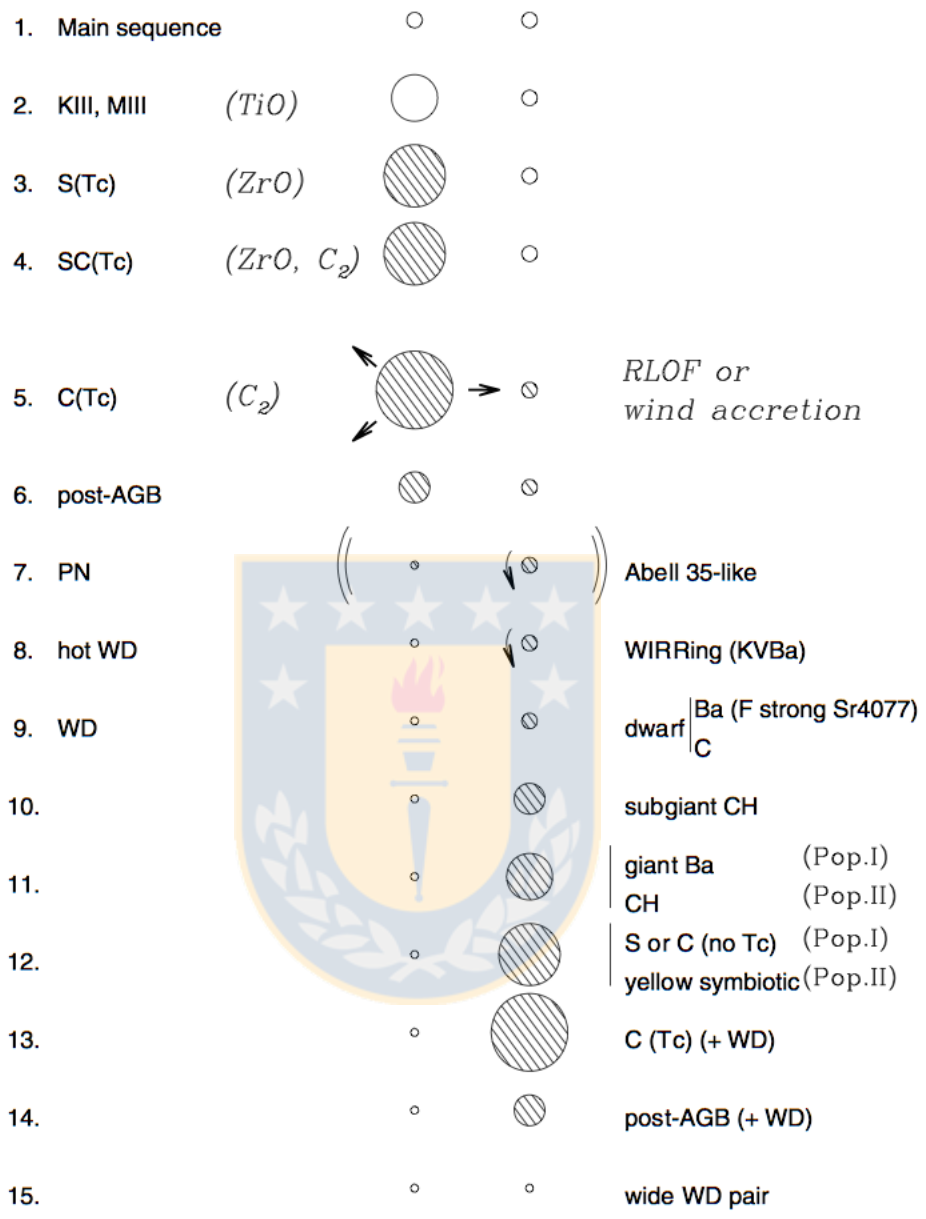

Figure 1.4: The different presumed stages in the evolution of a binary system consisting of two intermediate-mass stars in a (not too) close orbit. The left column corresponds to the normal evolutionary sequence of single stars, while the right column represents the various classes of stars with chemical peculiarities specifically produced by mass transfer across the binary system. Hatched circles denote stars with atmospheres enriched in carbon or heavy elements (see Jorissen (2003); Frankowski & Jorissen (2007), for a detailed description of the various kinds of symbiotic stars and peculiar red giants involved). Image taken from Jorissen et al. (2009).

1.6 Binary post-AGB stars

Post-AGB stars are low or intermediate initial mass ($\leq 8M_{\odot}$) stars that end their lives losing a large fraction of their mass. Within 10^5 years between 20% and 80% of the total-mass is ejected in the so-called super-wind event. This happens in the Asymptotic Giant Branch (AGB) when the stars consists of a degenerate carbon-oxygen core surrounded by a nuclear burning shell that in turn is surrounded by a convective envelope. When the super-wind has depleted the envelope to $\sim 0.01M_{\odot}$ the photosphere collapses, the super-wind stops and the star rapidly moves to the blue region of the HR diagram. The star starts to ionize the surrounding ejecta forming a planetary nebula. This last process lasts about 10^4 years, hence observing post-AGB stars is rare due to their short-lived nature and not many of them are known (e.g. Szczerba & Górny 2001; van Winckel 2003).

Fig. 1.4 shows one of the suspected evolutionary sequences of a system having two low- or intermediate-mass Main Sequence (MS) stars (initially wide enough to avoid significant interaction during pre-RGB phases). The object studied in the third part of this thesis, ELHC 10, is located in stage 6: a system consisting of a luminous post-AGB star and a MS companion surrounded by a circumbinary disc. The kind of interaction that leads to circumbinary disc formation is not known and two possible solutions have been proposed: The first poses that during the evolution of these stars, there must have been a phase of strong interaction when the primary was a giant. It is during this phase of strong interaction that non-conservative mass transfer may have occurred, creating a circumbinary disc (Waters et al. 1992; Jorissen 2003; Frankowski & Jorissen 2007). Another possible formation scenario includes a wind-capture scenario, where the AGB wind is captured by the companion (Mastrodemos & Morris 1998, 1999). But so far, neither of the two theoretical predictions comply with the observational constraints, which indicates that wind-RLOF and CE ejection processes are still far from being understood.

On the other hand, it is generally accepted that many of the peculiar morphologies of the planetary nebula (PNe) are due to these binary interactions. The current hypothesis for PNe formation requires the presence of a binary system in the center to explain how many of them can be asymmetric. The main problem with this "binary hypothesis" is the detection of these binary systems, since few have been detected in the center of PNe and it is here where the post-AGB binaries represent an interesting population to fill up the void, since after the post-AGB phase, the next phase is the planetary nebula stage (See, stage 7 in Fig. 1.4).
The number of known binaries among the post-AGB stars is low, the most famous case in the Milky Way is HD 44179, better known as the Red Rectangle Nebula. The detection of binarity for post-AGB stars on the basis of radial velocity measurements is far from trivial and additional to this, the presence of shocks in the atmosphere cause line-deformation and line-splitting which makes the determination of the radial velocity difficult (Klochkova 2015).

Besides, the binary post-AGB stars can be divided into two groups: stars with abundance patterns similar to single stars (e.g. 89 Her, Luck et al. 1990), and a group of very metal deficient objects (Lambert et al. 1988; Van Winckel et al. 1995), with [Fe/H] between -3 and -5. It was pointed out by Venn & Lambert (1990) that the abundance patterns in these extreme cases resemble those of the depletion of gas-phase elements in the ISM, i.e. strong underabundance of elements such as Mg, Fe, Ti and Cr, while C, N, O and S are solar. The detection of Zn with roughly solar abundance in HD 52961 (Van Winckel et al. 1992) and the Red Rectangle (Waelkens et al. 1996) confirmed this depletion scenario. The basic scenario of this process is that circumstellar gas is separated from the dust and subsequently re-accreted onto the star (Mathis & Lamers 1992; Waters et al. 1992). Recently, post-AGB objects with similar depletion patterns and far-IR excesses (van Aarle et al. 2011),

have been detected in the Large Magellanic Cloud (LMC), showing that the formation of a circumbinary disc is probably a common phenomenon in post-AGB binaries (De Ruyter 2005; de Ruyter et al. 2006)

1.7 The aim of this work and its structure

The subject of this thesis is devoted to the observational study of Hα emission-line stars (ELSs) in low metallicity environments. More specifically, this thesis studies the star-formation conditions and stellar evolution of ELS in the LMC, and investigates the processes of mass exchange and mass loss in binary systems. To do this, we used high-resolution optical spectroscopy, slitless spectroscopy, multicolor light curve and multi wavelength photometry at difference instruments and telescopes to obtain their stellar parameters and investigate the stellar properties, paying particular attention to the effects of shocks and ionization fronts on the interstellar medium propagating star formation in the LMC.
On the other hand, we have studied processes of mass and angular momentum loss in two eclipsing binaries in the LMC. High-resolution optical spectra at different instruments and telescopes were analyzed to derive stellar and orbital parameters for these systems and multicolor light curves obtained from public databases are used to derive the orbital solution for these system.

This work is organized as follows:

In Chapter 2, we investigate the star-formation conditions, and stellar evolution of Hα emission-line stars in the LMC star-forming region NGC 1850 and its surrounding field. Since various populations of stars with very different ages have been identified in this field, it appears that its history is rather complex. In this Chapter, we discuss the observational evidence of how the advancing ionization fronts and expanding superbubbles, giant shells or supergiant shells compress nearby clouds, increasing their density and causing the collapse of deeply embedded cores, leading to bursts of second-generation star formation in their peripheries and action zones. To investigate and to determine the influence of supergiant shells on new star formation, and to also estimate the evolutionary stage of these stellar populations, we used slitless spectroscopy with the Wide Field Imager (WFI) instrument on the Max Placnck 2.2 m at la Silla, in order to identify the Hα emission-line objects in the SGS complex number 6, which have been shown to have a simple expanding-shell structure. Hα emission-line objects, H II regions and OB associations are used to infer star formation in the last few years, while distributions of ionized, H I and molecular components of the interstellar gas are compared with the sites of recent and current star formation to determine whether triggering has taken place around SGS complex number 6.

In Chapter 3, we analyze multicolor light curves and high resolution optical spectroscopy of the eclipsing binary and Double Periodic Variable OGLE 05155332−6925581. According to Mennickent et al. (2008), this system shows a significant change in the long non-orbital photometric cycle, a loop in the color-magnitude diagram during this cycle and discrete spectral absorption components that were interpreted as evidence of systemic mass loss. We study the evolutionary route for the Large Magellanic Cloud interacting binary OGLE 05155332−6925581 by comparison of its stellar and orbital parameters with theoretical evolutionary tracks. The best representations for the current observed properties in this interacting binary are found under a non-conservative evolutionary regime, which includes mass loss from the system at some stage of the binary history. We compare the evolutionary stages of OGLE 05155332−6925581 with other DPV systems such as V393 Sco (Mennickent et al. 2012b), DQ Vel (Barría et al. 2013) and AU Mon (Mennickent 2014) to investigate the differences observed in their accretion disc. Our studies indicate that the DPV phenomenon is observed at different

evolutionary stages; but always inside of after a main mass transfer burst.

In Chapter 4, we investigate the luminous star ELHC 10 located in the bar of the Large Magellanic Cloud. We focus on solving the uncertainty about the nature of this complex eclipsing binary by performing a thorough analysis of the stellar components and the surrounding environment. High-resolution spectra and very accurate *BRI* light curves allowed us to study ELHC 10 in unprecedented detail for the first time. We have determined solid constrains for some parameters of the system which lead us to think that ELHC 10 could be the first post-AGB binary in the Large Magellanic Cloud, and the post-AGB binary with the highest progenitor mass and the highest-mass companion known. On the other hand, our study provides observational evidence that a circumbinary disc in post-AGB stars can be formed by binary star interaction and outflows through the outer Lagrangian points. This is a very important insight, since previously the process of disc formation in post-AGB stars has been obscure.

In the final chapter, we conclude this thesis with some general conclusions and some possibilities for future research are given.

Chapter 2

The LMC NGC 1850 region history: Emission-line stars as tracers of star formation episodes

2.1 Introduction

NGC 1850 is a young double cluster (labeled NGC 1850 A and B) located at the north-west edge of the bar in the LMC (see Fig. 2.1). It is located in a region of the LMC bar rich with star clusters and vigorous star-formation activity in the recent past, with a prominent extended peak between 100 Myrs and 50 Myrs ago associated with the dynamic interaction between the cluster and the embedded emission nebula LHA 120-N 103B, and a more recent peak 12 Myrs ago (see, e.g., Fischer et al. 1993; Gilmozzi et al. 1994). Furthermore, the main cluster NGC 1850 A appears as a globular-like cluster and has an age of 50 ± 10 Myrs, while the compact blue star cluster companion NGC 1850 B is located 30″ west of the center of NGC 1850 A and is more loosely distributed. It is much younger, with an age of 4.3 ± 0.9 Myrs confirmed by the detection of a pre-main sequence population of stars associated with it (Gilmozzi et al. 1994). The environment of NGC 1850 shows several salient features (see Fig. 2.2). For instance, there is an arc-like nebular feature visible in Hα in the east side of the cluster. This feature is characterized by a high concentration of ELS and YSOs. Furthermore, one supernova remnant SNR B0509-68.7, frequently confused with LHA 120-N 103B, is located in the northern part of this H II region. This SNR has been shown to be the product of a Type Ia supernova based on the abundance of Si, S, Ar, Ca, and Fe derived from X-ray observations, and has an age of $\sim$ 860 yr and angular size of $\sim 0.46'$ (Lewis et al. 2003; Rest et al. 2005; Badenes et al. 2007). Because the progenitor of this supernova was not a massive star, and because it occurred very recently, it did not have the possibility of triggering the star formation in the ambient molecular cloud. In Fig 2.2 it is possible see, at 10′ to the south-east of NGC 1850 the cluster NGC 1858, which is also embedded in the H II region LHA 120-N 105A.

2.2 Age and spatial distribution of stellar populations surrounding NGC 1850

Fischer et al. (1993) presented a detailed study of the stellar content in NGC 1850 using *BV* photometry and echelle spectra of 52 supergiants, estimating several cluster parameters such as reddening, age, and internal dynamics. They found 3 distinct populations of stars. The first was the bulk of main-sequence stars that constitute the main cluster NGC 1850 A. The second was the PMS population belonging primarily to the very

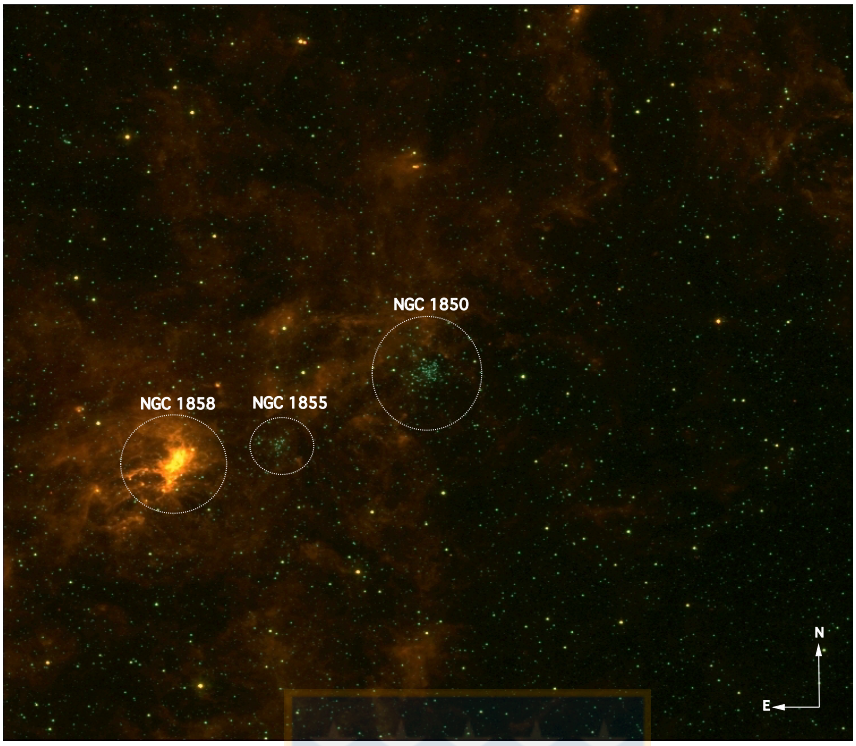

Figure 2.1: Combine Spitzer IRAC images (3.6, 5.8 and 8.0 μm) on the center of cluster NGC 1850.

young cluster NGC 1850 B, whose center is located $\sim 30''$ W of the main cluster. The third population are red giant stars, mainly comprised of LMC field stars. These three populations were confirmed and their ages were better constrained by Gilmozzi et al. (1994) using optical and ultraviolet imaging observations obtained with the Hubble space telescope (see Section 2.1). More recently, the cluster population has been studied using two-color diagram (2-CD) photometric techniques to identify candidate Be stars (Wisniewski & Bjorkman 2006). Therefore, the LMC NGC 1850 cluster is a region of interest for studies of the star formation process. Since various populations of stars with very different ages have been identified in this field, it appears that its history is rather complex. Book et al. (2009) and Yamaguchi et al. (2001b) examined the recent star formation associated with supergiant shells in the LMC. They found observational evidence of how the advancing ionization fronts and expanding superbubbles, giant shells or supergiant shells compress nearby clouds, increasing their density and causing the collapse of deeply embedded cores, leading to bursts of second-generation star formation in their peripheries and action zones . To investigate and to determine the influence of supergiant shell complex number 6 on new star formation in the LMC star-forming region NGC 1850 and its surrounding field, and to estimate the evolutionary stage of these stellar populations, we used slitless spectroscopy in order to identify Hα emission-line objects, as discussed in the following sections.

2.3 Slitless Hα spectroscopy with the WFI Instrument

2.3.1 Observations

Dr. Dietrich Baade et. al. performed observations on September 26, 2002 at the 2.2 m MPG/ESO telescope at La Silla Observatory with WFI in slitless spectroscopic mode. The R50 grism combined with the Hα filter

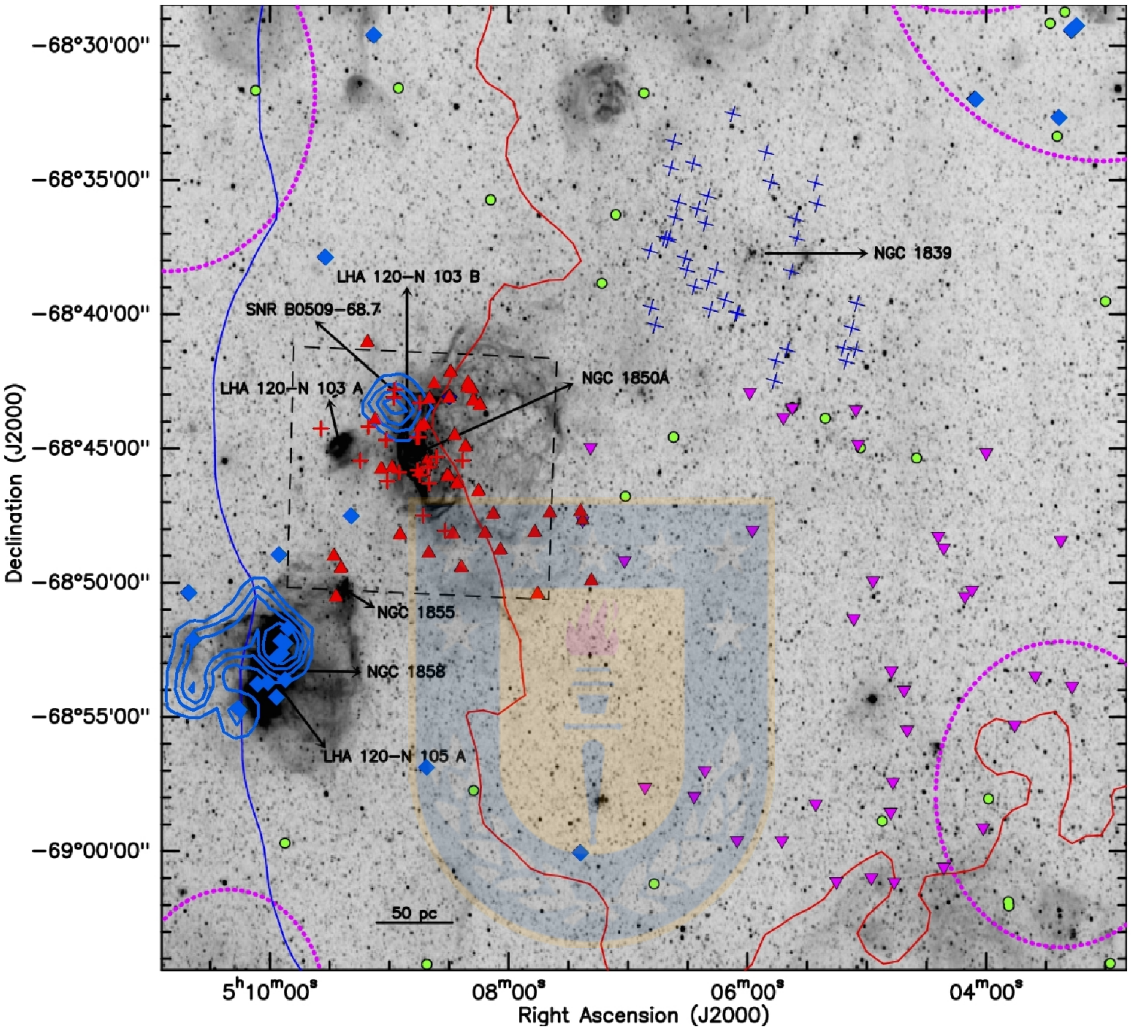

Figure 2.2: Hα image from MCELS on the center of cluster NGC 1850 and spatial distribution of the stars classified in this work using slitless spectroscopy. The different distribution of early-type and late-type stars can be seen: ELS (red triangles) and CELS (red crosses). Confirmed YSOs from Gruendl & Chu (2009) are shown in blue diamonds, while B stars with hydrogen in emission from Iqbal & Keller (2013) are marked with blue crosses, ELS from Reid & Parker (2012) are marked with green points and ELS with high resolution spectra in the ESO archive appear in magenta inverted triangles. The dashed black box shows part of the WFI-slitless field for which all WFI spectra were extracted. The blue and red solid lines represent the inner and outer edges of the SGS 6 complex, discussed in Section 2.5.2. North is up, east to the left.

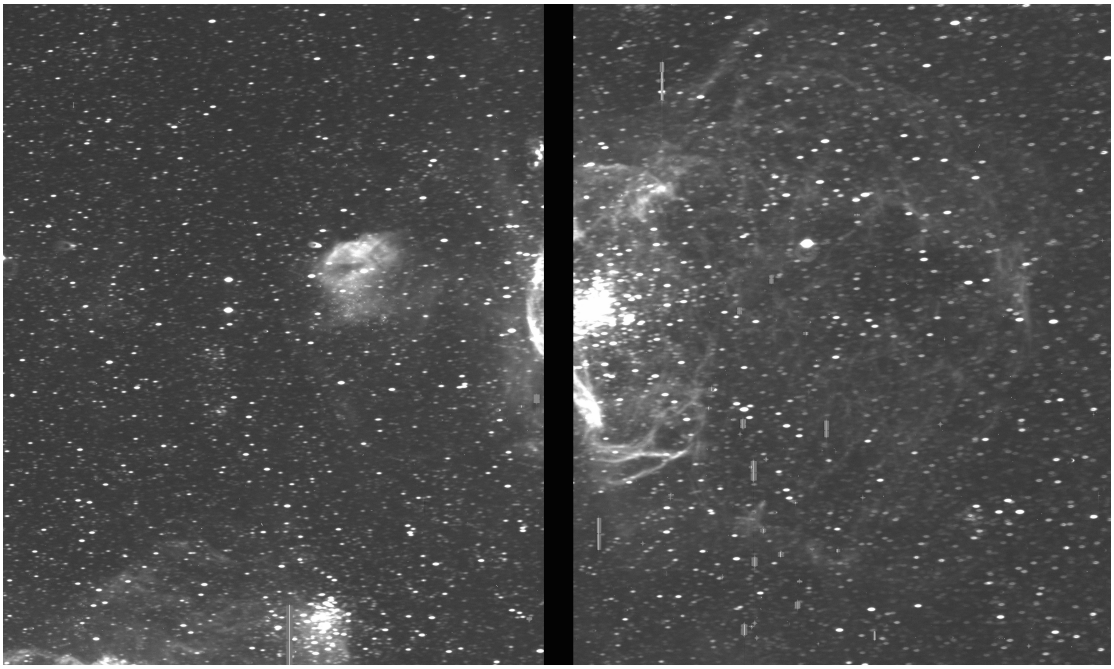

Figure 2.3: $11' \times 8'$ ESO-WFI frame in slitless spectroscopic mode with the filter RC (200 nm bandpass) centered on Hα. The stars appear as spectra. The diffuse background is due to the Hα emission line of the nebulosity. North is up, east to the left.

where used. They allow to reduce the crowding and the overlapping between spectra in dense stellar regions such as the bar of the LMC. Each image has a $34' \times 33'$ field and the typical exposure time was 400s, with a seeing of about $\sim 1.1''$. About 20 pointings were performed in the LMC as shown in Martayan et al. (2010b), resulting in 5 million spectra. The use of WFI allows the coverage of a large spatial area at once while the slitless mode allows one to obtain spectra not contaminated by diffuse ambient nebula, and therefore it does not lead to false detections of circumstellar (CS) emission-line stars. However, the low spectral resolution is not able to detect the weak emission. Martayan et al. (2010a), about 80% to 90% of the Hα ELS are detected with WFI down to $V \sim 16.5$ mag. Only the stars with emission peaks weaker than twice the continuum, or with EW_α above -10 Å are not detected. For fainter magnitudes the completeness rate of detection falls to about 50%. Spectra with signal-to-noise ratios smaller than 10 cannot be properly processed. As explained by Martayan et al. (2010a), there is a differential defocus in all the WFI images, which increases from the center to the edges of the image. This defocus that in principle would be a disadvantage as it causes a changing spectrum shape inside each image, was turned into an advantage for the recognition of emission-line stars, because the emission of the Hα line has taken the shape of a doughnut or horseshoe (i.e, in the telescope pupil), which leads to ELS stars being easily recognized on the image in areas with more defocus, as described in Section 2.3.2. The image of the field of NGC 1850 in slitless spectroscopic mode, that we used for this part of PhD thesis is shown in Fig. 2.3

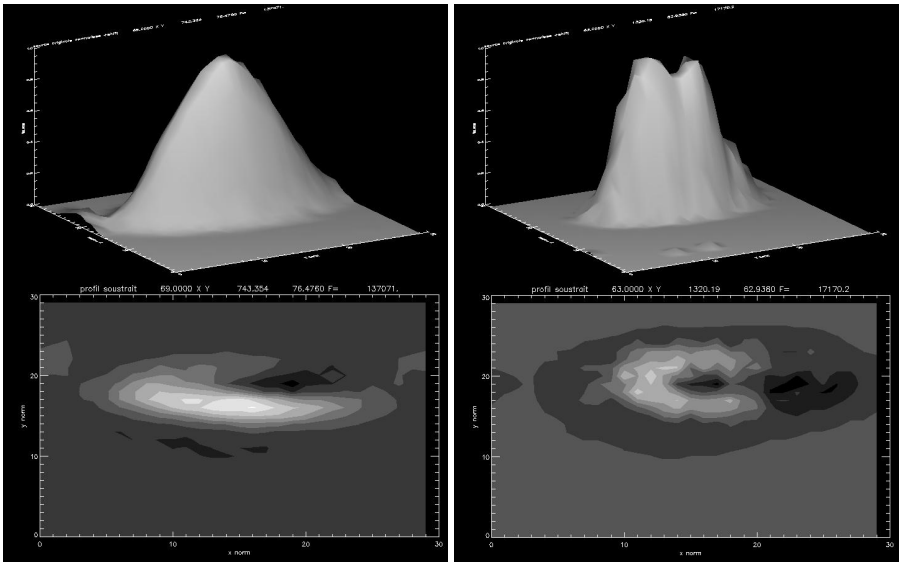

Figure 2.4: The appearance of the objects with and without Hα emission in defocused slitless WFI spectra extracted of region NGC 1850. *Top:* 3-D representations of the original flux distributions, *bottom:* 2-D projections of the residual after subtraction of the mean, scaled point spread function (PSF) of a pure continuum source. While a pure continuum source is just blurred by the defocus, a (nearly unresolved) emission line is effectively imaged like a point source, yielding a roughly donut (or horseshoe) like image of the pupil. The bright excess above the mean of the image corresponding to the emission peak is visible in the center-upper of the horseshoe (bottom right figure). Imagen taken from Garrido, Martayan & Aguayo (2015) in preparation.

2.3.2 Data reduction and emission-line stars identification

Dr. Christophe Martayan et al. in 2010 made a basic imaging data reduction with IRAF[1] and its MSCRED package. The extraction of the spectra was performed using a modified version of *SExtractor* (Bertin & Arnouts 1996). As previously mentioned, only spectra with signal-to-noise ratios above 10 were properly processed, which allowed us to extract objects with V magnitudes down to 20. However, in the area of very high background or very strong defocus the spectra cannot be extracted. This affects less than 10% of the entire spatial coverage of WFI.

In order to recognize ELS in NGC 1850 region the *IDL* script ALBUM (Martayan et al. 2008, 2010a) was used in this thesis. It allows the user to choose a local extraction area near the cluster to obtain the average spectrum with flux above a certain user-defined threshold. This method allows to calculate different average spectra for each cluster and therefore to properly take into account the amount of defocusing of the local area. Album starts out from the assumption that the 2-D PSF varies only slowly with position in the frame. To compute the 2-D PSF, typically 50 – 250 spectra were registered (by cross-correlation), coadded, and normalized. This step is operator-supervised; and unsuitable stars can be rejected. In the first step, all obvious emission-line stars, apparent binaries, too closely spaced sources, spectra with severe cosmic ray hits or otherwise reduced quality are rejected and a new regional mean spectrum is computed. It was empiricially established that the inclusion, at the $\leq$ 5% level, of emission-line objects only insignificantly modifies the regional mean spectrum profile. The resulting regional template spectrum was subtracted (after cross-correlation and shift in X and Y) from each normalized 2-D spectrum to be checked for Hα line emission . Album also automatically rejects artifacts

[1]IRAF is distributed by the National Optical Astronomy Observatories, which are operated by the Association of Universities for Research in Astronomy (AURA), Inc., under cooperative agreement with the National Science Foundation.

such as ghosts or cosmic ray events by applying a suite of tests to the shapes of the spectra. In the case of emission-line stars, the 2-D spectra exhibit a secondary peak (see Fig. 2.4).

So, the spectra were inspected following the method previously described, and according to their shape, the spectra were classified into three categories: emission-line stars, candidate emission-line stars (CELS), and normal stars without emission peak in Hα. The ELS are those with data good enough to distinguish the emission pattern clearly without any doubts. CELS show noisy spectra or spectra affected by defocusing, making the apparent presence of emission uncertain.

2.3.3 Astrometry and cross-matching of WFI sources with optical and infrared surveys

Once all the stars in the sample were classified, we performed astrometry using the ASTROM package (Wallace & Gray 2003). We used 28 reference stars with good astrometry and low proper motions from the UCAC2 (Zacharias et al. 2004) catalogue in the region of NGC 1850. The coordinates for the 1979 sources in this field were obtained with an RMS better than 1″ (accuracy from 0.5″ to 0.7″). Once the astrometry was done, the WFI stars were cross-correlated with the OGLE-II database with a tolerance radius for detection limited to 1.2″. We succesfully matched 1159 stars, i.e., a matching rate of 58.2%, most probably due to the strong nebulosity of the area leading to missing sources in the OGLE catalogues. Among these 1159 stars we found 38 ELS, 26 CELS in the star-forming region NGC 1850. In total our sample of interest is comprised of 64 stars (See, Table 2.1).

Subsequently, we performed a conservative neighbor search with a 1.2″ searching radius and selected the closest match for each source using TOPCAT[2] (Tool for OPerations on Catalogues And Tables, Taylor 2011). In this way, the MACHO (Alcock et al. 1999) and OGLE available light curves were retrieved for 58 stars (for more details about this, see discussion in Section 2.4.2), as well as the photometry in the wavelength range $0.3 - 22\,\mu$m from optical, near-and mid-infrared catalogs, described in the next section.

MCPS and OGLE II optical photometry

In Table 2.3 we present the $UBVI$ magnitudes from the Magellanic Clouds Photometric Survey (MCPS). MCPS includes 24 million stars in the central 64 deg^2 area of the LMC (Zaritsky et al. 2004). MCPS has incorporated the catalogs of Massey (2002) for bright stars and DENIS, which was used to confirm the observational uncertainty estimates. MCPS has a typical seeing about $\sim$ 1.5″ and magnitudes are in the Johnson-Kron-Cousins photometric system (Landolt 1983, 1992). The mean BVI magnitudes from the OGLE II catalog are also given in Table 2.3. OGLE II has a median seeing for the entire dataset of about 1.3″, and the uncertainty of the zero-point is less than 0.02 mag (Udalski et al. 2000).

Near and mid-infrared photometry

We obtained near-infrared (NIR) and mid-infrared (MIR) photometry for the observed ELS. The NIR photometry includes magnitudes from the IRSF Magellanic Clouds point sources catalog (Kato et al. 2007), which contain 15 million point sources in the central 40 deg^2 of the LMC. IRSF has an average seeing of 1.3″, 1.2″, 1.1″ and limiting magnitudes of 18.8, 17.8, and 16.6 mag in the J, H and K_S bands, respectively. The MIR search includes: 1) the four bands of the SAGE survey that uniformly imaged in 3.6, 4.5, 5.8, and 8 μm the central 7 deg^2 of the LMC with the IRAC instrument on the Spitzer Space Telescope (Meixner et al. 2006) and

[2] http://www.star.bris.ac.uk/~mbt/topcat/

MACHO	OGLE ID	$(B-V)_0$	$(V-I)_0$	V_0	M_V	SP from	$(H-K)_0$	$(J-H)_0$	SED fitting values			Excess	Classification	Classification	Reference
or WFI ID		(mag)	(mag)	(mag)	(mag)	colors	(mag)	(mag)	T_{eff}	$\log g$	SP	SED	stars WFI	diagnostic	
1.4539.193	SC11 157005	-0.32	-0.21	16.195	-2.30	B2	0.10	0.02	17000 ± 1000	5.0 ± 0.5	B4 V	yes	ELS	PBe	2
1.4539.151	SC11 162383	-0.19	0.01	16.259	-2.23	B2	0.30	0.10	17000 ± 1000	5.0 ± 0.5	B4 V	yes	ELS	PBe	2
1.4539.228	SC13 162385	-0.17	-0.12	16.461	-2.03	B2	0.28	0.18	17000 ± 1000	5.0 ± 0.5	B4 V	yes	ELS	PBe	…
2.4661.3757	SC11 257440	-0.07	0.14	16.896	-1.60	B3	0.37	0.16	17000 ± 1000	5.0 ± 0.5	B4 V	yes	ELS	PBe	…
1.4539.185	SC11 162423	-0.15	-0.31	16.438	-2.06	B2	0.23	-0.07	19000 ± 1000	5.0 ± 0.5	B2-B3 V	yes	ELS	PBe	…
1.4539.134	SC11 162456	-0.17	-0.18	16.066	-2.43	B2	-0.05	0.13	17000 ± 1000	5.0 ± 0.5	B4 V	yes	ELS	PBe	…
1.4540.778	SC11 168904	-0.17	-0.04	17.127	-1.37	B4	0.14	0.13	17000 ± 1000	5.0 ± 0.5	B4 V	yes	ELS	PBe	…
1.4540.168	SC11 168906	-0.28	-0.27	16.842	-1.65	B3	0.22	-0.13	25000 ± 1000	3.5 ± 0.5	B1 IV	yes	ELS	PBe	…
1.4660.2117	SC11 251211	-0.20	-0.13	16.719	-1.77	B3	0.27	-0.02	17000 ± 1000	5.0 ± 0.5	B4 V	yes	ELS	PBe	1
79.4659.3417	SC11 338244	0.27	0.48	15.128	-3.37	F4	0.21	0.32	7000 ± 100	2.0 ± 0.5	F2 II	yes	ELS	Ceph	2
1.4661.1151	SC11 257414	-0.17	-0.09	16.155	-2.34	B2	0.12	0.03	17000 ± 1000	5.0 ± 0.5	B4 V	yes	ELS	PBe	1
79.4659.3525	SC11 338482	-0.24	-0.21	16.084	-2.41	B2	0.18	-0.02	22000 ± 1000	5.0 ± 0.5	B2 V	yes	ELS	PBe	…
WFI-1587	…	-0.11	-0.28	15.862	-2.63	B1	0.17	0.11	18000 ± 1000	4.5 ± 0.5	B3 V	yes	ELS	PBe	2
1.4540.35	…	-0.13	-0.35	16.248	-2.25	B2	0.18	0.05	18000 ± 1000	5.0 ± 0.5	B3 V	yes	ELS	PBe	1
1.4550.105	…	-0.16	-0.34	15.907	-2.59	B1	0.03	-0.04	19000 ± 1000	4.5 ± 0.5	B2-B3 V	yes	ELS	PBe	1
1.4539.354	…	-0.12	-0.26	16.801	-1.69	B3	0.02	0.18	19000 ± 1000	5.0 ± 0.5	B2-B3 V	yes	ELS	PBe	1
1.4539.302	…	-0.18	-0.25	16.682	-1.81	B2-B3	0.22	0.20	18000 ± 1000	4.0 ± 0.5	B3 V	yes	ELS	PBe	1
1.4539.350	…	-0.19	-0.36	16.807	-1.69	B3	0.35	0.00	18000 ± 1000	5.0 ± 0.5	B3 V	yes	ELS	PBe	1
WFI-1489	…	-0.19	-0.30	16.252	-2.24	B2	0.17	0.06	22000 ± 1000	5.0 ± 0.5	B2 V	yes	ELS	PBe	…
WFI-1756	SC11 168610	-0.23	-0.12	16.024	-2.47	B2	0.17	-0.01	18000 ± 1000	5.0 ± 0.5	B3 V	yes	ELS	PBe	…
1.4418.60	SC11 76699	-0.20	-0.12	15.456	-3.04	B1	0.18	0.00	19000 ± 1000	3.5 ± 0.5	B2 - B3 IV	yes	ELS	PBe	…
1.4539.191	…	-0.12	-0.32	15.664	-2.83	B1	0.26	0.20	22000 ± 1000	5.0 ± 0.5	B2 V	yes	ELS	PBe	2
2.4661.3655	…	0.02	-0.08	15.789	-2.70	B1	0.12	0.16	18000 ± 1000	5.0 ± 0.5	B3 V	yes	ELS	PBe	…
1.4660.122	SC11 251205	-0.18	0.04	16.304	-2.19	B2	0.20	0.16	17000 ± 1000	5.0 ± 0.5	B4 V	yes	ELS	PBe	1
1.4539.345	SC11 162947	-0.23	-0.17	16.744	-1.75	B3	0.35	-0.08	17000 ± 1000	5.0 ± 0.5	B4 V	yes	ELS	PBe	1
1.4540.58	SC11 162373	-0.24	-0.15	15.320	-3.17	B1	0.23	0.13	17000 ± 1000	5.0 ± 0.5	B4 V	yes	ELS	PBe	2
1.4540.90	…	-0.10	-0.01	15.460	-3.03	B1	0.14	0.06	17000 ± 1000	5.0 ± 0.5	B4 V	yes	ELS	PBe	…
1	…	0.02	-0.45	16.954	-1.54	…	…	-0.04	19000 ± 1000	5.0 ± 0.5	B2-B3 V	yes	ELS	…	…
79.4659.3425	SC11 338327	-0.30	-0.23	14.948	-3.55	B0	0.18	-0.01	19000 ± 1000	3.5 ± 0.5	B2-B3 V	yes	ELS	PBe	…
1.4538.126	SC11 156984	0.02	-0.06	16.218	-2.28	B2	0.27	0.05	17000 ± 1000	5.0 ± 0.5	B4 V	yes	ELS	PBe	2
1.4540.426	SC11 172759	-0.30	-0.08	17.076	-1.42	B3	…	…	26000 ± 1000	5.0 ± 0.5	B1 V	yes	ELS	…	…
1.4660.719	…	1.02	1.47	19.127	0.63	…	0.18	0.49	…	…	…	…	ELS	…	…
1.4417.219	…	-0.07	-0.25	16.673	-1.82	B2	0.23	0.03	17000 ± 1000	5.0 ± 0.5	B4 V	yes	ELS	PBe	…
1.4417.105	…	-0.07	-0.43	15.881	-2.61	…	-0.02	-0.03	17000 ± 1000	5.0 ± 0.5	B4 V	yes	ELS	PBe	…
1.4418.87	…	-0.12	-0.32	15.497	-3.00	B1	-0.03	-0.01	18000 ± 1000	5.0 ± 0.5	B3 V	yes	ELS	PBe	– –
1.4418.102	SC11 76718	-0.21	-0.10	15.984	-2.51	B2	0.07	-0.01	17000 ± 1000	5.0 ± 0.5	B4 V	yes	ELS	PBe	…
1.4418.59	SC13 233437	-0.30	-0.22	15.260	-3.23	B1	0.26	0.14	17000 ± 1000	3.5 ± 0.5	B4 V	yes	ELS	PBe	2
79.4659.3412	SC11 338231	-0.13	0.09	14.808	-3.69	B0	0.31	0.11	17000 ± 1000	5.0 ± 0.5	B4 V	…	ELS	PBe	2
1.4537.174	SC11 151418	-0.23	-0.21	16.457	-2.04	B2	-0.11	-0.02	17000 ± 1000	5.0 ± 0.5	B4 V	No	CELS	PBe	2
1.4539.149	SC11 162389	-0.22	-0.18	16.095	-2.40	B2	0.16	0.01	18000 ± 1000	5.0 ± 0.5	B3 V	yes	CELS	PBe	…
1.4550.68	SC13 170089	-0.54		18.423	-0.07	G1	0.21	0.80	4200 ± 100	3.0 ± 0.5	K3-K4 III	yes	CELS	Giant	…
79.4659.3485	SC13 244640	1.53	1.30	16.738	-1.76	K4	0.23	0.75	4200 ± 100	3.0 ± 0.5	K4 III	yes	CELS	Giant	…
1.4539.197	SC11 162462	-0.16	-0.12	16.351	-2.14	B2	-0.04	0.11	15000 ± 1000	5.0 ± 0.5	B5 V	yes	CELS	PBe	…
1.4539.399	SC11 162907	-0.22	-0.20	17.044	-1.45	B3	-0.09	0.10	17000 ± 1000	5.0 ± 0.5	B4 V	yes	CELS	PBe	1
2.4660.6602	SC11 251619	-0.20	-0.14	17.305	-1.19	B2-B3	0.34	-0.06	17000 ± 1000	5.0 ± 0.5	B4 V	yes	CELS	PBe	…
2.4660.6678	SC11 251662	-0.19	-0.12	16.919	-1.57	B3	0.11	0.07	17000 ± 1000	5.0 ± 0.5	B4 V	yes	CELS	PBe	1
2.4660.6379	SC11 251229	-0.19	-0.13	16.039	-2.45	B2	0.13	0.01	17000 ± 1000	5.0 ± 0.5	B4 V	yes	CELS	PBe	…
2.4661.3816	SC11 257574	-0.10	0.09	17.184	-1.31	B4	0.37	0.15	17000 ± 1000	5.0 ± 0.5	B4 V	yes	CELS	PBe	1
2.4661.3843	SC11 257702	-0.14	-0.14	17.102	-1.39	B4	0.13	-0.09	17000 ± 1000	5.0 ± 0.5	B4 V	yes	CELS	PBe	…
2.4782.2161	SC11 350745	-0.19	-0.13	16.136	-2.36	B2	0.15	0.16	17000 ± 1000	5.0 ± 0.5	B4 V	yes	CELS	PBe	2
1.4539.152	SC11 163820	-0.17	-0.24	15.689	-2.80	B1	0.15	-0.15	19000 ± 1000	5.0 ± 0.5	B2-B3 V	yes	CELS	PBe	…
1.4539.157	…	-0.35	0.09	15.813	-2.68	B1	0.02	0.03	17000 ± 1000	5.0 ± 0.5	B4V	yes	CELS	PBe	1
1.4539.184	SC11 165078	-0.22	-1.69	15.833	-2.66	B1	-0.17	-0.09	18000 ± 1000	5.0 ± 0.5	B3V	yes	CELS	PBe	1
14	SC11 162906	-0.19	-0.17	16.944	-1.55	B3	0.32	-0.10	17000 ± 1000	5.0 ± 0.5	B4V	No	CELS	PBe	1
1.4660.191	SC11 251197	-0.13	-0.10	16.806	-1.69	B3	-0.01	0.07	17000 ± 1000	5.0 ± 0.5	B4 V	No	CELS	PBe	1
2.4661.4355	SC11 260000	-0.16	0.38	19.540	1.05	…	…	-0.07	…	…	…	…	CELS	…	…
2.4661.3880	SC11 257490	0.99	1.07	19.145	0.65	…	0.10	0.58	…	…	…	…	CELS	…	…
1.4661.117	SC11 257340	-0.18	-0.16	15.972	-2.52	B2	0.06	-0.02	17000 ± 1000	5.0 ± 0.5	B4 V	yes	CELS	PBe	…
1.4661.204	SC11 257393	-0.05	-0.06	17.210	-1.28	B4	0.04	0.05	22000 ± 1000	5.0 ± 0.5	B2 V	No	CELS	PBe	…
21	SC11 257392	-0.15	-0.12	16.304	-2.19	B2	0.14	-0.06	20000 ± 1000	5.0 ± 0.5	B2-B3 V	yes	CELS	PBe	…
1.4660.632	SC11 251213	-0.11	-0.10	16.936	-1.56	B3	…	…	…	…	…	…	CELS	…	…
1.4539.93	SC11 162357	-0.22	-0.19	15.465	-3.03	B1	0.09	-0.06	18000 ± 1000	5.0 ± 0.5	B3 V	yes	CELS	PBe	…
1.4539.386	SC11 251459	-0.03	-0.13	17.255	-1.24	B4	0.33	0.03	17000 ± 1000	5.0 ± 0.5	B4 V	yes	CELS	PBe	…
1.4539.80	SC11 162290	1.50	1.50	16.342	-2.15	K4	0.21	0.79	4000 ± 100	3.0 ± 0.5	K4 III	yes	CELS	Giant	…

Table 2.1: Stellar parameters derived from colors following the Calibration of Lang (1992) and (Wisniewski & Bjorkman 2006, and references therein) for main-sequence stars. Spectral types calibration for giants come from Kitchin (2004). The results of the SED fitting using Kurucz and NextGen models are given in cols 10 to 12. Column 14 gives the classification obtained from WFI spectra discussed in Section 2.3: Emission-line stars (ELS), candidate emission-line stars (CELS), stars without emission peak in Hα (NELS). Column 15 gives the diagnostic about the nature of the object following the analysis described in Section 2.4. *References*: Stars cataloged in (1) Wisniewski & Bjorkman (2006); (2) Sabogal et al. (2005).

Table 2.2: Wide-field Infrared Survey Explorer (WISE) magnitudes from the *Spitzer* archive.

MACHO ID	W1 [3.4μm] WISE (mag)	W2 [4.6 μm] WISE (mag)	W3 [12 μm] WISE (mag)	W4 [22 μm] WISE (mag)
1.4539.134	15.159 ± 0.058	15.355 ± 0.098	< 13.483*	< 10.042*
79.4659.3417	13.272 ± 0.030	13.156 ± 0.033	< 11.548*	< 8.565
1.4661.1151	14.819 ± 0.048	15.079 ± 0.105	9.672 ± 0.037	9.099 ± 0.42
2.4661.3655	14.234 ± 0.047	14.284 ± 0.049	11.228 ± 0.155	< 9.755*
1.4540.426	14.566 ± 0.043	13.111 ± 0.029	9.151 ± 0.023	7.000 ± 0.048
1.4418.59	14.764 ± 0.044	14.475 ± 0.046	10.627 ± 0.061	8.758 ± 0.222
79.4659.3412	13.718 ± 0.032	13.047 ± 0.034	< 11.887*	< 7.889*
1.4550.68	12.691 ± 0.028	12.790 ± 0.027	10.533 ± 0.043	7.585 ± 0.066
79.4659.3485	13.612 ± 0.039	13.770 ± 0.045	11.761 ± 0.207	< 9.224*
2.4661.3880	11.913 ± 0.106	12.254 ± 0.095	6.693 ± 0.037	4.517 ± 0.030
1.4539.80	12.704 ± 0.027	12.838 ± 0.027	12.610 ± 0.274	< 9.751*

Notes: Values with asterisks (*) indicate that these are not used when fitting the observed SEDs as higher quality value are available.

2) the data from the Wide-field Infrared Survey Explorer (WISE, Wright et al. 2010). The corresponding catalog is available from the NASA/IPAC Infrared Science Archive[3]. Wright et al. (2010) mapped the whole sky in bands centered at wavelengths of 3.4, 4.6, 12, and 22 μm, with angular resolutions of 6.1″, 6.4″, 6.5″, and 12″, respectively. The result of the cross-matching of WFI sources with those catalogs is shown in Tables 2.2 and 2.3, in which the corresponding magnitudes are provided.

2.3.4 Optical Hα Images and CO emission maps

The Hα images from the Magellanic Cloud Emission-Line Survey (MCELS, Smith & MCELS Team 1999) were also used to get more constraints and information on this region. The MCELS survey of the LMC and SMC was performed with the Curtis Schmidt Telescope at the Cerro Tololo Inter-American Observatory (CTIO). The images have an angular resolution of 3″, and were taken with a narrow band interference filter centered on the Hα line (λ_c = 6563 Å, $\Delta\lambda$ = 30Å). The Hα images were grouped in a mosaic to cover the central $8^\circ \times 8^\circ$ of the LMC. To infer the star formation in the last few million years and determine whether a recent triggering has taken place, we extracted from the mosaic the region covering the LMC clusters NGC 1850, NGC 1855, NGC 1858, and the expanding-shell structure associated with the emission nebulae LHA 120-N 103A and LHA 120-N 103B (Henize 1956) as shown in Fig. 2.2. Furthermore, we used ^{12}CO emission maps of molecular clouds from the Magellanic Mopra Assessment (MAGMA) survey to identify the areas with the largest amounts of CO in the LMC NGC 1850 star-formation region. MAGMA is a high angular resolution ^{12}CO ($J = 1 \rightarrow 0$) mapping survey of giant molecular clouds in the LMC and SMC using the Mopra Telescope, which is situated near Coonabarabran, Australia. At 115 GHz, the Mopra Telescope has a 33″ FWHM beam-size. The full MAGMA LMC data were presented by Wong et al. (2011), and the final resolution of the maps after reduction is close to 45″ (i.e., 11 pc at the distance of the LMC) sampled onto a grid-spacing of 15″, and a channel spacing of 0.526 km s^{-1}. The MAGMA ^{12}CO contours also are marked in the Fig. 2.2.

[3] http://irsa.ipac.caltech.edu/

2.4 Analysis and results

2.4.1 Stellar classification of the stars in the LMC NGC 1850 region

The stellar classification of all Hα ELS in our sample was carried out using various methods such as photometric stellar classification based on ranges in absolute magnitudes, loci in NIR color-color diagrams, and fitting of synthetic spectra to observed spectral energy distributions (SEDs). We were able to identify the evolutionary stage of ELS, as well as to determine the values of their physical parameters. The following sections describe the methods used to classify those stars.

Photometric stellar classification

The MCPS and OGLE-II colors and apparent magnitudes needed to be converted into absolute values to estimate the spectral types of our ELS. The $V_0 = V - 3.1 \times E(B-V)$ parameter and the dereddened $(B-V)_0$ and $(V-I)_0$ colors were calculated using $E(B-V) = 0.17 \pm 0.03$, taking into account the galactic foreground $E(B-V)_{GAL} = 0.07$ and the mean extinction in the LMC bar $E(B-V)_{LMC} = 0.10$ given by Fitzpatrick (1986). It also corresponds to the value inferred by Fischer et al. (1993) for the NGC 1850 star-forming region. Also, we used an extinction-to-reddening ratio of $A_V/E(B-V) = 3.1$ as given by Fischer et al. (1993). The parameters are shown in columns 3 and 4 of Table 2.1.

The M_V of each star was calculated from the resulting V_0 and adopting a distance modulus $\mu = 18.493 \pm 0.008$ mag, corresponding to the distance to the LMC bar obtained by Pietrzyński et al. (2013) from eclipsing binaries. The results are listed in column 6 of Table 2.1. The uncertainty of M_V is given in terms of V_0 and the corresponding distance modulus adopted. The stars in the sample have absolute visual magnitudes between -3.69 and 1.05 magnitudes.

Individual spectral types were assigned by applying the calibration of Lang (1992) and Wisniewski & Bjorkman (2006, and references therein) for main-sequence stars as shown in column 7 of Table 2.1. Both intrinsic colors between $-0.4 \leq (B-V)_0 \leq 0.1$, $-0.35 \leq (V-I)_0 \leq 0.2$, and absolute magnitude between $-4.2 \leq M_V \leq 0.43$ are indicative of a spectral type B or earlier, according to the calibration given by Lang (1992). We assumed a luminosity class IV or V for the main-sequence stars and we adopted the color relation for giants when $0.33 \leq (B-V)_0 \leq 1.57$, since the values of M_V and intrinsic colors suggest a luminosity class II or III (e.g., Kitchin 2004).

Near-infrared color-color diagram

In Fig. 2.5 we plot the dereddened IRSF colors of the stars in our sample as well as the regions of classical T-Tauri stars (CTTS), Herbig Ae/Be (HAe/Be) stars, classical Be stars. The stars colors were corrected for interstellar reddening using the relations from Bessell & Brett (1988) and an interstellar extinction value of $E(B-V) = 0.17 \pm 0.03$ mag (Fischer et al. 1993; Fitzpatrick 1986):

$$(J-H)_0 = (J-H) - E(J-H), \tag{2.1}$$

$$(H-K)_0 = (H-K) - E(H-K), \tag{2.2}$$

$$E(J-H) = 0.37 \times E(B-V), \tag{2.3}$$

$$E(H-K) = 0.19 \times E(B-V), \tag{2.4}$$

The intrinsic colors of dwarf and giant stars were taken from Bessell & Brett (1988) and Hernández et al. (2005). As a limitation of our methodology, it was not possible to determine the contribution of the intrinsic

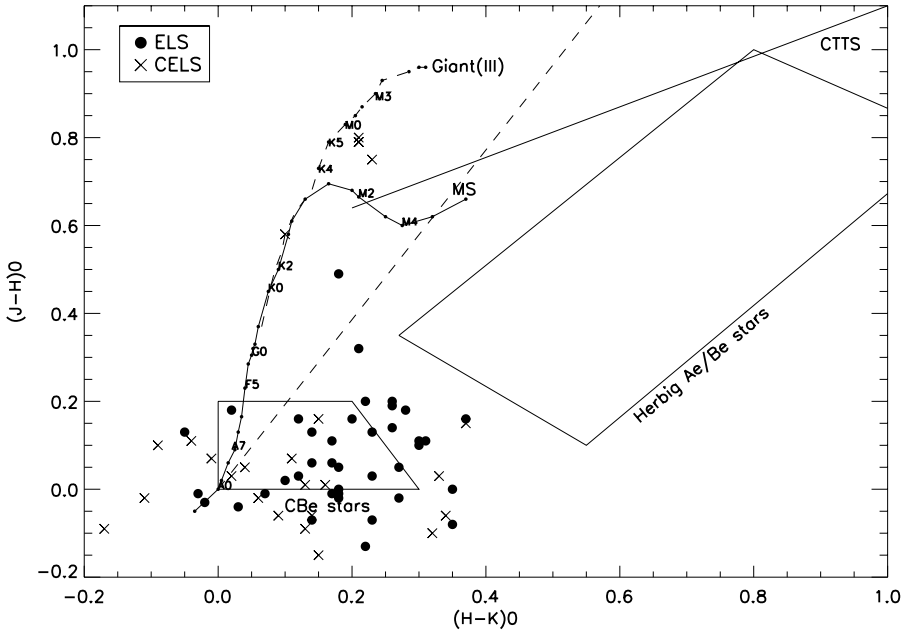

Figure 2.5: NIR color-color diagram based on IRSF magnitudes corrected for interstellar reddening for the stars of the Table 2.1. The location of the main sequence and giant stars from Bessell & Brett (1988), classical T-Tauri stars (CTTS) from Meyer et al. (1997), classical Be (CBe) stars from Dougherty et al. (1994), and Herbig Ae/Be stars from Hernández et al. (2005) are also shown. The dashed line indicates the direction of interestellar reddening of a standard A_0 star. This line is calculated for $R_V = 3.1$ with the reddening law of Cardelli et al. (1989).

circumstellar extinction for each star in our sample, which is naturally associated with the amount of dust and gas in the disk obscuring the star. It can be noted in Fig. 2.5 that several of the stars are found in the region of CBe stars. Despite the good correlation between the NIR classification, SED shape, and spectral type estimate, we are aware that additional spectroscopic observations are needed to definitely confirm the Be stars status of some ELS.

Modeling the spectral energy distribution

We constructed SEDs for 61 stars in our sample using the $UBVIJHK_S$, IRAC, and WISE magnitudes at wavelengths from 0.3 μm to 22 μm in the $UBVIJHK_S$+IRAC+WISE systems shown in Tables 2.2 to 2.3. The remaining 3 stars of our sample did not have enough data to do the SED fitting. The ATLAS9 Kurucz ODFNEW/NOVER models (Kurucz 1993), the BT-NextGen (GNS93) models (Hauschildt et al. 1999), and the VO-tool VOSA[4] (Virtual Observatory SED Analyser) developed by the Spanish Virtual Observatory were used to fit theoretical SEDs to observed data. For this fitting process, we assumed for all stars the same interstellar extinction and the appropriate distance to the LMC bar, as discussed in Section 2.4.1. Magnitudes in each filter were transformed to fluxes using standard zero-point fluxes given in the VO-tools. The SEDs constructed with these fluxes were compared with atmosphere models from the Kurucz's grid and the NextGen database. The models with low metallicity were adopted for the entire sample, for which, upper and lower limits of the metallicity were established from the mean values of metallicity distribution derived by Carrera et al. (2008) for the chemical enrichment history of the LMC. The best fitting model of the observed data given by VOSA is

[4]http://svo2.cab.inta-csic.es/theory/vosa/

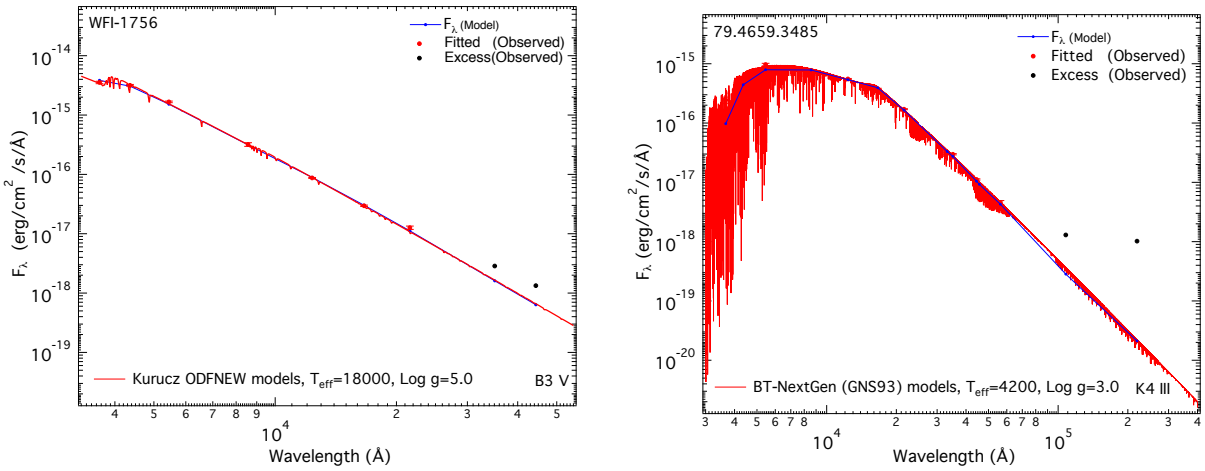

Figure 2.6: Examples of SEDs fitting with synthetic spectra using the VO-tool of B3 V ELS, and of a K4 III giant with IR excess.

the one that minimizes the value of the reduced χ^2 defined as:

$$\chi^2 = \frac{1}{N-P}\sum\Big(\frac{1}{\sigma^2}(Y_0 - M_D \times Y_m)^2\Big), \tag{2.5}$$

where Y_0 is the observed flux, σ the observational error in the flux, N the number of photometric points, P the number of parameters being fitted, Y_m the theoretical flux predicted by the model, and M_D the multiplicative dilution factor to the distance of LMC. For further information about the fitting procedure see Bayo et al. (2008). If a magnitude at a given band is available in different databases, we chose the one with the highest accuracy. This was indeed the case for the *BVI* bands, where OGLE II data were always preferred instead of MCPS, due to the fact that time-averaged values were used for the construction of the OGLE II databases for the *B*,*V* and *I*-band. Furthermore, color corrections were derived and added and only objects with more than 5, 10 and 40 good observations in the B, V, and I bands, respectively, were included in the final photometric map of the LMC (see Udalski et al. 1998a,b; Szymanski & Udalski 1993).

Similarly, IRSF NIR bands JHK_S were used instead of 2MASS data. The IRSF survey reached objects ~ 2 mag fainter than 2MASS, and resolved neighboring objects located down to $\sim 1.25''$ apart, compared with the spatial resolution $\sim 2''$ of 2MASS. Although the J, H and K_S filter bandpasses in the IRSF survey follow the specification of the Mauna Kea Observatories NIR filter set, they are not identical to those of 2MASS. Nevertheless, the uncertainties derived from the transformations between the IRSF and 2MASS systems are less than 1% (Kato et al. 2007). This was taken into account when estimating the uncertainties of the SED fitting.

In columns 10 to 12 of Table 2.1, the effective temperature, superficial gravity, and spectral type values coming from the best fit of Kurucz and NextGen models for the sample stars SEDs are provided. The accuracy in determining these parameters was determined by the model grid size of 1000 K in $T_{\rm eff}$ for Kurucz models, 100 K in $T_{\rm eff}$ for NextGen models, and 0.5 in $\log g$ for both models. In Fig. 2.6 two examples of SED fits are shown. The stellar parameters derived from the SEDs are independently obtained from those derived from the intrinsic color in Section 2.4.1. The agreement between temperatures and spectral types derived in both ways supports the reliability of the results and indicate that the stellar parameters are fairly constrained. It is important to recall that due to the lack of spectra the interstellar extinction that was used is a global value for the field, while it is seen in Fig. 2.1 that this field is very complex and the local reddening value can be different

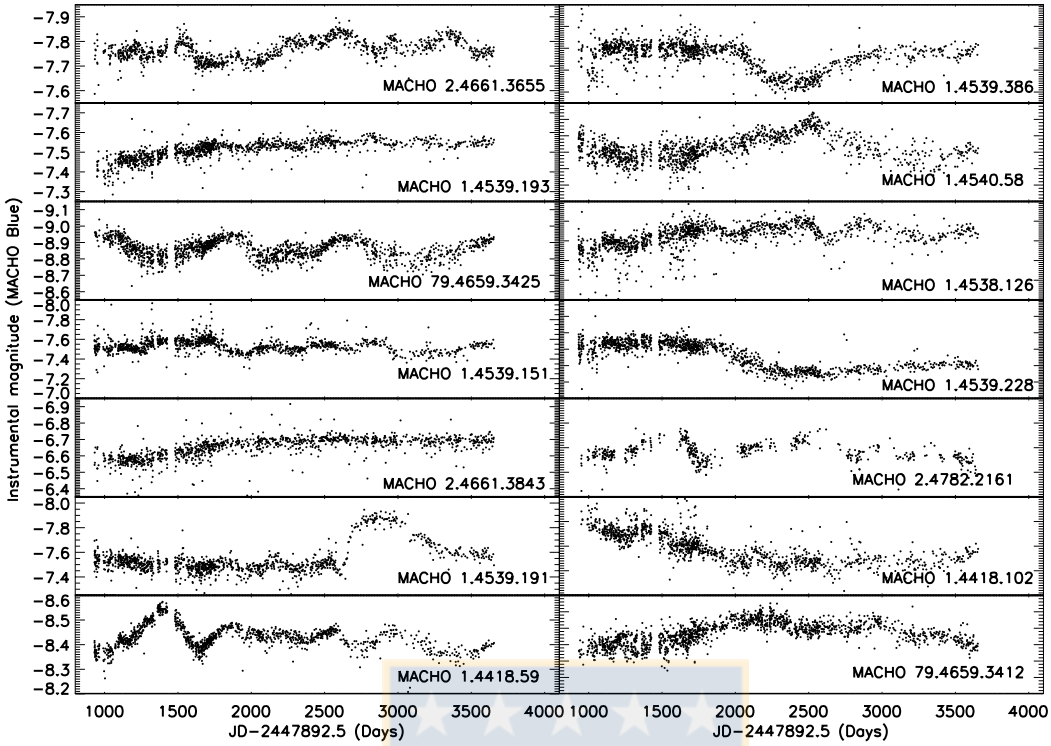

Figure 2.7: Examples of MACHO B-band lightcurves of PBe stars in our sample, showing irregular variability, outburst, or fading.

for each star. The combination of color-color diagram and SED fitting allowed to confirm the suspected nature of 54 Be stars for the 64 stars in the sample. In addition the lightcurves also provide some insight about their Be status as it is shown in Fig. 2.7 and Section 2.4.2.

2.4.2 Photometric variability

Another important piece of information about the nature of the 64 stars of our sample is their photometric variability. The variable nature of emission-line stars is an important feature related to the stellar evolution stage (Diago et al. 2008). In general, Herbig Ae/Be are known for their photometric variability on timescales of days to weeks, and generally show strong excess radiation above photospheric levels in the infrared and millimeter wavelength region. The nature of the variability is such that no definite period can be attributed to it and the amplitude of the variability is not constant, although in some cases it seems that secular changes follow a cyclical pattern on a timescale of several years (Herbst & Shevchenko 1999). On the other hand, the photometric variability (sudden brightening, fading episodes, or long-term brightness changes) in Be and B[e] stars is due to various possible mechanisms such as mass-loss through stellar winds, rapid rotation and/or non-radial pulsations (Porter & Rivinius 2003). Furthermore, giant stars pulsate with long periods (Catelan 2009). Therefore, the detection of variability periods may also help to differentiate between the different kinds of objects.
We searched the lightcurves of the stars in our sample in the OGLE-II and MACHO databases. The MACHO survey provides photometric instrumental magnitudes for each star in two contiguous “blue” and “red” passbands, labeled B and R, at different wavelengths than the standard B and R passbands in the Johnson-Cousins photometric system (Alcock et al. 1999). The MACHO light curves have between 500 to 1300 points per star,

depending on the filter with which were taken with good photometric accuracy errors. The MACHO photometry was accumulated over the interval of 8 years from July 1992 to January 2000. Among our 64 stars, 7 are not included in the MACHO database and 9 more do not have measured errors in their photometry and were thus discarded.
The OGLE-II lightcurves were also available, with an average 270 data points each one spanning 3 years between October, 1997 and November, 2000. It was possible to obtain the OGLE lightcurve for 7 of the 9 stars without a MACHO lightcurve. Similarly, we retrieved from OGLE the lightcurve for 3 of the 7 stars that have a MACHO lightcurve without photometric errors.
Among the 58 stars identified in our sample with an available lightcurve, and based on their lightcurves, their position in the NIR color-color diagram, and their stellar parameters derived from their colors and SED fitting, we consider 54 of them to be potential Be (PBe) stars since they show outbursts, bumps, fading events or long-term trends lasting up to thousands of days, typical characteristics of Be stars (Mennickent et al. 2002). Some examples of the light curves from the MACHO database for these stars are shown in Fig. 2.7.
To get further insight on the nature of those 54 PBe stars we analyze their lightcurves in search of periodicity. We apply the chisquare fitting method from Palmer (2009), shown to be better than the IRAF PDM or the FFT search with Period04 (Lenz & Breger 2005). No clear period was found; this can be attributed to the low quality of MACHO data, but it is also consistent with stochastic photometric variability in several time-scales, and episodes of quasi-periodic oscillations, which are often observed in Be stars (e.g. Mennickent et al. 2002).

2.4.3 On the nature of the emission-line objects in the NGC 1850 region

The diagnostics described in the previous sections, plus the spatial stellar distribution seen lead us to conclude that we have found 54 PBe stars with masses up to 17 $M_{\odot}$, according to the calibration of spectral types for main sequence stars given by Huang & Gies (2006). We note that the PBe stars have spectral types B1-B3, since the maximum probability of occurrence of the Be phenomenon is for spectral types around B2 (Zorec et al. 2007). But it is likely that there exist spurious effects due to the precision in the determination of the spectral types and the incompleteness of the data in our sample. This effect will be studied in detail in a subsequent work with a more statistically significant sample.
By the other hand, our estimated ages for the PBe stars agree with the predictions by Ekström et al. (2008), that stars with ages between 10 Myr and 25 Myr are the fastest rotators. In addition to the PBe stars, we have found 3 giant stars and one Cepheid variable at the NGC 1850 field. The classification and derived parameters for all these objects are shown in Table 2.1.

2.5 Discussion

2.5.1 Age estimate and spatial distribution of stellar populations in the WFI field surrounding NGC 1850

Age estimates and stellar populations of our extracted WFI field

In order to investigate the spatial distribution of the identified stellar populations surrounding the cluster NGC 1850 and their estimated ages, we use an $11' \times 8'$ WFI-frame centered on the OB association NGC 1850, corresponding to $\simeq 160\,\mathrm{pc} \times 116\,\mathrm{pc}$ in the LMC (see the dashed black box in Fig. 2.2). The age estimate of stars located in NGC 1850 and its vicinity was performed using isochrone fitting of optical color-magnitude diagrams (CMDs). The isochrones with $z = 0.008$ from Lejeune & Schaerer (2001) were used to estimate the age of each population in the entire WFI field. The young and main-sequence stars are estimates by three

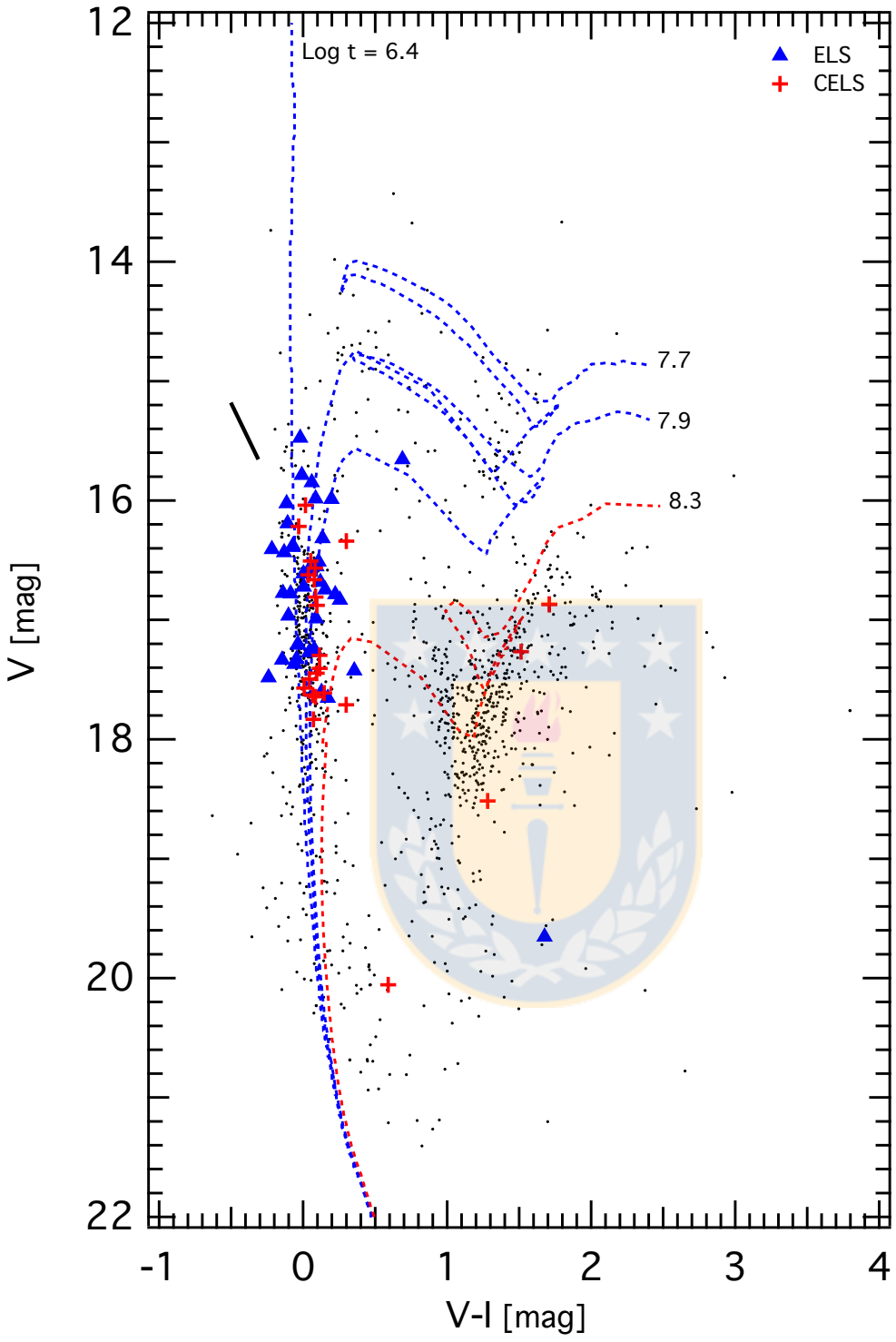

Figure 2.8: The CMD for all stars with WFI spectra in the field surrounding NGC 1850 ($11' \times 8'$ frame centered on the cluster NGC 1850). The CMD is based on the OGLE-II standard VI photometry in the LMC (Udalski et al. 2000). Emission-line stars are show by special symbols as defined on the image. Four isochrones are also shown (Lejeune & Schaerer 2001) for stars with the metallicity $Z = 0.008$ and age ($\log t$) labeled in the image. We adopted these isochrones using $V - M_v = 18.493 \pm 0.008$, $E(V-I) = 0.21$ and $A_v = 2.5 \cdot E(V-I)$. The reddening vector is indicated by the upper oblique line. The absence of a dense low main sequence for the isochrones is not physical but due to the fact that only stars with WFI spectra are shown.

reference isochrones of 2.5 Myrs, 50 Myrs, and 79 Myrs, while the old population of red giant stars is fitted by an reference isochrone of 200 Myrs. The comparison with the isochrones displayed in Fig. 2.8, allows us to estimate ages for the different populations in our field. These estimates are in fair agreement with those of Gilmozzi et al. (1994, and references therein) who give an age range of 50 Myrs to 120 Myrs for the old cluster, and 1 Myrs to 11 Myrs for the young cluster. The entire WFI sample of stars is plotted in the CMD shown in Fig. 2.8. In the same figure, the reference isochrone fits are also shown. One can see the corresponding different populations of stars: on the one hand, a population comprised of a mixture of very young stars with slightly older main sequence stars, and on the other hand a population of more evolved stars (mostly giants). This indicates that NGC 1850 went through different episodes of star formation, because intermediate mass stars can be found in pre-main sequence and main sequence areas, as can be see in Fig. 2.8. Clearly there is also a population of young stars in the main sequence.

Spatial segregation of stellar populations

The spatial localization of the various populations of our sample has also been studied, in particular for the emission-line stars, the young stars, and the evolved giant stars populations. For this reason, we used the *Spitzer*-IRAC 8.0 μm image of the SGS 6 complex available under the "SAGE" legacy program (Meixner et al. 2006). The angular resolution of IRAC is $\sim 2''$, corresponding to 0.5 pc at the distance of LMC (49.97 ± 0.19 kpc, Pietrzyński et al. 2013). Fig. 2.9 shows a portion of the *Spitzer*-IRAC 8.0 μm image covering the LMC clusters NGC 1850 and the supergiant shell SGS 6 complex, which is discussed in Section 2.5.2. Fig. 2.9 clearly displays the structure of the H II region, which shows filamentary structures due to ionizing star clusters and massive stars present in the field. It is worth noting that most of the strong nebulosity seen in the Spitzer image (Fig. 2.9) becomes transparent in Hα (Fig. 2.2). This implies that the cloud is not an issue regarding the detection of the stars, and that the (sufficiently luminous) main-sequence or massive pre-main sequence stars should be detectable at all locations in our $\sim 11' \times 8'$ frame centered on the cluster NGC 1850.

As expected, most main-sequence and pre-main-sequence stars appear to be located in the central region of NGC 1850. However, in the west side of the cluster the field appears to have a low star-density, while on the east and southeast side of NGC 1850 the density of giant stars is very high. The spatial location of those populations of stars is shown in Fig. 2.10. The location of the $\sim$ 200 Myr-old giant stars population could be explained by an older low-mass open cluster, that would have dissolved in about 100 Myrs. This is the average lifetime of low-mass clusters, according to Terlevich (1987). However, this would not explain why those stars are only located on one side of the open cluster. Possibly the expansion of the supergiant shells could play a role in this distribution. We discuss this in more detail in Section 2.5.2.

Ours emission-line stars shown in Figs. 2.9 and 2.11 appear to be spatially segregated by age. We can see that some of the main sequence and the pre-main sequence stars ones appear to follow filamentary structures seen in the infrared, as opposed to those seen in the optical in Fig. 2.2 and are distributed along to shell rim of SGS 6 complex, while CELS are distributed in the open cluster on the left side of shell rim (See, Fig. 2.10).This is discussed in more detail in Section 2.5.2.

2.5.2 Supergiant shell complexes in the LMC and the spatial distribution of ELS

Supergiant shells in the LMC

As it is mentioned above in this Ph.D thesis we have used the SGS and shell complexes defined by Dawson et al. (2013) to study their possible relationship with the areas of star formation, especially in the NGC 1850

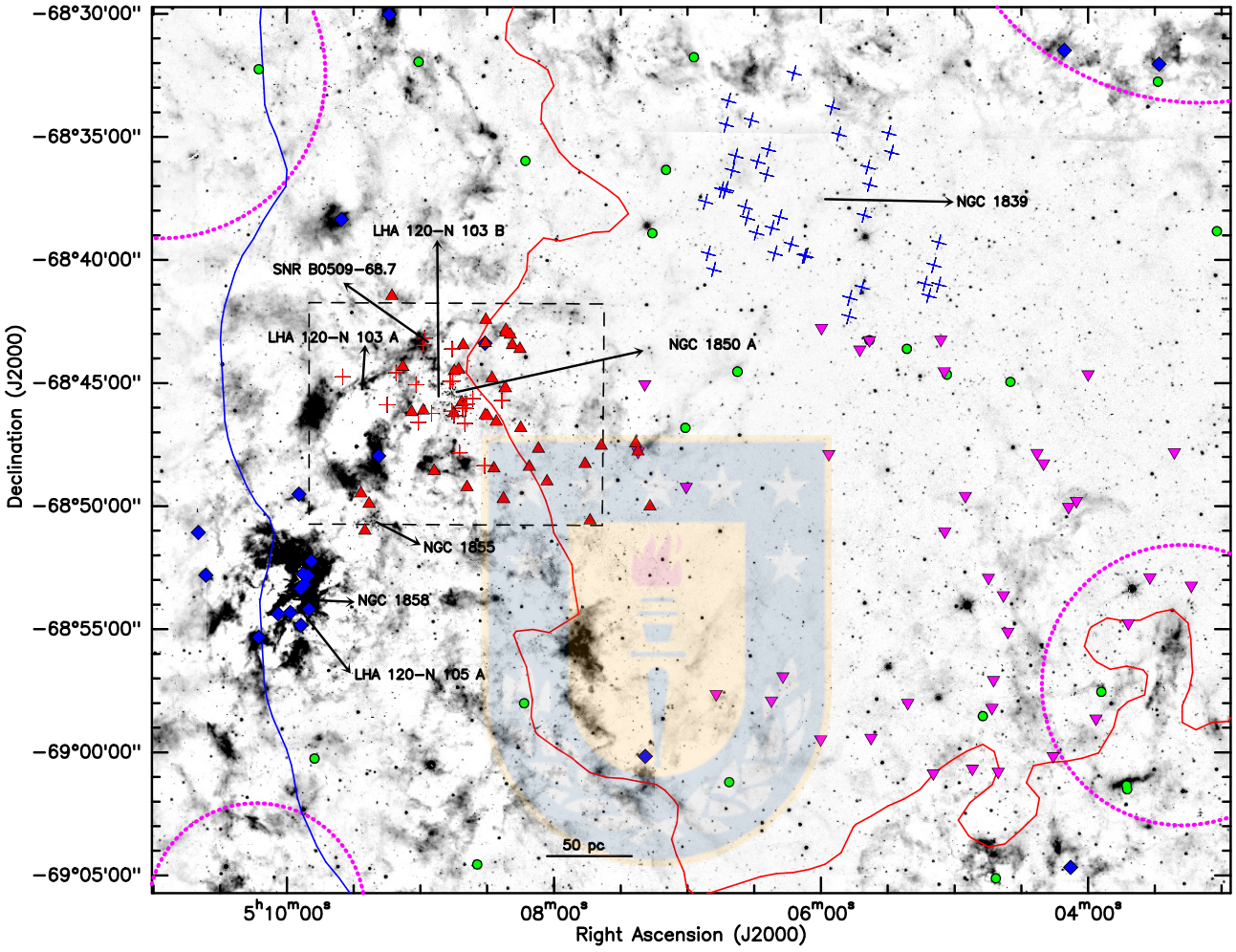

Figure 2.9: Spitzer 8.0 μm image on the center of cluster NGC 1850. The locations of the ELS (red triangles) and CELS (red crosses) are shown in the image. YSOs from Gruendl & Chu (2009) are shown in blue diamonds, B stars with hydrogen in emission from Iqbal & Keller (2013) are marked with blue crosses, ELS from Reid & Parker (2012) are marked with green circles, and ELS with high resolution spectra in the ESO archive (This refers to our dataset of ESO-Flames spectra which are being analyzed) appear in magenta inverted triangles. The dashed black box shows part of the WFI-slitless field for which all WFI spectra were extracted. The blue and red solid lines represent the inner and outer edges of the SGS 6 complex, respectively, discussed in Section 2.5.2. North is up, east to the left.

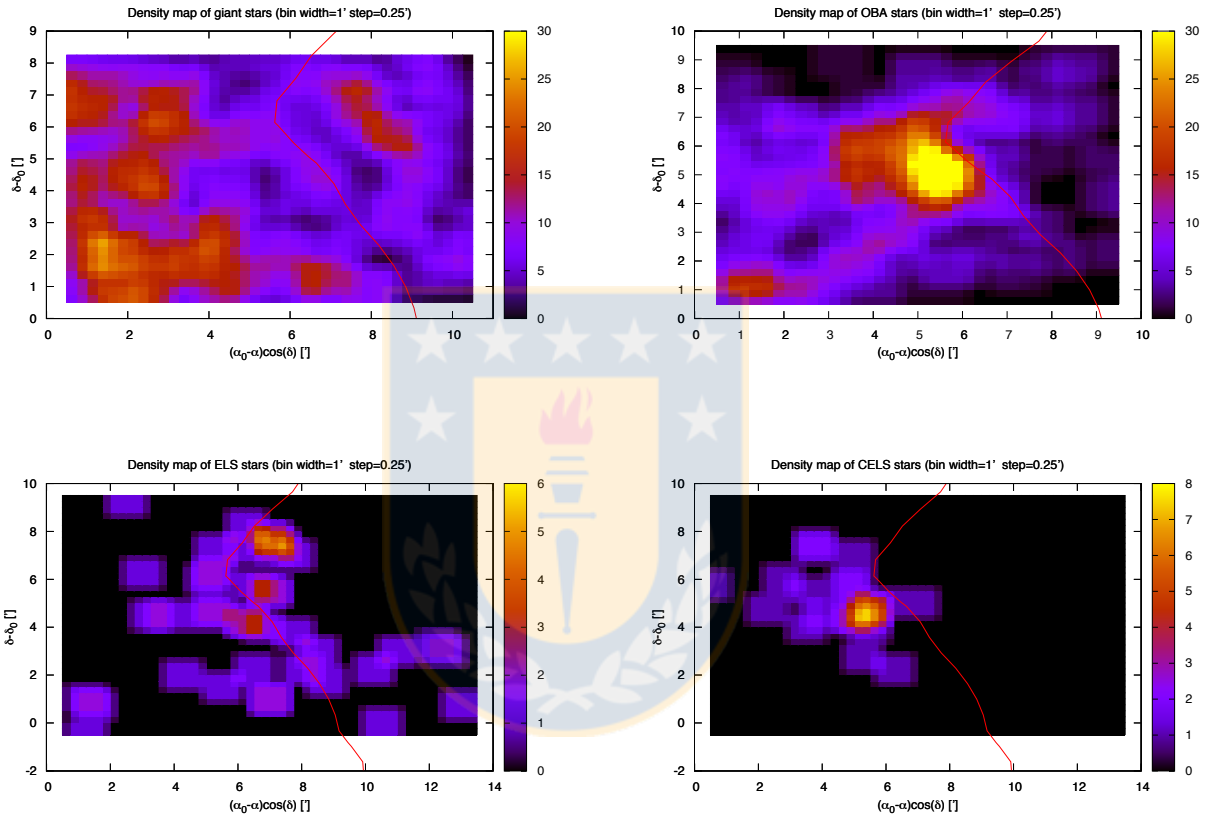

Figure 2.10: Star-position distribution maps around NGC 1850. Density maps of normal stars based on the population of OBA stars and Giant stars in the WFI-slitless field for which all WFI spectra were extracted (upper panels), density maps of ELS and CELS in our sample of 64 stars (bottom panels). The red solid lines represent the inner edge of the SGS 6 complex. Bright regions indicate high density and the units of color scale are $Nstars \cdot arcmin^{-2}$.

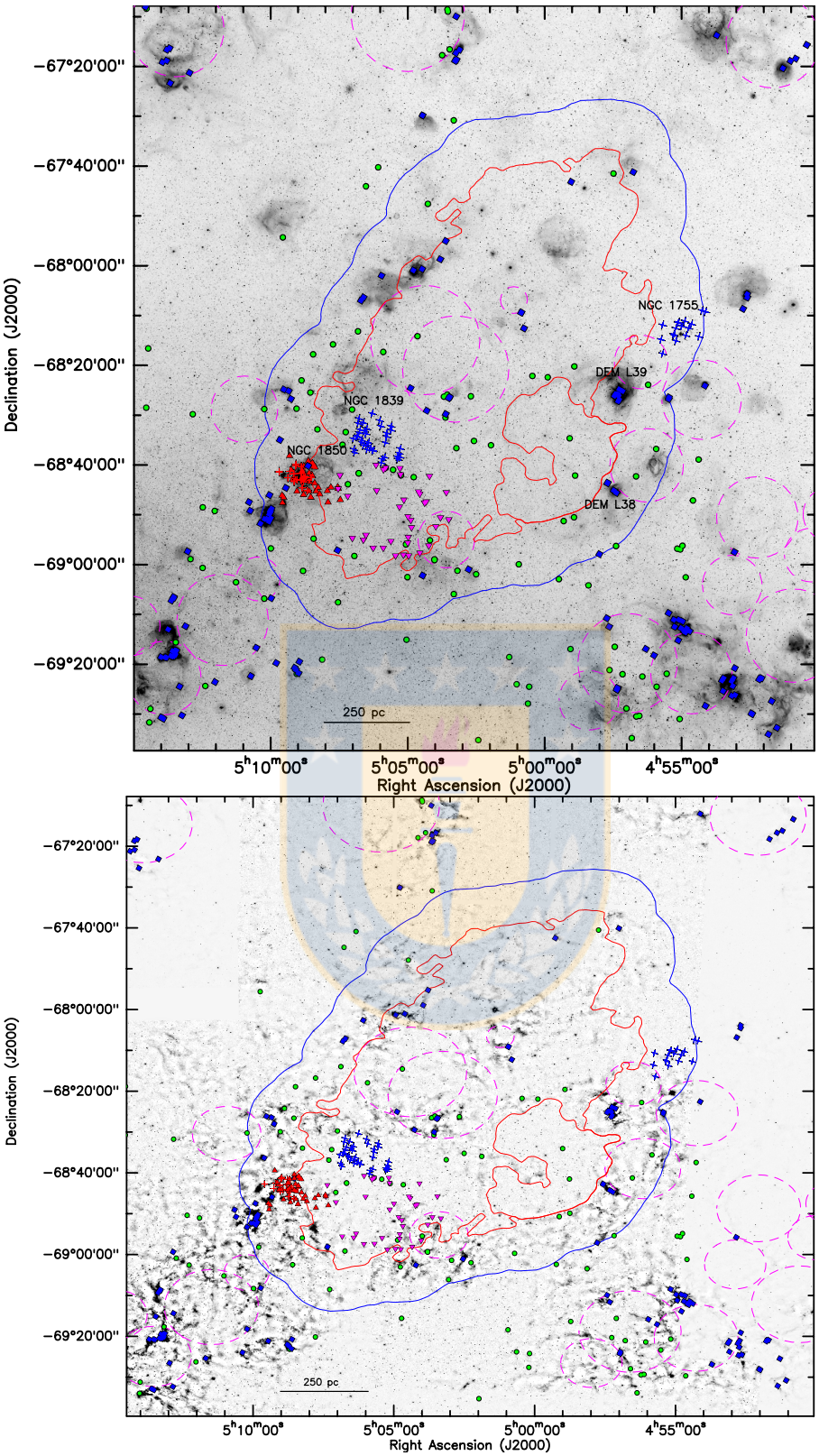

Figure 2.11: SGS 6 complex overlaid on MCELS Hα emission (upper panel) and *Spitzer* 8 μm emission (bottom panel). The position of the cluster NGC 1850 in the SGS 6 complex is marked, together with the localization of ELS (red points) and CELS (red crosses) from WFI. We further marked definitive YSOs (blue diamonds) from Gruendl & Chu (2009), ELS from Reid & Parker (2012) are marked with green points, B stars with hydrogen in emission in the young clusters NGC 1839 and NGC 1755 from Iqbal & Keller (2013) are shown with blue crosses, and ELS with high resolution spectra in the ESO archive appear in magenta inverted triangles. Dashed circles are the H I GSs from Kim et al. (1999). North is up, east to the left.

region. Indeed we searched for a possible relationship between the location of ELS + CELS found with WFI and the ionized gas structures within the SGS complex.

Our region of interest coincides with the SGS complex labeled Complex 6 in Dawson et al. (2013), see Fig. 1.1. It consists of two overlapping shells: SGS5 and the smaller, better defined object known as LMC 6 or SGS2 in Kim et al. (1999). This region is shown in Fig. 2.11, where we have also plotted structures tentatively identified as GSs with radii given by Kim et al. (1999). These relatively smaller structures are better delineated in the *Spitzer* 8 μm emission (bottom panel of Fig. 2.11). In the same Fig. 2.11, are also shown YSO and ELS identified in this work and in the literature. They allow us to examine the locii of star formation and the process of gas compression by the expanding shock of the SGS in the SGS Complex 6.

Spatial distribution of ELS and star formation in the NGC 1850 SGS6 region

The position of the CO clouds in the star-forming region NGC 1850 shows that they are likely pre-existing clouds that have been compressed by the expansion of the SGS 6 complex (see, Fig. 2.2). These clouds are located only on one side of the shell, along its rim, as discussed by Book et al. (2009) for the molecular clouds associated with the OB associations LH 11 and LH 12 on the west side of the SGS 6 complex. Indeed, the clusters NGC 1850 A/B appear at the south-east edge of this SGS, on its compression zone.

Fig. 2.2 clearly shows the compression of the H II region LHA 120-N 103 B by the shell rim of the SGS 6 complex. The Hα filaments in the NGC 1850 cluster are considered to be shock fronts of the expanding shell.

The star formation process is typically associated with clouds where the gravitational collapse of pre-stellar cores gives rise to the embedded protostars. Thus, their association with these clouds may indicate a young-star nature. Fig. 2.11 shows that YSOs are associated with CO clouds and H II regions, being located at the center of these regions. This indicates an ongoing star formation in those zones.

A few YSOs are found in the central part of the SGS 6 complex, but are still embedded in some nebulosity while most of the YSOs are located along the shell rim. In the NGC 1850 star-forming region, many YSOs appear in the central part of the cluster NGC 1858 (south-east of NGC 1850), and there is a clear correlation between YSOs and molecular clouds (see Figs. 2.2 and 2.9). It seems that the formation of YSOs in the NGC 1858 cluster is related to local interstellar conditions. However, we note that this cluster has already suffered from the passage of the outer rim of the SGS 6 as shown in Figs. 2.2, 2.9, and 2.11. This SGS front might have triggered the star formation process.

However, the situation is less clear in the NGC 1850 cluster. There the molecular cloud has been almost completely exhausted and the sample of ELS consists of very young stars and slightly older stars, located in the interaction zone of the SGS 6 complex. In particular, its YSOs and young stars are mostly located in either the central part of the cluster or in its border, while some of its ELS appear to be located slightly out of the cluster in the filaments all around it. The ELS in this cluster appear to be formed on the side of CO clouds where the Hα filaments are located, suggesting that the formation of the ELS was triggered by the compression of the CO clouds by the expanding SGS shock. This specific spatial distribution of ELS in NGC 1850, which are composed of different types of stars in different early evolutionary stages, is in agreement with the notion that the expansion of SGSs and ionization fronts of massive stars compress the H II regions and molecular clouds, leading them to collapse, triggering episodes of star formation, just ahead of the ionization fronts. Therefore, one can expect that the star-formation episodes around NGC 1850 A/B and NGC 1858 are a natural consequence of this compression mechanism.

To further test this triggering mechanism of star formation, in Fig. 2.11 are also shown the YSOs identified by Gruendl & Chu (2009), ELS from Reid & Parker (2012), ELS from Iqbal & Keller (2013) and the ELS from ESO-archive with emission in Hα defined as candidate Be stars in the entire SGS 6 area. It appears that as in

the case of NGC 1858 and as explained above, the YSOs are located inside the dense molecular clouds, which collided or are colliding with the rim of a GS or a SGS.

While ELS appear to follow the remnants of the collisions (in the rim or in the filaments) or are in the field, revealing in advance the compression by the SGS and the passage of the ionization fronts. As one can see in Figs. 2.10 and 2.11, ELS are concentrated inside or around the edges of the SGS and GSs. This suggests that a certain fraction of these ELS were formed due to the dynamical effects of SGSs. Furthermore, this provides further evidence that the current star formation in the zone of the NGC 1850 cluster was triggered by the advance of the SGS 6 complex and the ionization fronts of massive stars, as suggested by Yamaguchi et al. (2001b) and Book et al. (2009) for other star-forming regions in the LMC. The distributions of GS, SGS, and ELS also suggest that some star formation occurs out of the open clusters, in the filaments of matter where there is enough material to form stars when the clouds suffer the encounter with the GS/SGS expansion. Some OB associations and possibly even less dense groups of stars outside of classical open clusters or associations could have been born by such a mechanism. Very few ELS are located in the central parts of SGS or GS and could be evolved stars with their original gas/dust blown away. Of course, the nature of the various ELS populations used in this part of thesis work must be spectroscopically confirmed.

Our results suggest that in the NGC 1850 region, star formation at scales of 100 pc to 250 pc would be driven mainly by the expansion of the SGSs, which is consistent with the morphological and dynamical evolution of the LMC (de Vaucouleurs & Freeman 1972; van der Marel et al. 2002; Alves 2004), which is supported by the almost constant velocity dispersion found in the LMC (Carrera et al. 2008, 2011). This guarantees that density waves in the spiral-arm do not a major role for stellar formation at the LMC at these scales.

2.6 Conclusions

Using the ESO WFI in slitless spectroscopic mode, together with existing images and photometry in different bands from the optical to the mid-infrared, we identify a sample of 38 ELS and 26 CELS in the open cluster NGC 1850 and its surroundings. Among these 64 stars, 60 are of spectral type B, and 57 are new detections. For most of them, OGLE or MACHO photometry and lightcurves were obtained. All this information was combined to perform an SED analysis, to find the infrared excess, to detect potential periodicity or variability of those objects, and finally to give some clues on the nature of those stars. In the sample of 64 Hα emission-line objects, 54 potential Be stars were identified with masses up to $17 M_{\odot}$, along with 3 giant stars and one Cepheid variable. Among the normal stars without emission, 3 different populations of stars were identified: i) PMS stars, ii) stars, including massive ones at the beginning of the MS, and iii) low-mass stars already evolved and in the giant stage. They all show the complexity of the star formation and evolution history of the NGC 1850 region.

The spatial distribution of the ELS and normal stars was analyzed, and some segregation was found with respect to the star's age/evolution and spectral type. It seems that the ELS are concentrated in the surrounding region of NGC 1850, as well as along the filaments of matter at the edges of the bubbles of the H II region. The younger ELS are preferentially located closer to the NGC 1850 cluster core. On the other hand, the spatial concentration of the ELS in NGC 1850 along the inner rim of the SGS 6 complex suggests that the currently forming generation of ELS is predominantly triggered by the feedback from the massive stars of the cluster, combined with the dynamical effect due to the expanding shell. This result was further tested in the entire SGS 6 complex and similar results are obtained for YSOs appearing in the core of dense molecular clouds that have just suffered a collision with the SGSs or GSs, while other ELS are more dispersed but still mainly follow the filaments, old remnants of previous collision of the SGS expansion with molecular clouds. These results are

also consistent with those from Yamaguchi et al. (2001b), indicating that the stars and clusters tend to form on the side facing towards the shell center. Both results suggest that the star formation episodes in and out of open clusters are triggered at the shell rim during the collision of the shell expansion with molecular clouds. Those results also show that the ELS appear to be good tracers of the star formation and evolution. This process of star formation will be further tested in larger fields of the LMC and the results will be presented in future work.

Table 2.3: Magnitudes for all ELS found with WFI in the open clusters NGC 1850, NGC 1855, and its surrounding field.

MACHO or WFI ID	RA J2000 (h m s)	DEC J2000 (o ' ")	U MCPS (mag)	B MCPS (mag)	V MCPS (mag)	I MCPS (mag)	B OGLE (mag)	V OGLE (mag)	I OGLE (mag)	J IRSF (mag)	H IRSF (mag)	K IRSF (mag)	[3.6μm] SAGE (mag)	[4.5μm] SAGE (mag)	[5.8μm] SAGE (mag)	[8.0μm] SAGE (mag)
1.4539.193	05:08:39	-68:49:29.1	16.090 ± 0.073	16.645 ± 0.028	16.544 ± 0.030	16.489 ± 0.104	16.570 ± 0.023	16.722 ± 0.014	16.718 ± 0.029	16.66 ± 0.02	16.64 ± 0.04	16.54 ± 0.08	15.402 ± 0.043	15.385 ± 0.047	…	…
1.4539.151	05:08:27	-68:48:42.7	15.775 ± 0.049	16.605 ± 0.025	16.590 ± 0.060	16.508 ± 0.045	16.764 ± 0.032	16.786 ± 0.058	16.563 ± 0.047	16.49 ± 0.02	16.39 ± 0.04	16.09 ± 0.07	15.598 ± 0.040	15.403 ± 0.058	15.109 ± 0.165	…
1.4539.228	05:08:11	-68:48:38.6	16.067 ± 0.050	16.990 ± 0.031	16.988 ± 0.061	16.899 ± 0.057	16.990 ± 0.026	17.035 ± 0.024	16.906 ± 0.032	16.81 ± 0.02	16.63 ± 0.05	16.35 ± 0.08	15.845 ± 0.042	15.615 ± 0.047	…	…
2.4661.3757	05:09:08	-68:44:36.6	16.612 ± 0.068	17.462 ± 0.040	17.239 ± 0.035	17.103 ± 0.045	17.521 ± 0.015	17.423 ± 0.015	17.068 ± 0.021	16.89 ± 0.03	16.73 ± 0.03	16.36 ± 0.09	16.008 ± 0.078	15.767 ± 0.053	…	…
1.4539.185	05:08:07	-68:47:54.4	16.441 ± 0.176	16.493 ± 0.056	16.529 ± 0.058	16.646 ± 0.044	16.987 ± 0.103	16.965 ± 0.046	17.068 ± 0.099	16.81 ± 0.04	16.88 ± 0.07	16.65 ± 0.12	16.577 ± 0.113	16.501 ± 0.114	…	…
1.4539.134	05:08:15	-68:47:04.3	16.066 ± 0.053	16.263 ± 0.044	16.237 ± 0.037	16.047 ± 0.056	16.592 ± 0.027	16.593 ± 0.018	16.560 ± 0.078	16.33 ± 0.04	16.20 ± 0.05	16.25 ± 0.10	15.270 ± 0.067	15.533 ± 0.124	…	…
1.4540.778	05:08:41	-68:43:42.9	16.985 ± 0.058	17.719 ± 0.067	17.651 ± 0.067	17.404 ± 0.065	17.656 ± 0.026	17.654 ± 0.021	17.483 ± 0.034	17.53 ± 0.05	17.40 ± 0.09	17.26 ± 0.18	…	16.073 ± 0.132	…	…
1.4540.168	05:08:19	-68:43:41.8	15.179 ± 0.053	15.646 ± 0.053	15.704 ± 0.051	16.026 ± 0.051	17.263 ± 0.059	17.369 ± 0.037	17.430 ± 0.046	17.71 ± 0.05	17.84 ± 0.15	17.62 ± 0.25	…	15.420 ± 0.142	…	…
1.4660.2117	05:09:04	-68:46:26.4	16.723 ± 0.055	17.210 ± 0.032	17.108 ± 0.039	17.225 ± 0.046	17.215 ± 0.018	17.246 ± 0.019	17.170 ± 0.019	17.18 ± 0.03	17.20 ± 0.05	16.93 ± 0.14	16.861 ± 0.100	16.947 ± 0.132	…	…
79.4659.3417	05:09:26	-68:50:05.2	15.417 ± 0.051	16.012 ± 0.038	15.337 ± 0.093	14.930 ± 0.045	16.098 ± 0.051	15.655 ± 0.064	14.966 ± 0.074	14.35 ± 0.02	14.03 ± 0.01	13.82 ± 0.02	13.518 ± 0.054	13.294 ± 0.030	13.178 ± 0.067	…
1.4661.1151	05:08:45	-68:44:46.7	16.252 ± 0.052	16.546 ± 0.032	16.574 ± 0.043	16.479 ± 0.048	16.677 ± 0.02	16.682 ± 0.015	16.563 ± 0.018	16.56 ± 0.02	16.53 ± 0.05	16.41 ± 0.10	15.933 ± 0.094	15.923 ± 0.121	…	…
79.4659.3525	05:09:23	-68:50:10.3	15.931 ± 0.354	16.548 ± 0.044	16.409 ± 0.061	16.621 ± 0.044	16.545 ± 0.014	16.611 ± 0.015	16.609 ± 0.019	16.78 ± 0.03	16.80 ± 0.03	16.62 ± 0.10	16.499 ± 0.135	…	…	…
WFI-1587	05:08:31	-68:42:40.42	15.815 ± 0.053	16.451 ± 0.360	16.389 ± 0.067	16.462 ± 0.049	…	…	…	16.52 ± 0.02	16.41 ± 0.03	16.24 ± 0.06	15.888 ± 0.062	15.804 ± 0.050	…	…
1.4540.35	05:08:43	-68:44:42.64	16.254 ± 0.053	16.818 ± 0.027	16.775 ± 0.048	16.916 ± 0.106	…	…	…	16.71 ± 0.02	16.66 ± 0.06	16.48 ± 0.11	16.038 ± 0.124	15.702 ± 0.074	…	…
1.4550.105	05:08:28	-68:45:03.37	15.905 ± 0.061	16.441 ± 0.041	16.434 ± 0.063	16.567 ± 0.056	…	…	…	16.63 ± 0.02	16.67 ± 0.05	16.64 ± 0.12	16.217 ± 0.049	15.968 ± 0.048		…
1.4539.354	05:08:31	-68:46:33.38	16.857 ± 0.053	17.373 ± 0.030	17.328 ± 0.051	17.374 ± 0.052	…	…	…	17.64 ± 0.04	17.46 ± 0.10	17.44 ± 0.25	17.020 ± 0.131	16.853 ± 0.109	…	…
1.4539.302	05:08:30	-68:46:35.44	16.566 ± 0.052	17.201 ± 0.068	17.209 ± 0.048	17.245 ± 0.045	…	…	…	17.27 ± 0.03	17.07 ± 0.07	16.85 ± 0.14	16.306 ± 0.082	16.083 ± 0.070	…	…
1.4539.350	05:08:26	-68:46:49.33	16.902 ± 0.057	17.310 ± 0.050	17.334 ± 0.046	17.480 ± 0.092	…	…	…	17.38 ± 0.03	17.38 ± 0.10	17.03 ± 0.17	16.730 ± 0.094	16.578 ± 0.097	…	…
WFI-1489	05:08:22	-68:43:11.48	16.188 ± 0.057	16.759 ± 0.057	16.779 ± 0.045	16.867 ± 0.058	…	…	…	17.07 ± 0.02	17.01 ± 0.04	16.84 ± 0.12	16.427 ± 0.097	16.626 ± 0.137	…	…
WFI-1756	05:08:22	-68:43:05.25	15.959 ± 0.052	16.382 ± 0.036	16.377 ± 0.034	16.449 ± 0.077	16.494 ± 0.013	16.551 ± 0.011	16.460 ± 0.014	16.55 ± 0.02	16.56 ± 0.03	16.39 ± 0.07	15.970 ± 0.062	15.805 ± 0.056	…	…
1.4418.60	05:07:46	-68:48:30.67	14.334 ± 0.050	17.358 ± 0.059	15.873 ± 0.029	…	15.950 ± 0.04	15.983 ± 0.048	15.897 ± 0.032	15.92 ± 0.02	15.92 ± 0.02	15.74 ± 0.05	15.471 ± 0.037	15.263 ± 0.045	15.029 ± 0.093	
1.4539.191	05:08:03	-68:49:13.96	15.648 ± 0.088	16.244 ± 0.046	16.191 ± 0.056	16.300 ± 0.042	…	…	…	16.51 ± 0.02	16.31 ± 0.04	16.05 ± 0.07	15.578 ± 0.122	15.295 ± 0.061	15.088 ± 0.132	…
2.4661.3655	05:09:13	-68:41:43.46	15.565 ± 0.051	16.505 ± 0.030	16.316 ± 0.034	16.182 ± 0.046	…	…	…	16.10 ± 0.03	15.94 ± 0.04	15.82 ± 0.07	15.171 ± 0.080	14.951 ± 0.103	14.252 ± 0.146	…
1.4660.122	05:08:45	-68:46:28.7	16.297 ± 0.055	16.589 ± 0.061	16.397 ± 0.076	16.447 ± 0.085	16.818 ± 0.034	16.831 ± 0.028	16.576 ± 0.030	16.27 ± 0.03	16.11 ± 0.04	15.91 ± 0.07	14.622 ± 0.126	…	14.311 ± 0.097	…
1.4539.345	05:08:42	-68:46:02.7	16.872 ± 0.070	16.592 ± 0.106	16.762 ± 0.060	16.551 ± 0.100	17.216 ± 0.065	17.271 ± 0.022	17.230 ± 0.035	17.25 ± 0.04	17.33 ± 0.11	16.98 ± 0.16	16.440 ± 0.142	16.289 ± 0.137	…	…
1.4540.58	05:08:22	-68:45:26.901	15.304 ± 0.118	15.645 ± 0.021	15.670 ± 0.028	15.724 ± 0.041	15.782 ± 0.025	15.847 ± 0.021	15.788 ± 0.023	15.62 ± 0.02	15.43 ± 0.02	15.17 ± 0.04	14.619 ± 0.042	14.426 ± 0.037	14.073 ± 0.081	13.981 ± 0.214
1.4540.90	05:08:16	-68:43:51.452	15.370 ± 0.060	16.056 ± 0.025	15.987 ± 0.042	15.791 ± 0.04	…	…	…	15.97 ± 0.01	15.85 ± 0.03	15.68 ± 0.05	15.227 ± 0.048	15.054 ± 0.035	14.884 ± 0.139	13.961 ± 0.126
1	05:08:54	-68:48:49.96	17.228 ± 0.094	17.675 ± 0.087	17.481 ± 0.052	17.722 ± 0.054	…	…	…	17.88 ± 0.04	17.86 ± 0.08		17.372 ± 0.189	16.84 ± 0.113	…	…
79.4659.3425	05:09:27	-68:49:45.20	14.489 ± 0.053	15.379 ± 0.048	15.243 ± 0.054	15.502 ± 0.062	15.347 ± 0.061	15.475 ± 0.051	15.496 ± 0.040	15.50 ± 0.02	15.45 ± 0.02	15.24 ± 0.03	14.842 ± 0.043	14.699 ± 0.042	14.461 ± 0.082	13.798 ± 0.199
1.4538.126	05:08:22	-68:49:57.45	15.923 ± 0.064	16.939 ± 0.043	16.745 ± 0.036	16.593 ± 0.064	16.970 ± 0.027	16.940 ± 0.025	16.706 ± 0.027	16.48 ± 0.02	16.37 ± 0.03	16.07 ± 0.06	15.489 ± 0.051	15.218 ± 0.044	14.927 ± 0.135	…
1.4540.426	05:08:31	-68:43:37.31	17.357 ± 0.059	17.477 ± 0.078	17.603 ± 0.069	17.476 ± 0.121	20.166 ± 0.439	19.679 ± 0.263	19.698 ± 0.398	18.94 ± 0.11	…	…	14.496 ± 0.048	13.335 ± 0.031	12.128 ± 0.058	10.510 ± 0.030
1.4660.719	05:08:59	-68:46:22.3	…	20.846 ± 0.126	19.654 ± 0.125	17.978 ± 0.076	…	…	…	17.28 ± 0.05	16.73 ± 0.05	16.52 ± 0.10	…	…	…	…
1.4417.219	05:07:17	-68:50:12.320	16.716 ± 0.089	17.295 ± 0.046	17.200 ± 0.054	17.236 ± 0.096	…	…	…	17.32 ± 0.04	17.23 ± 0.07	16.97 ± 0.11	16.527 ± 0.091	16.175 ± 0.085	…	…
1.4417.105	05:07:44	-68:50:48.232	16.003 ± 0.055	16.512 ± 0.032	16.408 ± 0.037	16.626 ± 0.049	…	…	…	16.59 ± 0.02	16.56 ± 0.04	16.55 ± 0.09	16.208 ± 0.074	16.109 ± 0.072	…	…
1.4418.87	05:07:23	-68:47:39.063	15.695 ± 0.057	16.073 ± 0.054	16.024 ± 0.033	16.139 ± 0.041	…	…	…	16.27 ± 0.02	16.22 ± 0.03	16.22 ± 0.06	15.862 ± 0.063	15.78 ± 0.073	…	…
1.4418.102	05:07:39	-68:47:45.643	15.932 ± 0.054	16.440 ± 0.169	16.363 ± 0.038	16.375 ± 0.061	16.474 ± 0.029	16.511 ± 0.03	16.405 ± 0.034	16.37 ± 0.02	16.32 ± 0.03	16.22 ± 0.05	15.584 ± 0.191	15.626 ± 0.087	15.492 ± 0.176	…
1.4418.59	05:07:22	-68:47:59.004	15.050 ± 0.049	15.658 ± 0.027	15.787 ± 0.053	15.797 ± 0.037	15.894 ± 0.053	15.973 ± 0.036	15.913 ± 0.05	15.77 ± 0.01	15.57 ± 0.02	15.28 ± 0.03	14.584 ± 0.057	14.411 ± 0.065	14.065 ± 0.072	13.892 ± 0.178
79.4659.3412	05:09:25	-68:51:15.7	14.204 ± 0.051	15.324 ± 0.033	15.052 ± 0.035	14.936 ± 0.042	15.375 ± 0.04	15.335 ± 0.035	15.037 ± 0.032	14.93 ± 0.02	14.82 ± 0.02	14.51 ± 0.02	13.894 ± 0.036	13.631 ± 0.033	13.444 ± 0.058	13.189 ± 0.11
1.4537.174	05:08:38	-68:54:50.8	16.743 ± 0.096	16.907 ± 0.033	16.942 ± 0.035	17.119 ± 0.048	16.921 ± 0.049	16.984 ± 0.051	16.985 ± 0.046	17.05 ± 0.02	17.07 ± 0.06	17.18 ± 0.16	16.972 ± 0.088	17.042 ± 0.155	…	…
1.4539.149	05:08:31	-68:48:36.6	16.081 ± 0.051	16.357 ± 0.038	16.400 ± 0.040	16.511 ± 0.055	16.572 ± 0.014	16.622 ± 0.022	16.587 ± 0.020	16.66 ± 0.02	16.65 ± 0.04	16.49 ± 0.10	15.471 ± 0.097	15.475 ± 0.068	…	…
1.4550.68	05:08:31	-68:45:16.0	18.475 ± 0.105	17.930 ± 0.089	16.963 ± 0.047	…	18.581 ± 0.121	18.950 ± 0.233	18.721 ± 0.324	14.35 ± 0.01	13.55 ± 0.01	13.34 ± 0.01	13.153 ± 0.037	13.227 ± 0.026	13.247 ± 0.054	13.215 ± 0.081
79.4659.3485	05:09:18	-68:49:56.0	18.861 ± 0.130	18.490 ± 0.059	16.964 ± 0.053	15.681 ± 0.042	18.962 ± 0.071	17.265 ± 0.021	15.752 ± 0.013	14.54 ± 0.02	13.79 ± 0.02	13.56 ± 0.02	13.423 ± 0.027	13.495 ± 0.028	13.446 ± 0.080	…
1.4539.197	05:08:40	-68:46:53.7	16.520 ± 0.053	16.887 ± 0.042	16.798 ± 0.049	16.840 ± 0.050	16.888 ± 0.014	16.878 ± 0.016	16.783 ± 0.017	16.72 ± 0.02	16.61 ± 0.05	16.65 ± 0.11	16.487 ± 0.072	16.180 ± 0.045	…	…
1.4539.399	05:08:41	-68:46:17.1	17.112 ± 0.097	17.148 ± 0.078	17.385 ± 0.062	17.610 ± 0.050	17.525 ± 0.031	17.571 ± 0.04	17.565 ± 0.043	17.51 ± 0.04	17.41 ± 0.12	17.50 ± 0.25	16.761 ± 0.112	16.687 ± 0.131	…	…
2.4660.6602	05:09:01	-68:46:51.1	17.498 ± 0.058	17.699 ± 0.056	17.661 ± 0.069	17.802 ± 0.163	17.806 ± 0.021	17.832 ± 0.024	17.761 ± 0.028	17.76 ± 0.03	17.82 ± 0.07	17.48 ± 0.22	16.863 ± 0.112	16.594 ± 0.111	…	…
2.4660.6678	05:08:55	-68:46:29.3	17.009 ± 0.064	17.103 ± 0.060	17.237 ± 0.064	17.410 ± 0.076	17.424 ± 0.018	17.446 ± 0.018	17.352 ± 0.021	17.41 ± 0.03	17.34 ± 0.05	17.23 ± 0.18	14.996 ± 0.051	15.067 ± 0.062	14.945 ± 0.121	…
2.4660.6379	05:09:15	-68:46:08.6	15.981 ± 0.051	16.477 ± 0.029	16.362 ± 0.033	16.490 ± 0.082	16.542 ± 0.023	16.566 ± 0.015	16.484 ± 0.014	16.43 ± 0.02	16.42 ± 0.02	16.29 ± 0.08	16.100 ± 0.048	15.831 ± 0.047	…	…
2.4661.3816	05:09:02	-68:45:20.0	16.969 ± 0.132	17.494 ± 0.055	17.460 ± 0.060	17.283 ± 0.058	17.776 ± 0.019	17.711 ± 0.03	17.413 ± 0.028	17.22 ± 0.03	17.07 ± 0.03	16.70 ± 0.10	16.068 ± 0.081	15.685 ± 0.066	…	…

Table 2.3: –continued

MACHO or WFI ID	RA J2000 (h m s)	DEC J2000 (o ' ")	U MCPS (mag)	B MCPS (mag)	V MCPS (mag)	I MCPS (mag)	B OGLE (mag)	V OGLE (mag)	I OGLE (mag)	J IRSF (mag)	H IRSF (mag)	K IRSF (mag)	[3.6] SAGE (mag)	[4.5] SAGE (mag)	[5.8] SAGE (mag)	[8.0] SAGE (mag)
2.4661.3843	05:09:11	-68:44:51.2	17.235 ± 0.056	17.657 ± 0.449	17.539 ± 0.095	17.635 ± 0.084	17.657 ± 0.017	17.629 ± 0.018	17.563 ± 0.025	17.57 ± 0.03	17.66 ± 0.06	17.53 ± 0.24	…	16.767 ± 0.159	…	…
2.4782.2161	05:09:35	-68:45:01.3	16.106 ± 0.054	16.447 ± 0.366	16.400 ± 0.034	16.527 ± 0.042	16.643 ± 0.068	16.663 ± 0.065	16.587 ± 0.051	16.43 ± 0.02	16.27 ± 0.02	16.12 ± 0.07	15.565 ± 0.075	15.360 ± 0.068	…	…
1.4539.152	05:08:37	-68:45:53.258	16.091 ± 0.060	16.221 ± 0.053	16.216 ± 0.075	16.248 ± 0.102	17.154 ± 0.106	17.297 ± 0.173	17.447 ± 0.217	16.81 ± 0.05	16.9 ± 0.08	16.72 ± 0.11	16.028 ± 0.060	15.903 ± 0.088	…	…
1.4539.157	05:08:40	-68:46:06.568	16.357 ± 0.072	16.165 ± 0.072	16.340 ± 0.048	16.041 ± 0.088	…	…	…	16.57 ± 0.03	16.48 ± 0.04	16.43 ± 0.10	15.413 ± 0.085	15.403 ± 0.098	…	…
1.4539.184	05:08:39	-68:46:06.004	16.319 ± 0.063	16.313 ± 0.069	16.360 ± 0.066	17.837 ± 0.14	18.673 ± 0.155	18.612 ± 0.184	18.908 ± 0.207	16.81 ± 0.03	16.84 ± 0.06	16.98 ± 0.16	16.058 ± 0.110	16.232 ± 0.168	…	…
14	05:08:40	-68:46:17.025	17.094 ± 0.063	16.957 ± 0.168	17.251 ± 0.04	17.302 ± 0.063	17.471 ± 0.015	17.496 ± 0.03	17.454 ± 0.028	17.60 ± 0.03	17.64 ± 0.10	17.29 ± 0.24	…	…	…	…
1.4660.191	05:08:45	-68:46:34.426	16.647 ± 0.055	16.951 ± 0.044	16.744 ± 0.057	16.902 ± 0.061	17.333 ± 0.042	17.296 ± 0.113	17.183 ± 0.04	17.06 ± 0.04	16.93 ± 0.06	16.91 ± 0.14	…	…	…	…
2.4661.4355	05:08:58	-68:43:25.948	…	19.817 ± 0.105	19.840 ± 0.117	…	20.067 ± 0.112	20.056 ± 0.09	19.466 ± 0.127	18.71 ± 0.11	18.72 ± 0.14	…	…	…	…	…
2.4661.3880	05:08:59	-68:43:43.511	19.776 ± 0.184	19.451 ± 0.081	18.262 ± 0.079	17.114 ± 0.044	19.672 ± 0.067	18.516 ± 0.032	17.235 ± 0.019	16.23 ± 0.02	15.59 ± 0.02	15.46 ± 0.04	15.194 ± 0.106	15.196 ± 0.156	…	…
1.4661.117	05:08:46	-68:43:52.504	16.117 ± 0.056	16.477 ± 0.029	16.419 ± 0.04	16.545 ± 0.054	16.499 ± 0.008	16.506 ± 0.011	16.454 ± 0.013	16.48 ± 0.03	16.44 ± 0.03	16.35 ± 0.08	16.079 ± 0.118	15.984 ± 0.084	…	…
1.4661.204	05:08:46	-68:45:10.286	16.11 ± 0.106	15.462 ± 0.257	16.226 ± 0.089	16.213 ± 0.108	17.737 ± 0.159	17.612 ± 0.238	17.466 ± 0.198	17.10 ± 0.07	16.99 ± 0.12	16.92 ± 0.21	…		…	…
21	05:08:47	-68:45:11.242	15.925 ± 0.089	16.462 ± 0.114	16.514 ± 0.048	16.309 ± 0.114	16.831 ± 0.018	16.808 ± 0.042	16.722 ± 0.037	16.71 ± 0.02	16.71 ± 0.06	16.54 ± 0.10	16.444 ± 0.123	16.166 ± 0.115	…	…
1.4660.632	05:08:46	-68:46:24.486	…	17.463 ± 0.034	17.405 ± 0.042	17.291 ± 0.029	17.463 ± 0.034	17.405 ± 0.042	17.291 ± 0.029	…	…	…	…	…	…	…
1.4539.93	05:08:23	-68:45:57.774	15.492 ± 0.053	15.870 ± 0.028	15.846 ± 0.03	15.999 ± 0.043	15.992 ± 0.02	16.039 ± 0.012	16.023 ± 0.013	16.06 ± 0.02	16.06 ± 0.03	15.94 ± 0.06	15.780 ± 0.089	15.751 ± 0.090	…	…
1.4539.386	05:08:42	-68:48:04.859	17.18 ± 0.107	17.452 ± 0.052	17.266 ± 0.06	17.392 ± 0.05	17.782 ± 0.089	17.644 ± 0.047	17.560 ± 0.043	17.50 ± 0.04	17.41 ± 0.10	17.05 ± 0.15	17.035 ± 0.201	16.734 ± 0.160	…	…
1.4539.80	05:08:09	-68:46:56.1	…	18.475 ± 0.066	16.775 ± 0.041	15.119 ± 0.039	18.538 ± 0.021	16.869 ± 0.016	15.160 ± 0.010	13.96 ± 0.01	13.17 ± 0.01	12.96 ± 0.01	12.821 ± 0.024	12.957 ± 0.022	12.850 ± 0.046	12.962 ± 0.076

Chapter 3

OGLE 05155332−6925581: An eclipsing LMC member of the enigmatic group of DPVs

3.1 Introduction

The star OGLE 05155332−6925581 (MACHO IDs 79.5739.5807 and 78.5739.78; OGLE LMC-SC8-125836) is a member of the LMC DPV group. OGLE 05155332−6925581 shows a long-term periodicity of 188 days and an eclipsing variability with orbital period 7.2843 days (Mennickent et al. 2003). OGLE 05155332−6925581 appears in the field as a visual double, with a nearby companion 3.8 arcsec to the east. The OGLE position for the companion is $\alpha\,(2000) = 5^{\rm h}\ 15^{\rm m}\ 53.88^{\rm s}$ and $\delta\,(2000) = -69^{\circ}\ 25'\ 58.1''$. A finding chart based on an OGLE image taken at the $I-$band is shown in Fig. 3.1.

We have selected OGLE 05155332−6925581 for a detailed monitoring study since it is one of the brightest DPVs in the Large Magellanic Cloud (LMC). In consequence the quality of the available photometry is good enough for deriving physical properties of this object.

The system was analyzed for the first time by Mennickent et al. (2008, hereafter M08). The investigation carried out by M08 was based on a multi-wavelength light curve analysis, and resulted in discovering an intermediate-mass semidetached Algol-type binary in a evolutionary stage characterized by mass exchange and mass loss where the less massive star transfers matter onto the more massive star. M08 also detected evidence for a relatively luminous disc around the primary star. They reported a loop in the color-magnitude diagram during the long cycle that was interpreted as evidence of mass loss modulated by some still unknown mechanism. This was also supported by the motion of discrete absorption components observed in the infrared hydrogen lines.

So, M08 offered the explanation of cyclic mass loss for the long photometric cycle, but failed in identifying the motion of the gainer in their low resolution spectra, and the stellar parameters, in particular the mass ratio, remained relatively uncertain in their study.

Consequently, we decided to investigate this system with high resolution spectroscopy, in order to look for the missing features of the hot star, find definitive stellar parameters and understand better the evolutionary stage of the system when comparing with results of non-conservative evolutionary models for binary stars.

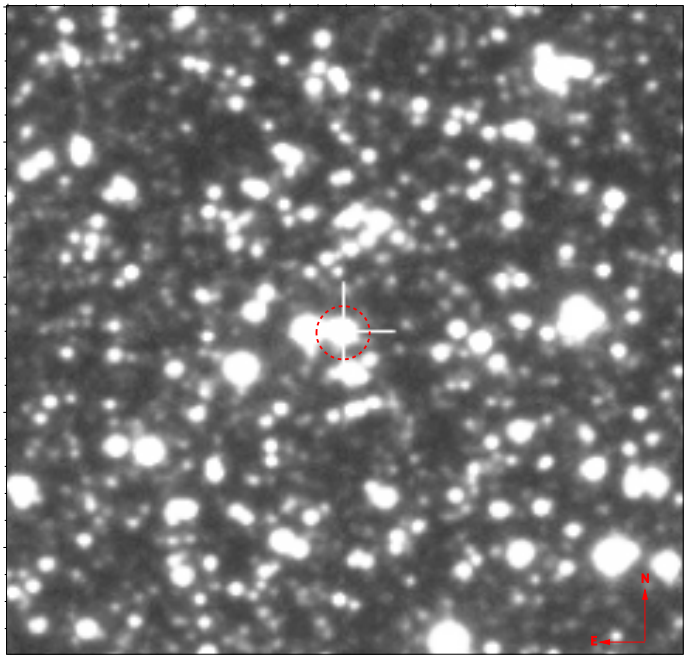

Figure 3.1: The finding chart of OGLE 05155332−6925581 based on an $I-$band OGLE image. The field of view is 60×60 arsec^2 and centred at $\alpha\,(2000) = 5^{\rm h}\ 15^{\rm m}\ 53.32^{\rm s}$ and $\delta\,(2000) = -69^{\circ}\ 25'\ 58.1''$. The red dashed circle indicates the position of OGLE 05155332−6925581

Mode	Setting	$\lambda-$range (Å)	Exp. Time (s)	R	N.
Medusa	HR5A	4341-4585	2770	20000	14
UVES	580	4775-6800	2770	47000	5

Table 3.1: Summary of the wavelength coverage, exposure time and spectral resolution of the different FLAMES modes and settings used in the observation of OGLE 05155332-6925581. R is the spectral resolving power and N the number of spectra obtained.

3.2 Observations and data reduction

We have monitored OGLE 05155332−6925581 spectroscopically in the optical wavelength range. The observations of this object were obtained in the period from 2009 January 17 to September 26, using the Fibre Large Array Multi-Element Spectrograph (FLAMES) on the Very large Telescope (VLT) in service mode. In total, 19 spectra were obtained, 14 of them with the GIRAFFE spectrograph using the standard MEDUSA-GIRAFFE setting High Resolution Mode (HR5A) in the wavelength region of 4 341 – 4 585 Å and five spectra using the Ultraviolet and Visual Echelle Spectrograph (UVES) in the region 4 775 – 6 800 Å with standard UVES setting 580, as shown in Table 5.1. The UVES data do not include the region 5 756 – 5 823 Å because of the gap between the two detectors.

The European Southern Observatory (ESO) Common Pipeline Library (CPL) FLAMES reduction routines were used for initial data processing and consisted of flat-fielding, bias subtraction and wavelength calibration. Separate fibers were used to observe the sky in each exposure. Each sky fibre was inspected for signs of cross-contamination from bright spectra/emission lines from adjacent fibers on the detector. Any contaminated sky fiber was rejected before creating a median sky spectrum, which was then subtracted from each science

Table 3.2: Principal lines detected in the optical spectrum of OGLE 05155332−6925581.

λ (Å)	Line	λ (Å)	Line	λ (Å)	Line
4 387.9	He I	4 471.5[a]	He I	4 390.6	Mg II
4 481.2[a]	Mg II	4 549.5 [a]	Fe II	4 861.3	Hβ
4 921.9[a]	He I	5 015.7	He I	5 875.6	He I
5 889.9	Na I int.	5 895.2	Na I int.	6 562.8	Hα
6 678.2	He I				

[a] Lines used in the RV measurement.

image. Related to the sky subtraction, one of the principal limitations of fiber spectroscopy is the subtraction of local nebular emission. Due to the distance of the Magellanic Clouds, even long-slit spectroscopy can suffer difficulties from spatially-varying nebular emission Walborn et al. (2002). Because we selected Balmer and He I lines for our analysis, we examined these lines for residuals due to poor nebulosity subtraction. These were actually found near the Hα profile, as shown later, but the affected regions are easily identified and isolated, and not considered in our analysis. The above method was implemented by Evans et al. (2011) to reduce VLT-FLAMES observations.

The UVES frames are reduced using a similar method as for the GIRAFFE data. We removed cosmic rays and then extracted the spectra, that were normalized over the entire spectral region. All spectra discussed in this part of PhD thesis are corrected to the heliocentric frame, using the RVCORRECT and DOPCOR packages implemented in IRAF.

3.3 Analysis and results

3.3.1 Radial velocity measurements and spectroscopic mass-ratio

M08 could not estimate a spectroscopic mass ratio for this system, mainly due to the weakness of the features of the primary star in the available low-resolution spectra. In addition, the analysis of the OGLE-II and MACHO light curves provided inconsistent values for the photometric mass ratio, in part since the light-curve model at that time did not include a contribution from a potential circumprimary disc. In this section we provide the first detection of the features of the hotter component and an improved determination for the the system mass ratio. Line identification was done with the aid of the spectral atlas for B main-sequence stars provided on-line by the Heidelberg University[1]. A list of the most prominent lines identified in each spectra is given in Table 3.2. We identified several strong absorption lines of He I, Mg II and Fe II in our FLAMES spectra. The UVES spectra display mainly Balmer and strong He I lines. Hα profiles are broad absorptions filled by emission. In this line we detected contributions of both stellar components plus a very narrow central absorption spike. This feature turned out to be residual absorption from the process of sky subtraction, consistent with spatially variable nebular emission in this part of the sky. The He I lines of the primary appear to be partially blended with lines from the secondary star, indicating a relatively hot donor star.

All spectra were normalized to the continuum before performing the radial velocity (RV) measurements and analysis. The RVs were measured by calculating the positions of the line center with a Gaussian fit using the IRAF SPLOT task. We measured the heliocentric radial velocities for the secondary using the Mg II 4 481Å and Fe II 4 549 Å lines. These RVs are listed in Table 3.3, along with the corresponding orbital phase computed with the ephemerides given in Section 3.3.2 and the errors taken as the standard deviations of the measurements. We

[1] http://www.lsw.uni-heidelberg.de/cgi-bin/websynspec.cgi

assumed a circular orbit, so a sine function was selected to fit them, obtaining a systemic velocity $\gamma_{\rm donor}$ = 253.20 ± 1.22 km s^{-1} and semi-amplitude $K_{\rm donor}$ = 200.42 ± 1.66 km s^{-1} with rms 4 km s^{-1} (see Fig. 3.2).
The lines He I 4471 Å and He I 4921 Å mainly follow the primary star, but a minor contribution of the secondary star is present. We used a deblending method to isolate the components in the analysis. We performed this task with the IRAF deblending 'd' routine available in the SPLOT package. We carefully measured the RVs of the He I lines (see Table 3.3) and fit them with a sine function, obtaining a systemic velocity $\gamma_{\rm gainer}$ = 229.85 ± 2.87 km s^{-1} and a semi-amplitude $K_{\rm gainer}$ = −41.69 ± 3.67 km s^{-1} with rms 11 km s^{-1}. Although there are other He I and Balmer lines in our UVES spectra with similar double profiles around phases 0.29 and 0.61, we could not deblend them to include them in the RV calculation, since the individual components were hardly resolved. The difference in the systemic velocity between the solution for the primary and secondary can be explained by emission of circumstellar matter affecting the He I lines. From the above semi-amplitudes we find a spectroscopic mass ratio of q_{sp} = 0.21 ± 0.02 for OGLE 05155332−6925581, which is smaller than q = 0.29 obtained by M08 from the best MACHO blue light-curve fitting model.
Interestingly, our donor half-amplitudes derived from the study of Fe II and Mg II lines are larger than those found by M08 in Balmer lines. This could be associated with larger contamination by emission in Balmer lines, as suggested by our donor-subtracted Hα profiles (Section 3.3.4). The fact that the emission formed around the gainer moves in anti-phase with the donor absorption produces the net effect of lowering the observed donor RV half-amplitudes. We considered another possible cause for the half-amplitude discrepancy: displacement of the light-centre due to donor irradiation by the disc and gainer (e.g. Wade & Horne 1988; Watson et al. 2003). This effect would result in an overestimate of K_2, leading to a corresponding underestimate of q. However, the absence of asymmetries in the donor line profiles and the large observed differences in H I line RV half-amplitudes (up to 45 km s^{-1}) suggest that residual emission is the most likely explanation. It is difficult to imagine how light centers could differ so much between lines of the same elements at a given ionization stage.

3.3.2 The light curve analysis and fitting procedure

We have used public domain photometric data available from the MACHO (Alcock et al. 1999) and OGLE II and III databases (Udalski et al. 1997; Szymanski 2005; Poleski et al. 2010). The photometric data cover 13.7 years. The observations were folded to the orbital period using the ephemeris for the main minimum from M08:

$$\mathrm{T_{min}} = 2\,450\,000.1392\,(21) + 7^{\rm d}.284297\,(10) \times \mathrm{E}. \tag{3.1}$$

The light-curve analysis was performed using the inverse-problem solving method (Djuraševic 1992) based on the simplex algorithm and the current version of the model of a binary system with a circumprimary disc (Djurašević et al. 2010). The model of a binary system with a circumprimary disc and code writing by Djurašević (1992), have been widely used and tested during our recent research of intermediate-mass interacting binaries (e.g. Djurašević et al. 2010, 2011, 2012; Mennickent et al. 2012a) and it is discussed in Appendix A.

3.3.3 Fitting procedure for photometric data

The fitting was done for a limited set of important parameters. The mass ratio $q = \mathcal{M}_c/\mathcal{M}_h$ = 0.21 was set to the value determined by the radial velocities of our new FLAMES observations, discussed in Section 3.3.1. The temperature for the primary was fixed to the value given by M08, viz. T_h = 25 000 K. Rotation for the donor was assumed synchronous (f_c = 1.0) since it is assumed that it has filled its Roche lobe (i.e. the filling factor of the donor was set to F_c = 1.0). In the case of the gainer, however, the accreted material from the disc is expected to transfer enough angular moment to increase the spin rate of the gainer up to the critical rotation

Table 3.3: RVs measured from the MEDUSA and UVES spectra for OGLE 05155332−6925581 referred to the Local Standard of Rest. The orbital phase Φ_o is calculated following the ephemeris given in Eq. (3.1). Subindex 1 and 2 refers to the gainer and donor, respectively.

HJD -2450000	Φ_o	RV_1 km s^{-1}	$(O-C)_1$ km s^{-1}	RV_2 km s^{-1}	$(O-C)_2$ km s^{-1}	Mode
5084.8895	0.043	228.82 ± 2.63	−12.32 ± 2.63	305.71 ± 1.18 [b]	−0.61 ± 1.18	Medusa
5100.8791	0.238	187.48 ± 1.68	−8.44 ± 1.68	455.29 ± 1.37	2.28 ± 1.37	Medusa
4853.6087	0.292	178.59 ± 0.79 [a]	−11.21 ± 0.79	...	...	UVES
4853.6538	0.298	187.94 ± 1.50	−1.45 ± 1.50	444.38 ± 0.75 [b]	−0.14 ± 0.75	Medusa
4868.6050	0.351	197.64 ± 0.46 [a]	9.30 ± 0.46	...	...	UVES
5079.8642	0.353	185.83 ± 0.94	−2.55 ± 0.94	407.31 ± 0.48 [b]	−5.67 ± 0.48	Medusa
4868.6495	0.357	183.77 ± 1.24	−4.73 ± 1.24	417.92 ± 1.50 [b]	8.04 ± 1.50	Medusa
4876.5457	0.441	215.14 ± 1.89 [a]	18.33 ± 1.89	...	...	UVES
4898.6029	0.469	207.32 ± 0.51 [a]	5.56 ± 0.51	...	...	UVES
5080.8272	0.485	215.98 ± 1.54	10.98 ± 1.54	265.49 ± 1.02 [b]	−6.14 ± 1.02	Medusa
4848.5946	0.604	228.10 ± 0.98	−6.29 ± 0.98	133.30 ± 0.34	2.69 ± 0.34	Medusa
4848.6366	0.610	245.81 ± 1.25 [a]	9.87 ± 1.25	...	...	UVES
5081.8340	0.623	223.96 ± 1.41	−15.33 ± 1.41	116.96 ± 0.72	4.48 ± 0.72	Medusa
4892.5550	0.639	233.16 ± 0.98	−10.16 ± 0.98	100.81 ± 1.21 [b]	2.06 ± 1.21	Medusa
4863.5947	0.663	238.02 ± 3.16	−11.07 ± 3.16	80.23 ± 1.33	−0.88 ± 1.33	Medusa
4907.5324	0.695	261.07 ± 1.81	4.98 ± 1.81	61.32 ± 0.16 [b]	−2.39 ± 0.16	Medusa
5082.8394	0.761	264.24 ± 1.80	−2.68 ± 1.80	56.16 ± 0.60 [b]	3.85 ± 0.60	Medusa
4865.5906	0.937	280.54 ± 2.76	17.01 ± 2.76	180.51 ± 0.88	5.29 ± 0.88	Medusa
5076.9004	0.946	272.10 ± 1.73	10.02 ± 1.73	180.56 ± 1.58 [b]	−5.26 ± 1.58	Medusa

[a] RVs values based on the line He II 4 921 Å,
[b] RVs values based on the lines Mg II 4 481 Å, only.

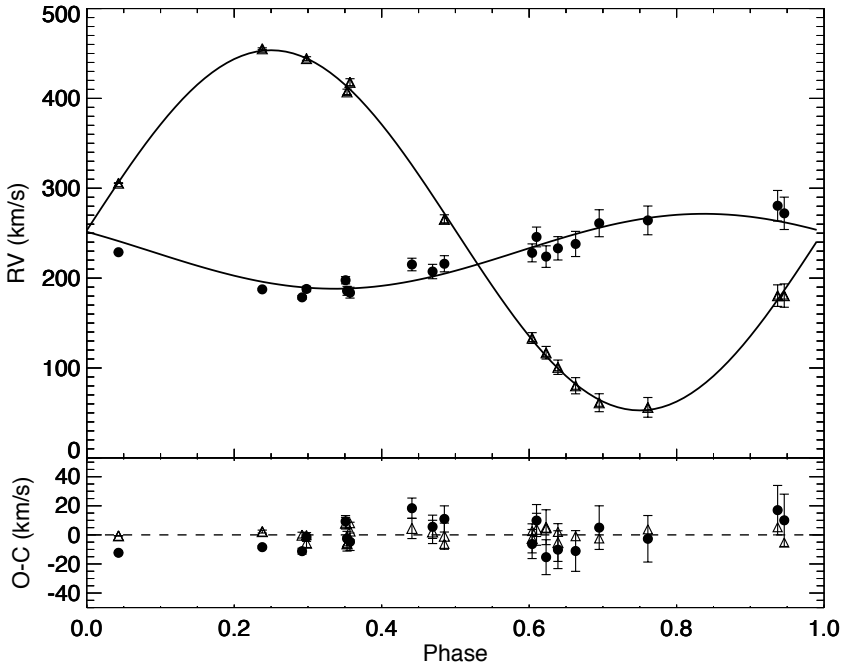

Figure 3.2: The RV curve together with O-C for OGLE 05155332−6925581. Plot is folded to orbital period using the ephemeris for the main minimum, given in the Eq. (3.1). Panel shows the RV measurements with the best-fit solutions. Filled circles represent the gainer and triangles the donor.

velocity as soon as even a small fraction of the mass has been transferred (de Mink et al. 2007). This means that the gainer should fill its corresponding non-synchronous Roche lobe for the star rotating in the critical regime. This assumption is justified by the rapid spin-up of the gainer at the system evolutionary stage (see Section 3.4). Therefore, the dimensions and the amount of rotational distortion are uniquely determined by the factor of non-synchronous rotation, which is the ratio between the actual and the Keplerian angular velocity. In this model the factor of non-synchronous rotation for the gainer was a free parameter, also determined by solving the inverse problem. However, we also calculated the best-fitting model for a synchronous gainer, and the results practically do not differ from the critical case. The results of our analysis are presented in Table 3.4.

The stellar parameters improve significantly the solution given by M08. We find primary and donor stars with 9.1 ± 0.5 and 1.9 ± 0.2 $M_\odot$, respectively. They have log g of 3.9 ± 0.1 and 2.8 ± 0.1 and radii of 5.6 ± 0.2 and 8.9 ± 0.3 $R_\odot$, respectively. The bolometric magnitudes are $M^h_{\rm bol} = -5.3$ and $M^c_{\rm bol} = -3.4$. The best fit requires an optically thick disc around the gainer. This disc has a moderately convex shape, with central thickness $d_c \approx 2.6\,R_\odot$ and thickness at the edge $d_e \approx 0.8\,R_\odot$. The radius of the disc is $\mathcal{R}_d \approx 14\,R_\odot$, more than two times larger than the gainer radius and about ∼ 77 per cent of the Roche lobe radius. The temperature of the disc increases from $T_d = 12\,600$ K at its edge to $T_h = 25\,000$ K in the inner radius, where it is in thermal and physical contact with the gainer.

The two spots on the edge of the disc mentioned in Appendix A were found at longitudes at 324° and 130° with temperatures 12 and 18 per cent higher than the disk edge temperature, respectively. Whereas the hot spot represents the region of impact of the gas stream with the disk, the bright spot at $\lambda \approx 130°$ can be interpreted as a region where the disc significantly deviates from circular shape, or as a region where the stream material falls back to the opposite side of the disc, after being deflected by the impact. Due to the relatively small size

Table 3.4: Result of the analysis of LMC star OGLE 05155332−6925581 in MACHO blue, MACHO red and OGLE I-band light curves obtained by solving the inverse problem for the Roche model with an accretion disc around the more-massive (gainer) component in critical rotation regime.

Quantity	MACHO blue	MACHO red	OGLE I	mean BRI	Quantity	
n	2 964	2 796	883		$\mathcal{M}_h[\mathcal{M}_\odot]$	9.1 ± 0.5
$\Sigma(O-C)^2$	1.9490	1.8550	0.2634		$\mathcal{M}_c[\mathcal{M}_\odot]$	1.9 ± 0.2
$\sigma_{\rm rms}$	0.0256	0.0258	0.0173		$\mathcal{R}_h[\mathrm{R}_\odot]$	5.6 ± 0.2
$i[^\circ]$	82.33	82.25	82.36	82.3 ± 0.3	$\mathcal{R}_c[\mathrm{R}_\odot]$	8.9 ± 0.3
$\mathrm{F_d}$	0.76	0.77	0.77	0.77 ± 0.03	$\log g_h$	3.9 ± 0.1
T_d[K]	12 200	12 800	12 770	12 600 ± 600	$\log g_c$	2.8 ± 0.1
$\mathrm{d_e}[a_{\rm orb}]$	0.020	0.021	0.025	0.02 ± 0.01	$M^{\rm h}_{\rm bol}$	−5.3 ± 0.2
$\mathrm{d_c}[a_{\rm orb}]$	0.070	0.072	0.077	0.07 ± 0.01	$M^{\rm c}_{\rm bol}$	−3.4 ± 0.1
$\mathrm{a_T}$	4.0	3.5	3.5	3.7 ± 0.3	$a_{\rm orb}[\mathrm{R}_\odot]$	35.2 ± 0.5
$\mathrm{f_h}$	10.6	10.6	10.5	10.6 ± 0.3	$\mathcal{R}_d[\mathrm{R}_\odot]$	14.1 ± 0.5
$\mathrm{F_h}$	1.00	1.00	1.00	1.00	$\mathrm{d_e}[\mathrm{R}_\odot]$	0.8 ± 0.3
$\mathrm{T_c}$[K]	12 930	12840	12 830	12 900 ± 500	$\mathrm{d_c}[\mathrm{R}_\odot]$	2.6 ± 0.5
$\mathrm{A_{hs}} = \mathrm{T_{hs}} / \mathrm{T}_d$	1.13	1.12	1.10	1.12 ± 0.1		
$\theta_{\rm hs}[^\circ]$	14.1	16.3	16.2	15.5 ± 1.0		
$\lambda_{\rm hs}[^\circ]$	327.4	322.9	322.4	324.2 ± 5.0		
$\theta_{\rm rad}[^\circ]$	-34.2	-33.8	-34.9	−34.3 ± 5.0		
$\mathrm{A_{bs}} = \mathrm{T_{bs}} / \mathrm{T}_d$	1.15	1.19	1.20	1.18 ± 0.1		
$\theta_{\rm bs}[^\circ]$	54.1	52.2	48.2	51.5 ± 3.0		
$\lambda_{\rm bs}[^\circ]$	120.5	136.5	134.2	130.4 ± 13.0		
$\Omega_{\rm h}$	7.94	7.92	7.90	7.92 ± 0.02		
$\Omega_{\rm c}$	2.56	2.56	2.56	2.56 ± 0.02		

FIXED PARAMETER: $q = \mathcal{M}_c/\mathcal{M}_h = 0.21$ - mass ratio of the components, $\mathrm{T_h} = 25\,000$ K - temperature of the more-massive (gainer), $\mathrm{F_c} = 1.0$ - filling factor for the critical Roche lobe of the donor, $\mathrm{F_h} = \mathrm{R}_h/\mathrm{R}_{zc} = 1.0$ -filing factor for the critical non-synchronous lobe of the more massive gainer (ratio of the stellar polar radius to the critical non-synchronous lobe radius along z-axis for a star in critical rotation regime), $f_c = 1.00$ -synchronous rotation coefficients of the donor, $\beta_{\rm h,c} = 0.25$ - gravity-darkening coefficients of the components, $\mathrm{A_{h,c}} = 1.0$ - albedo coefficients of the components.
Note: n - total number of observations in MACHO blue (B), red (R) and OGLE I-band; $\Sigma(O-C)^2$ - final sum of square of residual between observed (LCO) and synthetic (LCC) light-curves, $\sigma_{\rm rms}$ - root-mean-square of the residuals, i - orbit inclination (in arc degrees), $\mathrm{F_d} = \mathrm{R_d}/\mathrm{R_{yc}}$ - disc dimension factor (the ratio of the disc radius to the critical Roche lobe radius along y-axis), $\mathrm{T_d}$ - disc-edge temperature , $\mathrm{d_e}$, $\mathrm{d_c}$ - disc thicknesses (at the edge and at the center of the disc, respectively) in the units of the distance between the components, $\mathrm{a_T}$ -disc temperature distribution coefficient, $\mathrm{f_h}$ - non-synchronous rotation coefficient of the more massive gainer (in the critical rotation regime), $\mathrm{T_c}$ -temperature of the less massive cooler donor, $\Omega_{\rm h,c}$ - dimensionless surface potentials of the hotter gainer and cooler donor, $\mathcal{M}_{h,c}[\mathcal{M}_\odot]$, $\mathcal{R}_{h,c}[\mathrm{R}_\odot]$ - stellar masses and mean radii of star in solar units, $\log g_{h,c}$ - logarithm (base 10) of the system components effective gravity, $M^{\rm h,c}_{\rm bol}$ - absolute stellar bolometric magnitudes, $a_{\rm orb}[\mathrm{R}_\odot]$, $\mathcal{R}_d[\mathrm{R}_\odot]$, $\mathrm{d_e}[\mathrm{R}_\odot]$, $\mathrm{d_c}[\mathrm{R}_\odot]$ - orbital semi-major axis, disc radius and disc thicknesses at its edge and center, respectively, given in solar units.

and temperature difference compared to the lateral side of the disc, the hotspot is not sufficient to irradiate the face of the donor significantly. The bright spot is located on the disc lateral side which is not able to contribute to the irradiation of the donor.

In Fig. 3.3 we show the comparison between the synthetic and the OGLE-I, MACHO-B and MACHO-R light curves. We do not include error bars since the scatter in the light curves probably gives a better representation of the true errors. In general the fit is pretty good, but there is a slightly larger scatter in $O - C$ around secondary eclipse (I-band) and main eclipse (b and r bands). This scatter is very minor and could represent a third light in the system that is not considered in the model and that it is best visible during eclipses. A probable explanation for these larger residuals is the 3D structure of the hot spot, including material located at high latitudes, whose small contribution to the total flux is detected only during eclipses. We also show the geometrical model of the system at quadratures. The residuals do not depend on the long-cycle phase. This important result indicates that the orbital solution including the disc remains constant during the whole long cycle. Therefore, the disc represented in the model is not the cause for the long cycle. The figure also illustrates the geometrically thin nature of the disc, its relative size and the positions of the hot and bright spots in the system. At quadratures, the disc contributes about 15 per cent to the total light of the system at the I-band, whereas at main eclipse the secondary contributes about 84 per cent.

3.3.4 Donor-subtracted and residual spectra

One of the goals of this chapter is to find information about the environment near the hot primary star. However, from the disentangling processes we know that our composite spectrum is contaminated by the light contribution of the B-type donor, in particular in the Balmer and He lines. Thus, we need to remove the secondary star's spectral contribution from the observed spectra to study the light contribution of the primary and its circumstellar gas.

In order to remove the donor light from the composite spectra we assume that its contribution to the total light is additive to the other light sources and represented by the light-curve model proposed in Section 3.3.2. Furthermore, we compute a synthetic spectrum using the data in Table 3.4 for the donor star.

The model for the donor stellar atmosphere was constructed for an effective temperature of 13 000 K and surface gravity of $\log g = 3.0$ with solar abundance, using the LTE ATLAS9 code (Kurucz 1993), which handles the line opacity with the opacity distribution functions method. The Kurucz's models are constructed with the assumptions of plane-parallel geometry and hydrostatic and radiative equilibrium of the gas. The synthetic spectrum was computed with the SYNTHE code (Kurucz 1993) and broadening at a rotational velocity of $V_{\rm rot} \sin i = 60$ km s^{-1}, assuming that the donor has synchronous rotation, as was mentioned in Section 3.3.3. Both codes, ATLAS9 and SYNTHE were ported under General Public License (GNU) Linux by Sbordone (2005) and are available online[2]. The atomic data were taken from Castelli & Hubrig (2004)[3].

After that, the synthetic spectrum was Doppler corrected and scaled according to the contribution of the donor star at a given orbital phase and at the given wavelength range. This method was used by Mennickent et al. (2012b, hereafter M12b) to remove the donor spectrum from the observed composite spectrum of the interacting binary V393 Sco. Then, the isolated gainer spectrum plus disc in units of its normalized flux is given by

$$f_{\rm G}(\lambda, \Phi_0, \Phi_l) = f(\lambda, \Phi_0, \Phi_l) - P(\Phi_0, \lambda_c) \times f_{\rm D}(\lambda, \Phi_0) \tag{3.2}$$

where $f_{\rm G}$ is the donor-subtracted flux, f the observed flux, $f_{\rm D}$ the synthetic donor spectrum, P the fractional

[2] wwwuser.oat.ts.astro.it/atmos/

[3] wwwuser.oat.ts.astro.it/castelli/grids.html

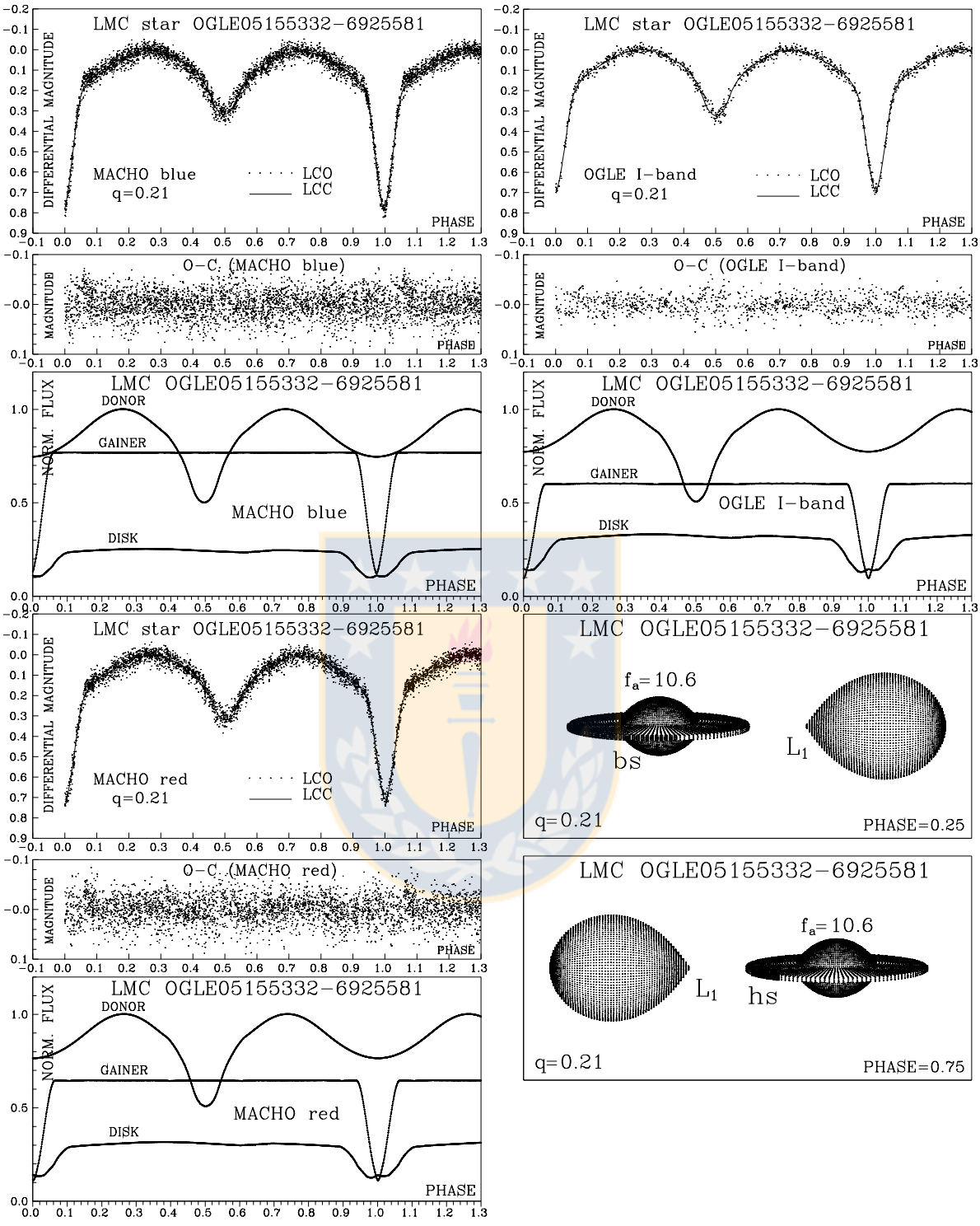

Figure 3.3: Observed (LCO) and synthetic (LCC) light-curves of LMC star OGLE 05155332−6925581 obtained by analyzing MACHO blue, red and OGLE I-band photometric observations; final O-C residuals between the observed and optimum synthetic light curves; fluxes of donor, gainer and of the accretion disc, normalized to the donor flux at phase 0.25; the views of the optimal model at orbital phases 0.25 and 0.75, obtained with parameters estimated by the light curve analysis.

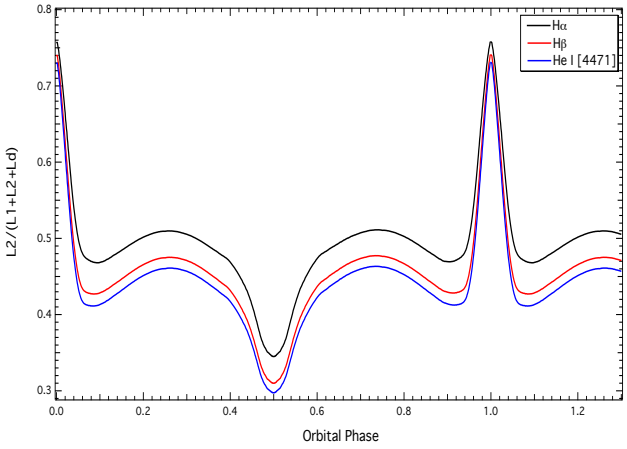

Figure 3.4: Light contribution factor for the donor at different spectral lines and orbital phases according to the light-curve model given in Section 3.3.2. L_1, L_2 and L_d are the gainer, donor and disc fluxes, respectively.

	FWHM (km s^{-1})		EW (10^{-2}Å)	
Phase	Hβ	He I [4921]	Hβ	He I [4921]
0.292	579.30 ± 3.60	335.80 ± 1.08	444 ± 1	73 ± 1
0.351	574.00 ± 1.19	338.10 ± 0.24	432 ± 1	63 ± 3
0.441	462.53 ± 1.05	301.73 ± 4.15	364 ± 1	54 ± 2
0.469	523.13 ± 1.90	247.00 ± 3.53	333 ± 1	40 ± 1
0.610	562.40 ± 0.65	233.30 ± 4.41	442 ± 1	58 ± 1

Table 3.5: Equivalent width and FWHM of the Hβ and He I 4 921 Å absorption lines from the donor-subtracted UVES spectra.

contribution of the donor derived from our light-curve model and λ_c the representative wavelength where P is calculated. The theoretical light contribution factors for the donor at different spectral lines according to the light-curve model are shown in Fig 3.4. The result of this process was a set of “donor-subtracted" spectra that were normalized to the new continuum.

Our spectra cover 1.5 times the long cycle of 172 days, but only the MEDUSA spectra are well distributed to adequately map the long variability. We inspected these profiles, having subtracted the donor, but without observing significant changes in the small wavelength range provided by the MEDUSA spectra. In the following, we analyse the UVES spectra, that show the prominent Hβ and He I 4 921 Å lines, looking for orbital variability.

The donor-subtracted spectra for the Hβ and He I 4 921 Å absorption lines in orbital phases 0.29 to 0.61 are shown in Fig. 3.5. The Hβ profiles are broad and show variable absorption wings extending up to ±1000 km s^{-1}. These lines are more symmetric near the secondary eclipse. The helium lines are broad and asymmetric and sometimes show flanking emission, especially at the red side of the He I 4 921 line in Fig. 3.5. Measures of full width at half-maximum (FWHM) and equivalent width (EW) for these lines are shown in Table 3.5 for each orbital phase. Fig. 3.5 also shows a synthetic spectrum computed with SYNTHE for the gainer using parameters $T_{\rm eff}$ = 25 000 K and $\log g$ = 3.9 and solar abundance. Our synthesized spectrum was computed for a gainer in critical rotation using a rotational parameter $V_{\rm rot} \sin i$ = 412 km s^{-1}, as determined in Section 3.3.3.

It is clear that the profiles are highly variable in shape. The fact that the Hβ line is deeper than the gainer synthetic profile suggests that it is produced in an extended absorption medium beyond the stellar photosphere, a kind of pseudo-photosphere. This medium could be the disc revealed in the light-curve analysis. The lack

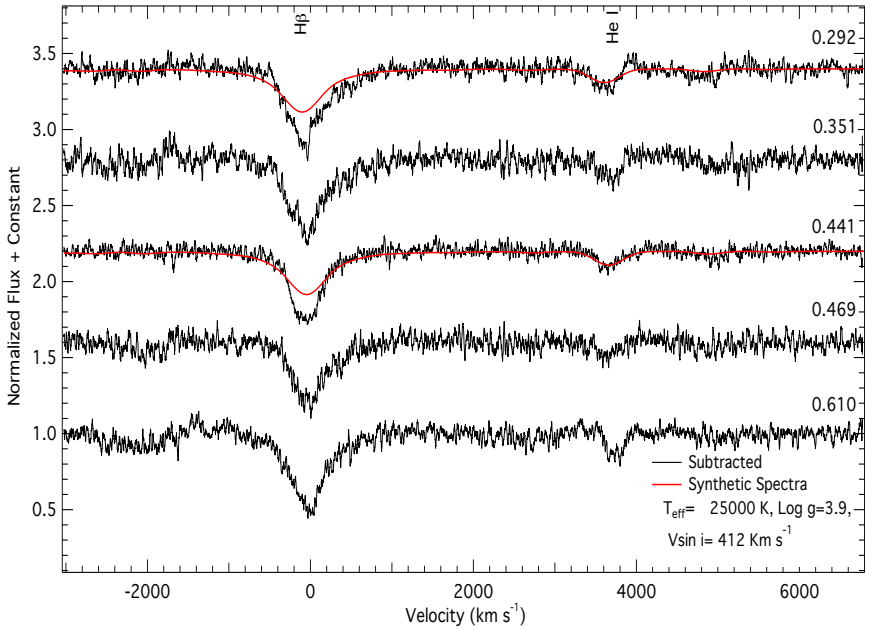

Figure 3.5: Donor-subtracted spectra showing Hβ variable extended wings up to $\pm$1000 km s^{-1}. He I 4 921 Å absorption line is also visible. The red line overplotted on the donor-subtracted spectra is the SYNTHE model using Kurucz atmospheres for a more-massive (gainer) component in the critical rotation regime. The labels in the upper right of each spectrum indicate the orbital phase.

of obvious variability in the 13.7-year folded orbital light curve indicates a stable disc, so the large profile variability suggests the presence of additional mass streams in the system. The general features are compatible with absorption/emission in an extended photosphere around the gainer plus additional mass flows. We found a good match using the critical rotational velocity for the He I profiles and Hβ absorption wings of our subtracted spectra near secondary eclipse, when the gainer is in front of the donor, as shown in Fig. 3.5. However, we observe a small deviation at phase 0.29, when the wings of the line profiles are less symmetrical, showing extended absorption in the Hβ red wing and emission in the He I 4 921Å red wing.

We obtained residual spectra around the Hα region. These spectra were obtained from the donor-subtracted spectra after removing the gainer synthetic spectrum. The process reveals weak double emission at Hα with a peak separation of about 620 kms^{-1} (Fig. 3.6). The same exercise at the He I 6 678 Å line shows absorption and traces of emission. We are cautious about interpreting the Hα double emission as produced in the circumprimary disc, since in the case of V 393 Scorpii the evidence indicates that this kind of profile is produced in a bipolar wind (M12b).

We conclude that line profile fitting cannot be used as proof of critical rotation in this system due to the high variability of the profiles. On the other hand, the detection of Balmer and He I emission is consistent with the presence of circumstellar matter in the system.

3.4 Discussion

3.4.1 On the evolutionary stage of OGLE 05155332−6925581

The comparison of the stellar parameters of OGLE 05155332−6925581 with predictions of evolutionary models for single stars of solar metallicity indicates that the gainer is located near the main-sequence band, a little

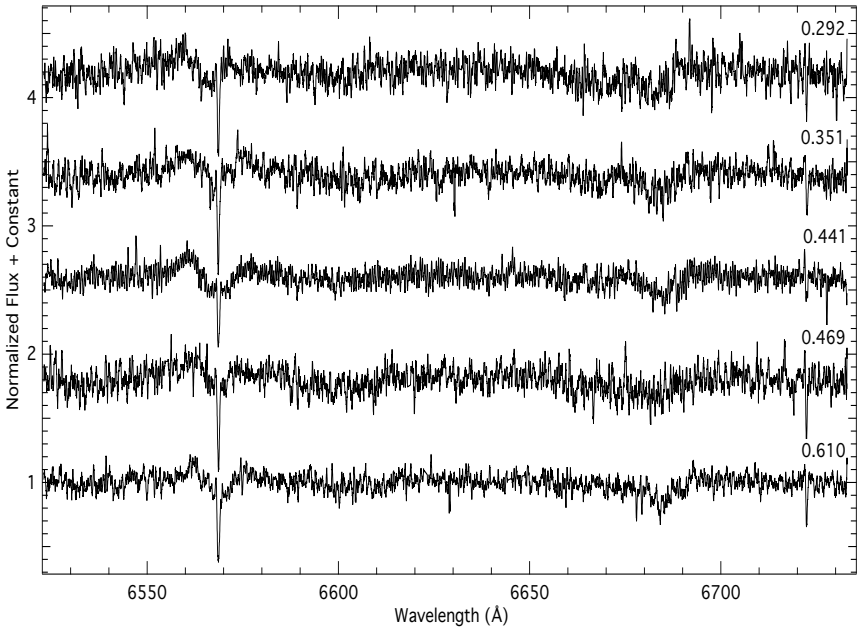

Figure 3.6: Residual spectra showing the Hα and He I 6 678 line profiles after removing donor and gainer synthetic spectra. The narrow absorption in Hα is an artifact of the reduction process. The labels in the upper right of each spectrum indicate the orbital phase.

displaced to higher luminosities for a star of comparable mass, while the donor is evolved from the main sequence, much more luminous for its mass, a fact explained by its expansion and subsequent filling of its Roche lobe (see Fig. 3.7). The small luminosity excess of the gainer can be explained in terms of their slightly advanced evolutionary stage; it has consumed about half of the hydrogen in its core, as will be shown later in this section.

In order to understand the evolutionary stage of this binary we compared our system parameters with those of the 561 conservative and non-conservative evolutionary tracks given by van Rensbergen et al. (2008b), available at the Center de Données Stellaires (CDS). Similarly to the case of V393 Sco studied by Mennickent et al. (2012a, hereafter M12a), a multi-parametric fit was carried out for each synthetic model (labeled with i) through the evaluation of the quantity $\chi^2_{i,j}$ defined by:

$$\chi^2_{i,j} \equiv \frac{1}{N}\sum_k \omega_k \left[\frac{S_{i,j,k} - O_k}{O_k}\right]^2 \tag{3.3}$$

where N is a normalization factor and ω_k the statistical weight of the parameter O_k, calculated as:

$$\omega_k = \sqrt{O_k/\epsilon\,(O_k)} \tag{3.4}$$

where $\epsilon\,(O_k)$ is the error associated with the observable O_k. $S_{i,j,k}$ is the theoretical parameter for the observable O_k, in the time t_j for the i-labeled model. For further information about the fitting procedure see M12a.

We find the absolute χ^2 minimum in the tidal-strong interacting model with initial masses of 8 and 3.2 $M_\odot$ and initial orbital period $P_{\mathrm{orb},i} = 2.5$ days. The absolute minimum χ^2_{min} identifies the current age of the system along with the theoretical stellar and orbital parameters, which are presented in Table 3.6.

The best fit indicates that OGLE 05155332−6925581 has an age of 4.76×10^7 years. The corresponding

Table 3.6: The parameters of the van Rensbergen et al. (2008b) model that best fit the OGLE 05155332−6925581 data. The hydrogen and helium core mass fractions (X_c and Y_c) are given for the cool and hot star.

Quantity	Value	Quantity	Value
Age	4.76×10^7 yr	Period	7.241 d
M_c	1.945 $M_\odot$	M_h	9.249 $M_\odot$
$\dot{M}_c$	$-3.17 \times 10^{-6}\ M_\odot\, yr^{-1}$	$\dot{M}_h$	$3.105 \times 10^{-6}\ M_\odot\, yr^{-1}$
$\log T_c$	4.120 K	$\log T_h$	4.385 K
$\log L_c$	3.351 $L_\odot$	$\log L_h$	3.862 $L_\odot$
R_c	9.090 $R_\odot$	R_h	4.821 $R_\odot$
X_{cc}	0.00	X_{ch}	0.496
Y_{cc}	0.98	Y_{ch}	0.484

evolutionary tracks for the primary and secondary stars are shown in Fig. 3.8, along with the position for the best model for our system.

We notice a good agreement with the evolutionary tracks given by the best model. The secondary star is inflated ($R_c = 9.1\, R_\odot$) and exchanges mass through the L_1 Lagrangian point at a rate of about $\dot{M} = 3.105 \times 10^{-6}\ M_\odot\, yr^{-1}$. This rather large mass transfer rate compares relatively well with the low limit found by M08, namely 8.6×10^{-5} $M_\odot$/yr, derived assuming accretion powered luminosity.

3.4.2 On mass flows and angular momentum loss

The orbital light curve was re-examined with the program Period04[4]. We calculated the error in the main frequency of the fit to the orbital light curve. The error consistently given by Monte Carlo simulations and the method of least squares is 2×10^{-7} Hz. This means that the period could drift at most by 2×10^{-5} d in 3365 d (the OGLE dataset time baseline). This implies that a period change at constant rate, if present, should be less than 0.2 s/yr to be consistent with the photometric time series. However, according to the best theoretical model, we find the system in a stage characterized by a rapid change of the orbital period (Fig. 3.8). The period should be changing by 4.7 s yr^{-1}. This apparent inconsistency was already noted by M08, who argued that the effects of mass exchange and mass loss could be balanced in the system producing a net effect of non-variability for the orbital period.

The models by van Rensbergen et al. (2008a, 2011) parametrize mass and angular momentum loss from the system through the parameters β and η, respectively. The mass loss is driven by radiation pressure from a hot spot located in the stream impact region on the stellar surface or accretion disc edge. The mass loss extracts angular momentum from the system and in this particular model only from the gainer. According to the models of van Rensbergen et al. (2008a, 2011), particular pairs of the parameters β and η should result in a constant orbital period.

The mass and angular momentum loss from a system during mass transfer can be described with the (β, η)-mechanism (see Rappaport et al. 1983). Here,

$$\beta = \left| \frac{\dot{M}_h}{\dot{M}_c} \right| \tag{3.5}$$

is the mass transfer efficiency, i.e. the fraction of mass lost by the donor (subscript c) accreted by the gainer (subscript h). The angular momentum loss $\dot{J}$ from the system resulting from a given amount of mass loss $\dot{M}$ is

[4]http://www.univie.ac.at/tops/period04/

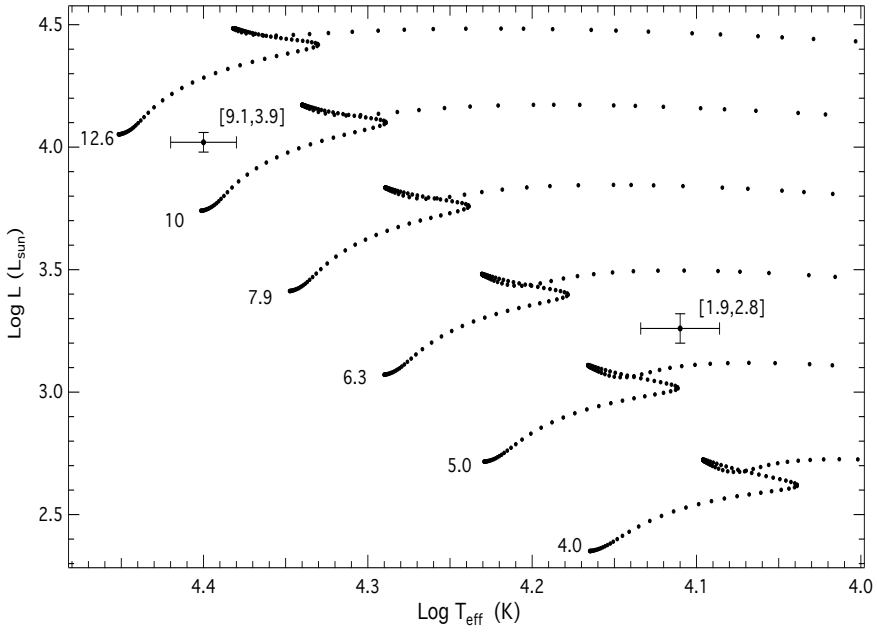

Figure 3.7: Comparison between evolutionary tracks for single stars with solar metallicity (Claret 2004) and the physical parameters of OGLE 05155332−6925581 in the log T_{eff} − log L diagram. Derived mass and log g values are given between parentheses. The evolutionary tracks are labelled with the initial masses.

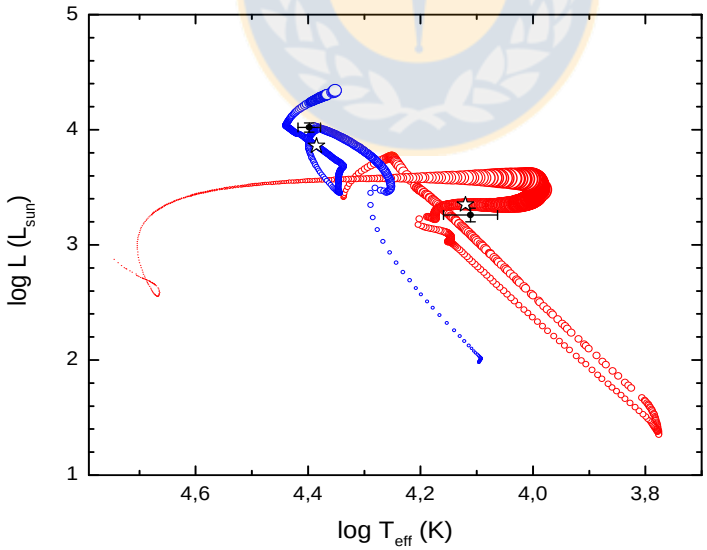

Figure 3.8: Evolutionary tracks for the binary star model from van Rensbergen et al. (2008a) that best fit the data. Donor (red track) and gainer (blue track) evolutionary paths are shown, along with the observations for OGLE 05155332−6925581 (filled circles with errors bars). The best fit is reached at the time corresponding to the model indicated by stars, that is characterized in Table 3.6. Stellar sizes are proportional to the circle diameters.

determined by η, according to

$$\dot{J} = \sqrt{\eta}\, \dot{M}_c\, (1-\beta)\, \frac{2\,\pi\, a^2}{P}, \tag{3.6}$$

with a the orbital seperation and P the orbital period. It can be shown (see e.g. Podsiadlowski et al. 1992) that whenever β and η remain constant throughout the considered timeframe (with indices i for initial and f for final), the resulting period variation is given by

for $0 < \beta < 1$:

$$\frac{P_\mathrm{f}}{P_\mathrm{i}} = \left(\frac{M_{c\mathrm{f}} + M_{h\mathrm{f}}}{M_{c\mathrm{i}} + M_{h\mathrm{i}}}\right)\left(\frac{M_{c\mathrm{f}}}{M_{c\mathrm{i}}}\right)^{3\left[\sqrt{\eta}\,(1-\beta)-1\right]}\left(\frac{M_{h\mathrm{f}}}{M_{h\mathrm{i}}}\right)^{-3\left[\sqrt{\eta}\,\frac{1-\beta}{\beta}+1\right]}; \tag{3.7}$$

for $\beta = 0$:

$$\frac{P_\mathrm{f}}{P_\mathrm{i}} = \left(\frac{M_{c\mathrm{f}} + M_{h\mathrm{f}}}{M_{c\mathrm{i}} + M_{h\mathrm{i}}}\right)\left(\frac{M_{c\mathrm{f}}}{M_{c\mathrm{i}}}\right)^{3\left(\sqrt{\eta}-1\right)} \mathrm{e}^{3\sqrt{\eta}\left(\frac{M_{c\mathrm{f}}-M_{c\mathrm{i}}}{M_{h\mathrm{i}}}\right)}. \tag{3.8}$$

If it is assumed that mass is lost with the specific orbital angular momentum of the gainer, it can be shown that this yields

$$\eta = \left(\frac{M_c}{M_c + M_h}\right)^4, \tag{3.9}$$

resulting in $\eta \ll 1$. On the other hand, if one assumes that matter is lost by the formation of a non-corotating circumbinary disk after passing through the second Lagrangian point, it was shown by Soberman et al. (1997) that a typical value is $\eta = 2.3$.

Given the observational upper limit for the period variation in this work, we have calculated the maximum amount by which the period may have changed during those 15 years. Then, with the equations for the period variation during (non-)conservative mass transfer and using the physical parameters of this particular system, we have calculated that the 15-yr-period variation theoretically for all different combinations of β and η. Results are shown in Fig 3.10.

The zone between the two curves is where the orbital period does not change more in 15 years than is allowed by the observations. The zone above the upper curve is where the period increases too much. This is the case for large β (little mass loss) and/or small η (little angular momentum loss). The zone below the lower curve is where the period decreases too much. This is the case for small β (much mass loss) and large η (much angular momentum loss).
The assumption of specific gainer orbital angular momentum loss (the one used in the calculation of the models) yields $\eta = 0.00089$ for this system. It is obvious that this is way too low in order to fall into the constant period region, and that under this assumption, irrespective of β, the period will increase (much) more than allowed by the observations. Based on this result we argue that another source of angular momentum loss is present in the system, possibly the outflows through L_2 and L_3 reported by M08. Notice that for $\eta \approx 2.3$, representative of angular momentum loss from a circumbinary disc (Soberman et al. 1997), there is a mass loss ($\beta \approx 0.5$) compatible with period constancy in this system.

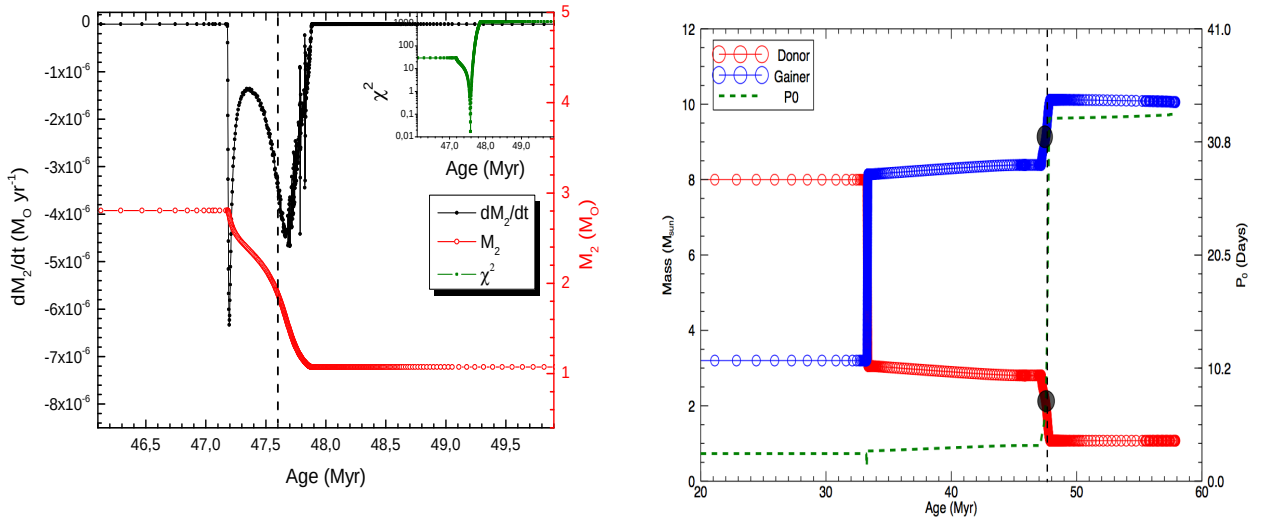

Figure 3.9: *Left*. $\dot{M}_2$ (upper curve) and M_2 for the best evolutionary model, χ^2 is shown in the inset graph. The few spikes in the $\dot{M}_2$ curve reflect minor convergence artifacts produced during the numerical calculations. *Right*. Evolution of orbital period and mass of the components with the mass transfer time for OGLE 05155332−6925581 with the initial orbital period $P_{orb,i}$ = 2.5 days. The vertical dashed lines and filled circles indicates the position for the best model.

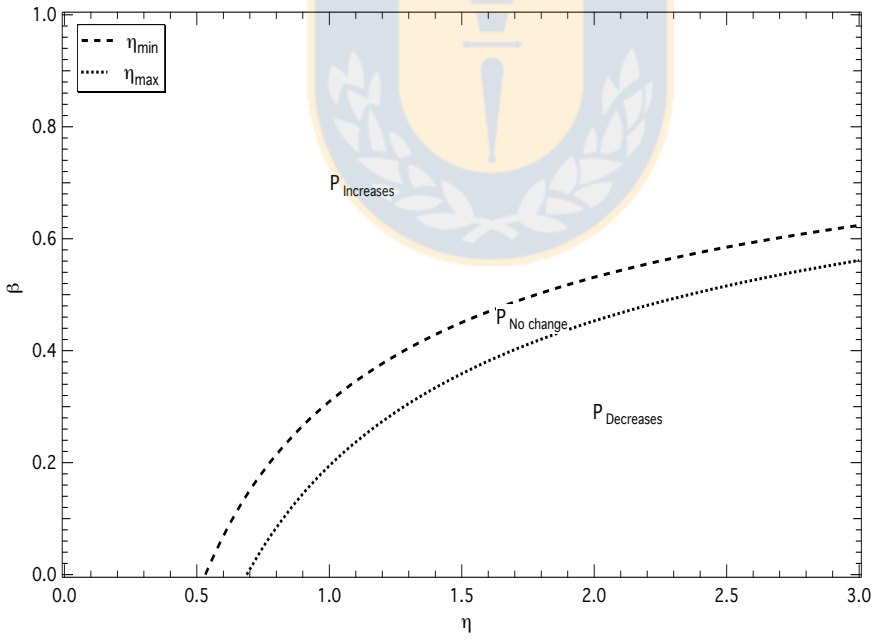

Figure 3.10: η and β parameters controlling the mass and angular momentum loss from the binary according to the model proposed by van Rensbergen et al. (2008a, 2011). The space between the upper and lower curves is for systems with a constant orbital period, according to the observed boundaries for the orbital period variability. The region above the upper curve is for systems showing an orbital period increase, while that below the lower curve is for systems with decreasing orbital period. The η value for OGLE 05155332−6925581 of 8.9×10^{-4} is incompatible with a constant orbital period under the view of the aforementioned model.

3.5 Conclusions

We have presented a detailed spectroscopic and photometric study of OGLE 05155332−6925581 including the analysis of high-resolution spectra and the application of a sophisticated light curve model. The multi-band light curves covering 13.7 years of photometric data from the MACHO and OGLE projects were analyzed along with the radial velocities of both stellar components of this eclipsing binary.

We find that the system is best modelled with a geometrically thin and optically thick disc around the gainer. The analysis of the photometric data has allowed us to derive improved orbital parameters and physical stellar properties such as stellar masses, radii, luminosities and the effective temperatures. All these parameters are given in Table 3.4. Interestingly, the orbital solution remains constant during the long cycle. This means that the disc is not the origin of the long cycle, which is also consistent with previous claims that the source of this variability is not eclipsed (M08). On the other hand, the presence of variable Balmer emission suggests the existence of a fourth component in the system with physical conditions usually associated with optically thin circumstellar gas. Due to the presence of this disturbing component, our line profile investigation is not conclusive regarding gainer critical rotation.

Taking advantage of our new and improved system and stellar parameters, we explored the evolutionary stage of OGLE 05155332−6925581 with the aid of published grids of evolutionary routes for binary systems of similar masses, considering conservative and non-conservative evolution. In particular, the grid of models by van Rensbergen et al. (2008b) were considered in our work. We find the system in a semi-detached configuration and at a stage of rapid mass transfer. The donor has exhausted its hydrogen in its core and we observed the systems in a Case-B mass transfer, with an age of 4.76×10^7 years. Contrary to the case of V 393 Scorpii, the gainer parameters do not deviate too much from a main sequence star of similar mass. This is consistent with a younger accreting object, in the sense that OGLE 05155332−6925581 have not had time to accrete large amounts of matter since it is still experiencing a burst of mass transfer (Fig. 3.9). In contrast, V 393 Scorpii already passed this event in the M12a model and had time to accumulate an important amount of mass in a massive disc. Our studies indicate that the DPV phenomenon is observed at different evolutionary stages; Case-A for V 393 Sco (M12a) and DQ Vel (Barría et al. 2013) and Case-B for OGLE 05155332−6925581 but always during or after a main mass transfer burst.

One notable observation in OGLE 05155332−6925581 is the absence of orbital period change overall, considering the relatively large mass transfer rate. This cannot be explained in terms of the mechanism of mass and angular momentum loss proposed by van Rensbergen et al. (2008a, 2011). Actually, the best model indicates that the system should be found at a phase of fast period increase. We argue that mass outflows through the Lagrange L_2 and L_3 points (as claimed by M08 to explain infrared spectroscopic observations) could extract angular momentum from the system in order to balance the mass exchange and produce a relatively constant orbital period. In addition, if the Balmer and He I emissions are due to a bipolar wind as suggested in the case of the DPV V 393 Scorpii (M12b), this wind could be an additional channel for escape of angular momentum from the system.

It is worthy of mention that current theoretical evolutionary models for close binaries do not include nor predict the DPV phenomenon. As the number of DPVs is relatively large, the phenomenon corresponds to a relatively long phase in the life of binaries of intermediate mass. Our study of OGLE 05155332−6925581 suggests that the DPV phenomenon could have an important effect in the balance of mass and angular momentum during the system evolution. This makes sense if the long cycle in OGLE 05155332−6925581 turns out to be due to a cyclic bipolar wind as suggested for the DPV V 393 Scorpii by M12b.

Chapter 4

ELHC 10: A post-AGB binary with circumbinary and circumstellar discs in the Large Magellanic Cloud

4.1 Introduction

The final evolution of low- and intermediate-mass stars is a fast transition from the asymptotic giant branch (AGB) over the post-AGB transit towards the planetary nebula phase, before the stellar remnant cools down as a white dwarf (WD). Although this scheme of the late phases of stellar evolution may be generally acknowledged, there is no understanding from first principles of several important physical processes that govern these evolutionary phases. The main shortcomings are related to the lack of understanding of the mass-loss mechanisms and mass-loss rate along the AGB ascent, the subsequent shaping processes of the circumstellar shells and discs, and the lack of fundamental understanding of the internal chemical evolution of these stars (Herwig 2005; Höfner 2009; Habing & Olofsson 2003). Our study provides evidence that circumbinary discs in post-AGB stars can be formed by binary star interaction and outflows through the outer Lagrangian points. It provides also support for the idea that low-mass post-AGB stars can be formed by an evolutionary channel different from single stars, specifically by mass depletion of an initially massive star by mass transfer in a semi-detached binary system.

These open questions have led us to investigate the luminous star ELHC 10 located in the LMC bar. ELHC 10 (also known as [BE74] 561, 2MASS J05194770-6939121 or OGLE LMC-LPV-41682) is a binary system with period of 219.9 d[1], located near the nebular complex N 120 (see, Fig. 4.1); it was identified as a Hα emission-line star by Bohannan & Epps (1974). The name ELHC 10 for this object was proposed by Lamers et al. (1999) and de Wit et al. (2002), who searched the EROS database for blue objects with irregular photometric behavior similar to Galactic Herbig Ae/ Be stars in the LMC bar. ELHC 10 was the reddest and brightest star in their sample, with a color $(B - V) = 0.30$ and estimated absolute magnitude of $M_v = -4.7$. The low resolution spectrum showed emission in Hα with equivalent width of -23 Å. Contrary to the other stars in their sample, this star was not an early B star; the spectrum was more compatible with an early F-type giant or supergiant. The spectral type was estimated as F 2/5 I-II, and the object was postulated as a candidate pre-main sequence star by de Wit et al. (2005). Although Herbig Ae/ Be stars (or HAeBe) are emission-line stars of spectral types O, B, A and in a few cases F, and in most instances exhibit IR excesses, which are attributed to dust emission

[1] http://ogledb.astrouw.edu.pl/ ogle/CVS/

Table 4.1: Summary of new spectroscopic observations. The HJDs at mid-exposure are given. Phases refer to the ephemeris given in Eq. 4.1. The signal to noise ratio is calculated at the continuum around Hα. We report the visibility of discrete absorption component in the Na D line as discussed in the text.

Phase	Telescope	Instrument	Date-obs	UT-start	exptime (s)	Airmass	HJD	S/N	DACs
0.04	ESO/3.6	HARPS	2014/11/06	04:19:02	2400	1.419	2456967.693794	14	BACs
0.22	ESO/3.6	HARPS	2010/09/28	05:05:09	2500	1.737	2455467.712230	20	RACs
0.25	ESO/3.6	HARPS	2013/10/08	05:44:38	2000	1.505	2456573.739580	22	RACs
0.47	LCO/Clay	MIKE	2012/02/07	00:22:03	900	1.323	2455964.514824	25	No
0.54	LCO/Clay	MIKE	2013/12/11	00:21:28	600	1.718	2456637.518113	25	No
0.54	LCO/Clay	MIKE	2013/12/12	00:17:46	600	1.717	2456638.515537	25	No
0.62	Irénée Du Pont	ECHELLE	2010/12/27	05:36:25	900	1.387	2455557.743669	40	BACs

Table 4.2: EROS-2 and OGLE II photometry, dereddened B-V color and derived spectral type for ELHC 10.

B_E	R_E	B	V	I	(B-V)	(V-I)	$(B-V)_0$	Spectral Type
13.576	13.503	14.428	13.931	13.484	0.494	0.446	0.32	F5

from circumstellar discs, this star is hardly a HAeBe candidate, due to the much evolved nature of the luminous component.

In this Chapter, we focus on resolving the uncertainty about the nature of this system by performing a thorough analysis of the stellar components and the surrounding environment. High-resolution spectra and very accurate *BRI* light curves allowed us to study ELHC 10 in unprecedented detail for the first time. We find that the brightest member of this binary has a low surface gravity and an atmosphere depleted in refractory elements and can be unambiguously identified as a member of the subclass of post-AGB stars. In addition, we provide convincing evidence for the existence of a circumbinary and a circumstellar disc. This is not an isolated finding, since there is many substantial observational evidence for stable and compact Keplerian circumbinary disks around almost all depleted post-AGB objects, similar to protoplanetary disks around young stellar objects de Ruyter et al. 2006; Gielen et al. 2008, 2009; van Aarle et al. 2011; Hillen et al. 2013, 2015, 2014; Bujarrabal et al. 2015. Additionally the binary nature of the disc source han been further confirmed, with the most famous example certainly being HD 44179, better known as the Red Rectangle Nebula (de Ruyter et al. 2005; Witt et al. 2009; Thomas 2012; Martínez González et al. 2015; Van Winckel et al. 1995, and references therein). Two other important cases similar to ELHC 10, where it has been possible to test the existence of stable Keplerian discs and the correlation with binarity in post-AGB stars have been reported by Gorlova et al. (2012, 2015). Hence, the present chapter aims to inquire into the nature of ELHC 10 bringing new light on the formation of stable discs in these binary systems, which are produced presumably by means of interaction with the companion, when the more massive component becomes either a red giant (RG) or an AGB star. Actually, these amazing and rare systems represent a new evolutionary channel that bypasses a full AGB evolutionary process that until now has been poorly studied.

In this Chapter we call the primary star the stellar component whose absorption lines are detected in the spectrum, while the secondary is the undetected (and more massive) star. Let's remember that this scenario of a less evolved more massive star can be possible in case of past or present mass transfer by Roche-lobe overflow, as happens in Algols. Quantities relative to these stars are labeled with subindexes *1* and *2*, respectively, except in Section 4.2 where we use *c* and *h* for the cooler and hotter star, respectively.

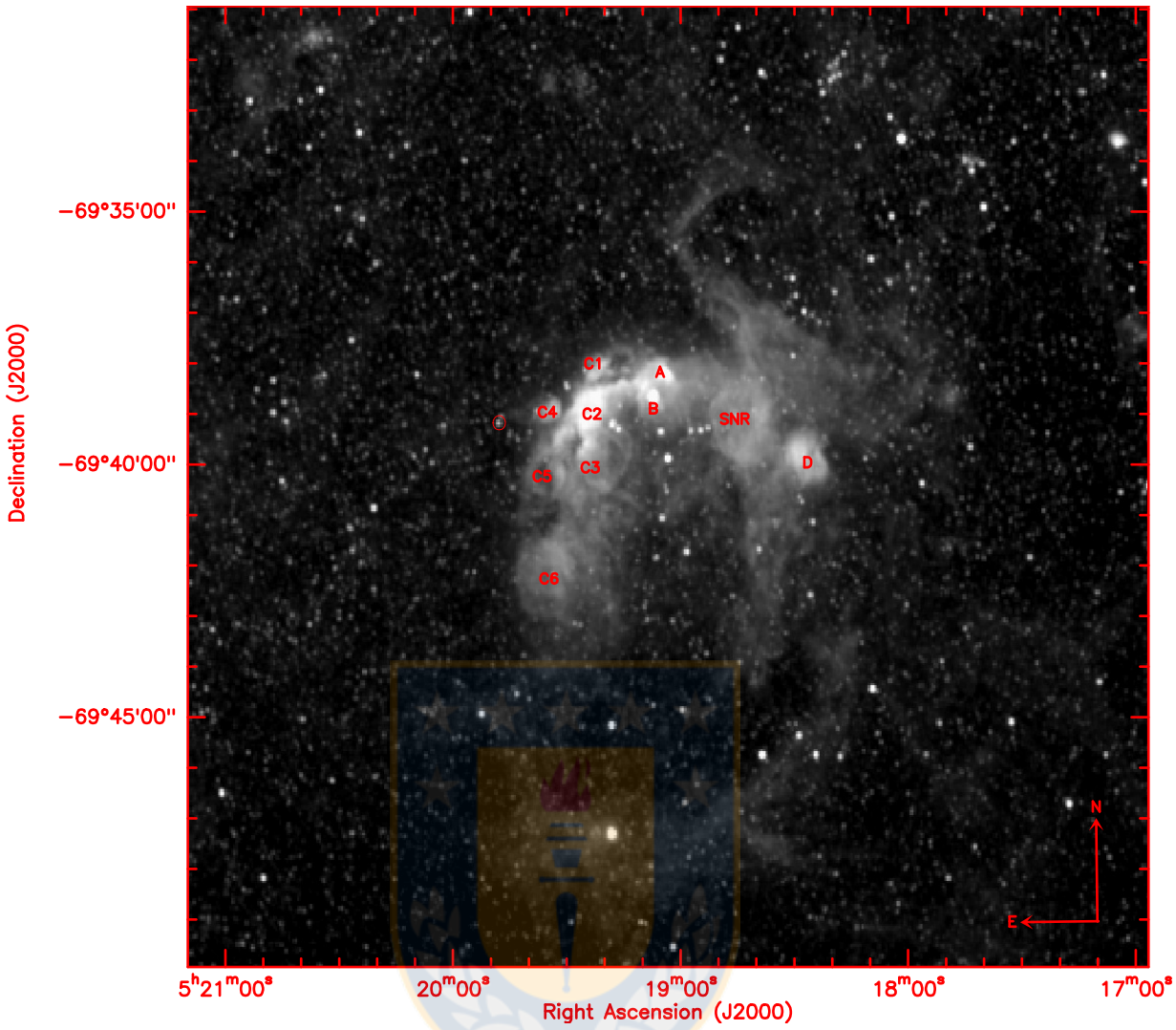

Figure 4.1: Hα image from MCELS on the center of nebular complex N120. The position of ELHC 10 is marked with red circle in the absolute coordinates α(2000)= 05:19:47.70 and δ(2000) = −69:39:12.1. See text for more details.

4.2 Observations and data reduction

4.2.1 Spectroscopy data

We conducted optical spectroscopic observations of ELHC 10 at different epochs during 4 years with several echelle spectrographs. Three high-resolution spectra were obtained in September 2010, October 2013 and November 2014, using the HARPS Echelle Spectrograph mounted on the ESO 3.6 m telescope at La Silla Observatory, Chile. The two CCD chips on this instrument sample the spectral range of 3780-6910 Å. The fibres allowed us to obtain spectra at resolving power ≈ 115000. The HARPS spectra do not include the 5304 to 5337 Å region, because of the gap between the two detectors.

Three additional spectra were secured with the Magellan Inamori Kyocera Echelle (MIKE) spectrograph at the Clay Telescope in Las Campanas Observatory, Chile, in February 2012 and December 2013. This double echelle spectrograph provided wavelength coverage of 3390-4965 Å (blue camera) and 4974-9407 Å (red camera). With a slit width of 0.7 arcsec, the resolving power was 40000. Unfortunately, the two spectra obtained

in December 2013 could not be calibrated in wavelength, but they were used to perform a qualitative analysis of line shapes.

We also obtained one high-resolution ($R \approx 40000$) spectrum with the DuPont Echelle Spectrograph at Las Campanas Observatory, covering the spectral region 4448-7982 Å in December of 2010.

All spectra discussed in this chapter are corrected for earth translational motion and normalized to the continuum. The radial velocities (RVs) are heliocentric. The data reductions were done with standard *IRAF* routines for echelle spectroscopy, including flat and bias correction, wavelength calibration and order merging. No flux calibration was needed for our purposes. A summary of our spectroscopic observations is shown in Table 4.1.

4.2.2 Photometric data

We used the Hα images from the Magellanic Cloud Emission-Line Survey (Smith & MCELS Team 1999) to get information about the conditions surrounding the environment of ELHC 10. As mentioned above, ELHC 10 is located near the nebular complex N 120. This complex is composed of smaller nebulae arranged in a bright incomplete ring with the exciting stars in the centre of the bubble-like nebular complex. Firstly, Henize in 1956 separated the nebula into four brighter overlapping H II regions: N 120 A, B, C and D. Additional images of this region as those of MCELS, revealed that N 120 C was composed of smaller nebulae, denoted C1 to C6, as shown in Fig. 4.1. The heliocentric velocity of the nebulae C1 to C6 were accurately measured to be between 250 and 263 km s^{-1}, with velocity dispersions between 3 to 7 km s^{-1} by Laval et al. (1992). In particular, we are interested in the heliocentric velocities of the nebular complex N 120 C4 and C5 that are closer to our star; these nebulae have heliocentric velocities between 260 and 261 km s^{-1}.

Multi-band and time-series photometry was retrieved from the Optical Gravitational Lensing Experiment in its third phase (OGLE III; Udalski et al. 2002), the Expérience de Recherche d'Objects Sombres in its second phase EROS-2[2] and the Massive Compact Halo Object (MACHOs[3]) project.

The OGLE III photometry was accumulated over an interval of almost 8 years, from July 2001 to May 2009, with the 1.3 meter Warsaw telescope located at Las Campanas Observatory in Chile. The majority of these observations were taken in the *I*-band, typically about 500 points, but ELHC 10 has OGLE II observations too, which increases the number of points up to 1000. About 40-60 observations ($\approx$ 100 with the OGLE II data) were secured in the *V*-band. See Soszyñski et al. (2009) for more information about the procurement of OGLE photometric data.

The EROS-2 observations were obtained using the 1 m Ritchey-Chrétien Telescope at ESO, La Silla-Chile. The telescope was equipped with two cameras, each camera contained eight 2048 $\times$ 2048 detectors mounted in a mosaic pattern. The pixel size is 0.6″, with a typical seeing of 2″ FWHM at the site. The EROS-2 Photometric System consisted of a $B_{\rm E}$ (420-720 nm, blue) band and $R_{\rm E}$ (620-920 nm, red) band. The $B_{\rm E}$ band is close to the Johnson *V*-band, but it is broader. The $R_{\rm E}$ band is intermediate between the bands of Cousins *R* and *I*. The photometric points obtained using the *B*-band generally have better accuracy than in the *R*-band (Grison et al. 1995; Ansari & EROS Collaboration 2001).

The MACHO survey provides instrumental magnitudes for each star in two contiguous "blue" and "red" passbands, labeled *B* and *R*, at different effective wavelengths than the standard B and R passbands in the Johnson-Cousins photometric system (Alcock et al. 1999). The MACHO light curves have between 500 to 1300 points per star, depending on the filter with they taken. The MACHO photometry was accumulated over

[2]http://eros.in2p3.fr/

[3]http://wwwmacho.anu.edu.au/

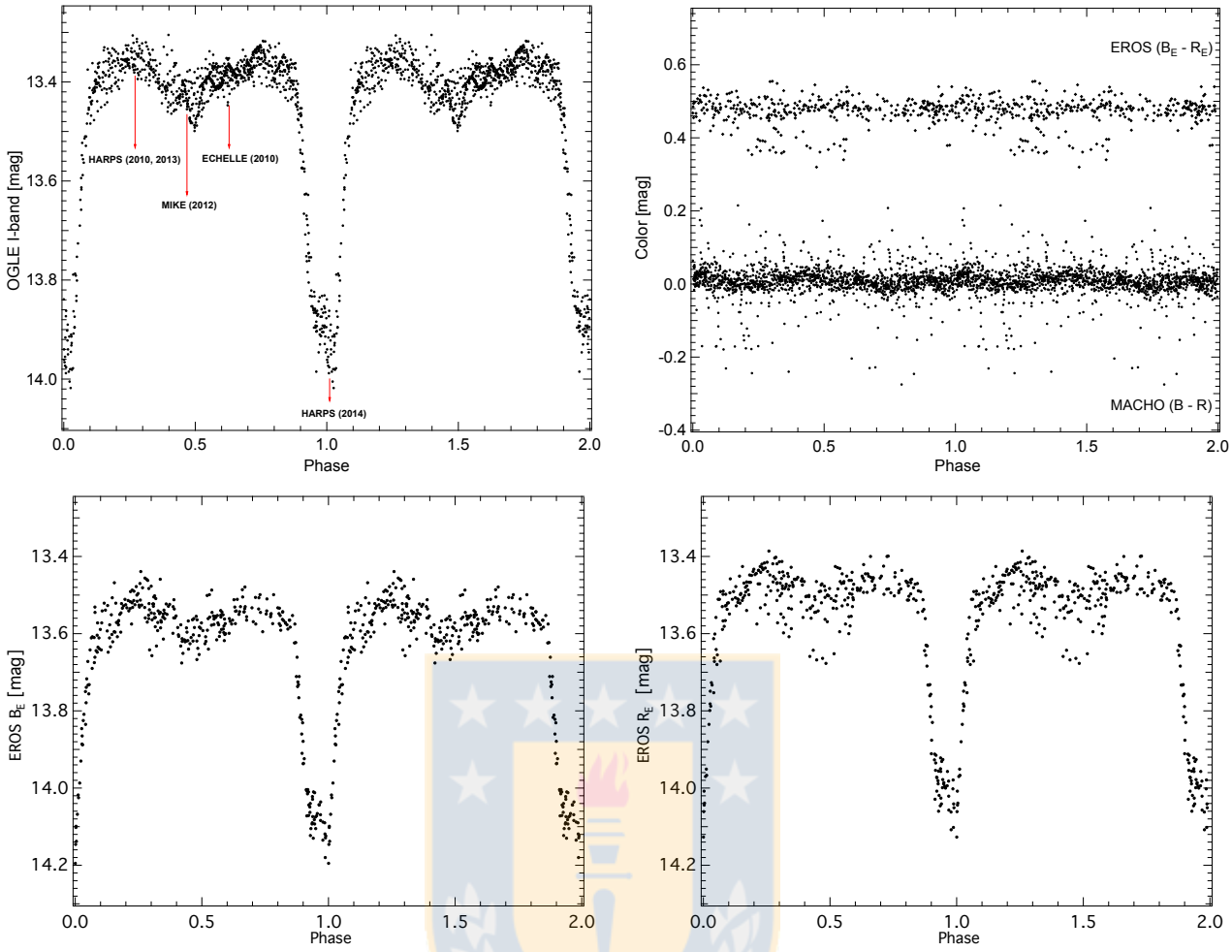

Figure 4.2: I-band, $B_{\rm E}$-band and $R_{\rm E}$-band phase diagrams and EROS-2 and MACHO colors for ELHC 10, showing primary and secondary eclipses. For clarity the phase has been extended over two periods. Epochs for our observations are indicated by arrows. EROS-2 colors are shifted by +0.4 mag.

the interval of 8 years from July 1992 to January 2000. The light curves retrieved from MACHO together with the EROS-2 light curves were used to construct color curves for ELHC 10 (Fig. 4.2).

4.3 Results

4.3.1 Photometric characterization and period search

In Table 4.2 we give the EROS-2 magnitudes and mean BVI magnitudes and colors obtained from the OGLE II catalog. OGLE II has a median seeing for the entire dataset of about 1.3″, and the uncertainty of the zero-point is less than 0.02 mag (Udalski et al. 2000). We calculated derredened $(B-V)_0$ colors assuming mean internal reddening $E(B-V) = 0.16$ mag given by Oestreicher & Schmidt-Kaler (1996), as representative for the gas and dust distribution inside the LMC.

The $(B-V)_0 = 0.32$ color is concordant with a middle F-type giant or supergiant, and this spectral type determination is compatible with the lines observed in the HARPS spectra discussed in Section 4.3.2 and the earlier estimate by de Wit et al. (2005).

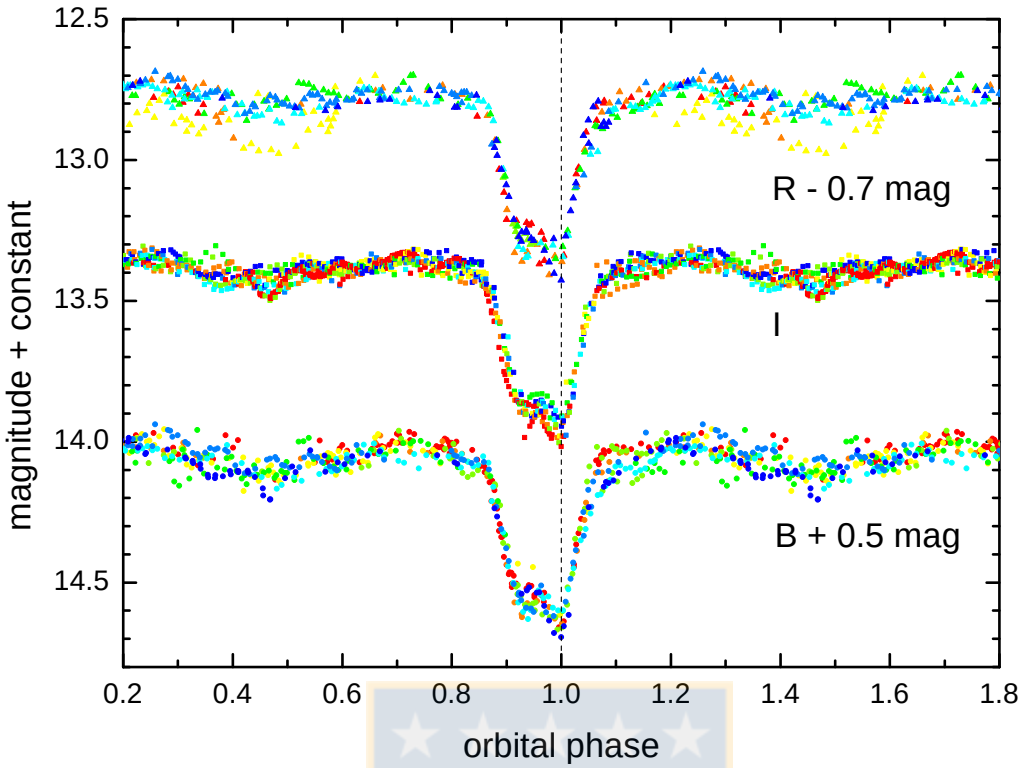

Figure 4.3: The main eclipse at different bandpasses. Data points are colored in a sequence changing with time, in order to see sub-orbital variability.

The OGLE III I-band and V-band light curves have been analyzed utilizing the Phase Dispersion Minimization (PDM) algorithm introduced by Stellingwerf (1978), as implemented in *IRAF*. We have found the fundamental period of 219.9 ± 2.4 days on the I-band time series. The period error is the half-width at half-maximum (HWHM) of the periodogram's peak. The ephemeris for the main eclipses is:

$$T_{min}(\mathrm{HJD}) = 2450582.513 + (219.9^{\,d} \pm 2.4) \times E. \tag{4.1}$$

We have modeled the OGLE III and EROS-2 light curves with a Fourier series including the orbital frequency plus harmonics following the method described by Mennickent et al. (2012). The analysis of the residuals of the light curve regarding this model did not reveal any additional periodicity.

Afterwards, OGLE III and EROS-2 light curves were folded using the ephemeris given by Eq. 4.1, and the result is shown in Fig. 4.2. The structure seen in the eclipses of ELHC 10 in particular the stop before minimum, is similar to that exhibited in the newly discovered systems OGLE-LMC-ECL 11893 (Dong et al. 2014), OGLE-BLG182.1.162852 (Rattenbury et al. 2015) and OGLE004633.76-731204.3 (Mennickent et al. 2010b). These systems have been described as long-period eclipsing binaries with circumstellar discs.

The OGLE V-band and I-band light curves were phased with the 219.9 day period, and then interpolated to a constant phase-step to get a representation of the average light variability during the cycle at each band. The color $V - I$ was constructed by subtracting both averaged light curves; it does not show any significant change during the cycle, but remains constant at the value $V - I = 0.5$, representative of a F 2 - F 5 type supergiant. The same color constancy is observed in MACHO and EROS colors (Fig. 4.2). Actually, the MACHO colors show the system slightly bluer by 0.01 mag. at quadratures. The almost gray and irregular eclipse is compatible with occultation of the primary by a non-stellar object having a similar temperature as the F-type supergiant.

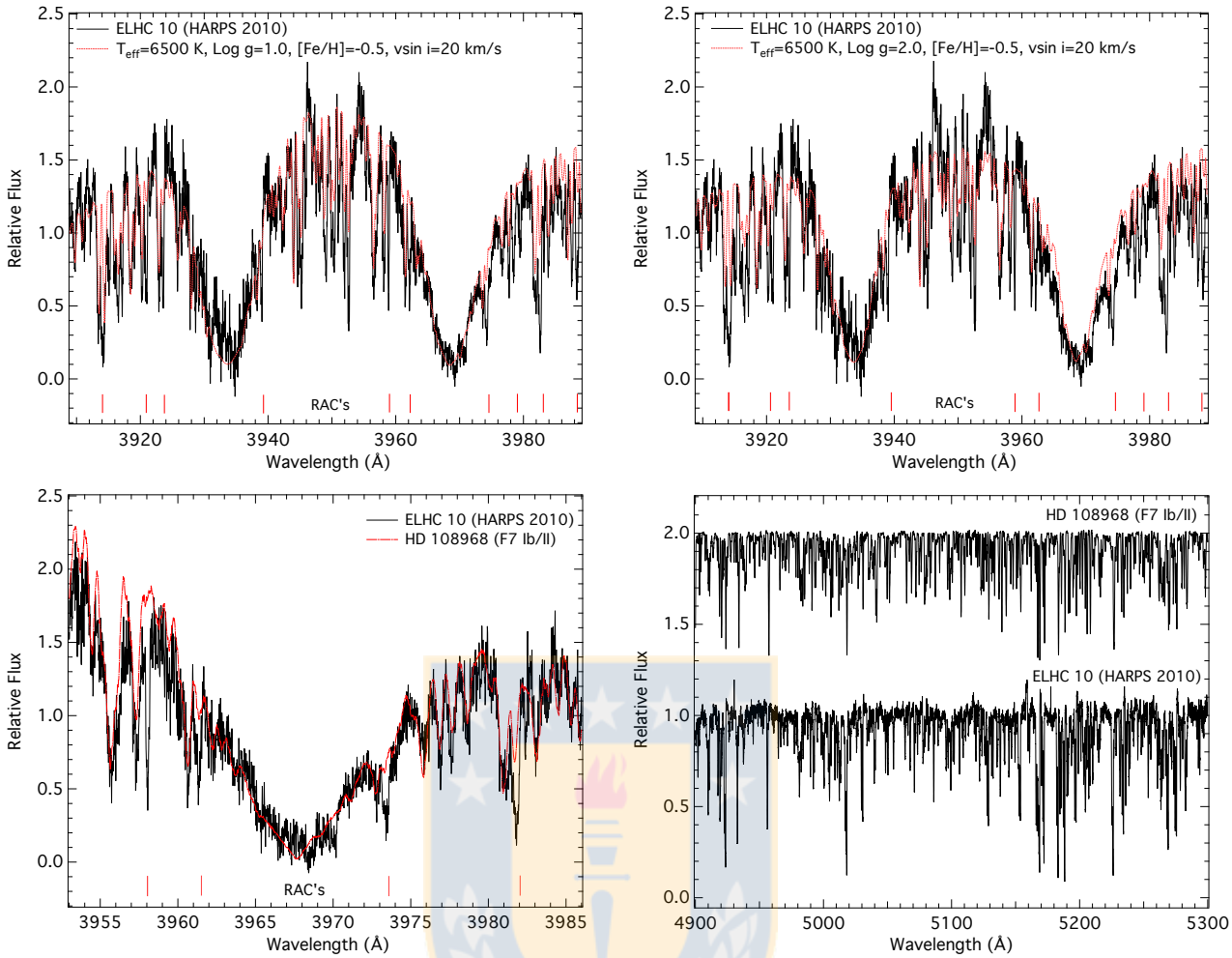

Figure 4.4: *Upper panel:* HARPS (2010) spectrum of ELHC 10 and synthetic spectra from Coelho et al. (2005) with different $\log g$ and low metallicity. *Bottom panel:* The optical spectrum of ELHC 10 and template spectrum taken from UVES atlas covering the H line of Ca II and metallic lines in the region 4900−5300 Å. Positions of some red absorption components (RACs) are indicated. The template spectrum have been offset in flux for convenience and ELHC 10 have been blue-shifted to the rest frame.

The variability of the eclipse shape at different epochs and also short-term quasi-periodic oscillations can be observed in Fig. 4.3. The scatter observed in the *R*-band at certain phases occurs only during one epoch (yellow points) and near secondary eclipse; it could be instrumental error related to problems with removal of Hα luminosity of the background nebulosity or alternatively, reveals changes in Hα emission strength.

4.3.2 Temperature and surface gravity of the primary star

We compared our spectra with the library of synthetic stellar spectra given by Coelho et al. (2005). The synthetic spectra with low metallicity were adopted, for which, upper and lower limits of the metallicity were established from the mean values of metallicity distribution derived by Carrera et al. (2008) for the chemical enrichment history of the LMC (i.e., $-1.5 \leq$ [Fe/H]≤ -0.5). The spectra with effective temperatures $3500 \leq T_{\rm eff} \leq 7000$ and surface gravities $0.0 \leq \log g \leq 3.0$ were subtracted from our spectrum in the region 3911-3993 Å covering the Ca II H/K lines in order to find the residual spectrum with the smaller standard deviation, considered as the

Table 4.3: Fluxes and their errors derived from magnitudes reported in different databases.

Filter	λ (Å)	f_λ (erg/cm^2/s/Å)	σf_λ (erg/cm^2/s/Å)
B	4413.08	1.30E-14	1.79E-16
V	5512.12	9.38E-15	1.30E-16
DENIS I	7862.10	4.97E-15	1.37E-16
I	8059.88	4.86E-15	2.24E-17
J	12350	1.66E-15	6.11E-17
H	16620	7.48E-16	2.76E-17
K_s	21590	2.91E-16	1.61E-17
WISE1	33526	7.93E-17	2.05E-18
IRAC1	35634	5.79E-17	1.60E-18
IRAC2	45110	2.61E-17	6.97E-19
WISE 2	46028	2.60E-17	6.46E-19
IRAC3	57593	1.17E-17	5.41E-19
IRAC4	79594	4.67E-18	7.74E-19
WISE3	115608	4.76E-18	1.75E-19
WISE4	220883	4.89E-18	3.47E-19

References: I data from DENIS Deep Near Infrared Survey (Cioni et al. 2000), *BVI* data from OGLE II - III survey (Udalski et al. 2000, 2008), JHK_s data from 2MASS all-sky survey (Skrutskie et al. 2006), *IRAC* (Meixner et al. 2006) and *WISE* using data retrieved from the *Spitzer Space Telescope* Archive (Wright et al. 2010).

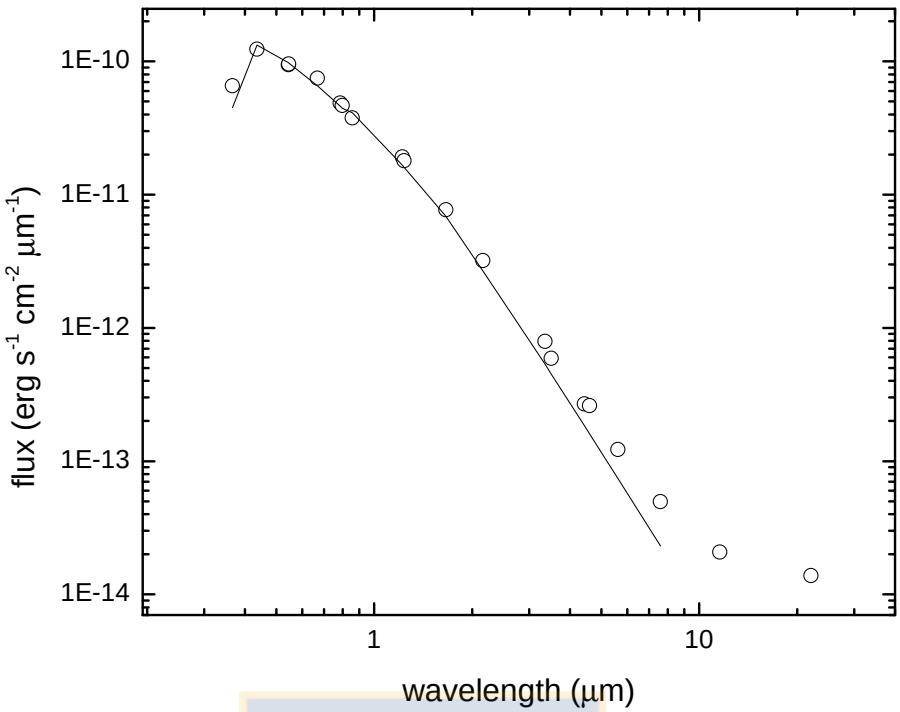

Figure 4.5: Spectral energy distribution for ELHC 10, constructed with the flux values listed in Table 4.3 and the best fit. The two redder fluxes were excluded from the fit since the corresponding W3 and W4 WISE images does not show the presence of the system, only the sky at the target position.

best model spectrum.

We find that a spectrum with $T_{\rm eff} = 6500$ K, $\log g = 1.0$ and [Fe/H]$= -0.5$ reproduces well this part of the HARPS spectrum in 2010. We estimate the accuracy of our adjustment to be ± 250 K in T_{eff} and ± 0.5 dex in $\log g$ and [Fe/H]. In addition, we used the tabulated effective temperature of supergiants as a function of spectral type from Kovtyukh (2007) to independently verify the range of spectral type for ELHC 10 based on its $T_{\rm eff}$: F 3 (6700 K) – F 6 (6270 K), which is consistent with the photometric estimation. In Fig. 4.4 we show the HARPS spectrum taken in 2010 for ELHC 10, along with the best synthetic spectrum and also the spectrum of the standard HD 108968 (F 7 Ib/II $v \sin i = 22 \pm 1.8$ km/s) taken from the atlas UVES-POP[4] (Bagnulo et al. 2003).

The fact that no veiling was necessary to fit the lines in the spectrum with a supergiant template indicates that most of the optical flux comes from this star, and the contribution of the companion is very small.

4.3.3 Analysis of the spectral energy distribution

We compiled fluxes at different wavelengths from several sources to build the spectral energy distribution (SED) from optical to far-infrared. Magnitudes m_λ were transformed to fluxes f_λ using the standard zero magnitude fluxes; the results are shown in Table 4.3.

We performed a fit to the SED by means of Marquant-Leveberg non-linear least-square algorithm by minimization of χ^2 of the function:

$$f_\lambda = f_{\lambda,0} 10^{-0.4E(B-V)[k(\lambda-V)+R(V)]}, \tag{4.2}$$

[4]http://www.eso.org/sci/observing/tools/uvespop.html

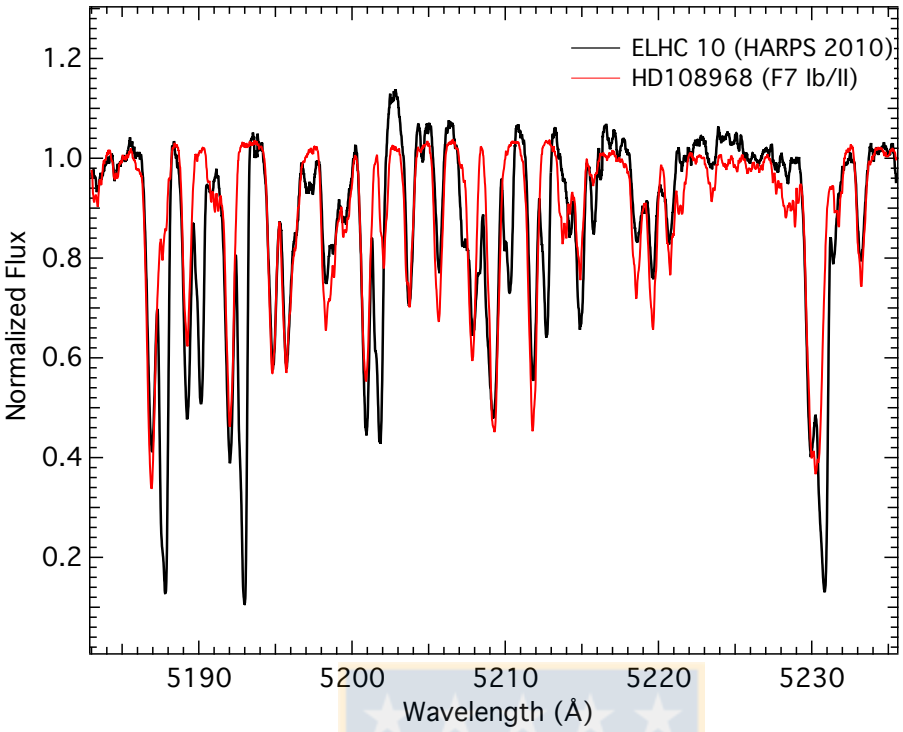

Figure 4.6: Spectrum of ELHC 10 overplotted with the template spectrum, exhibiting red absorption component (RAC's) in the metallic lines.

where

$$f_{\lambda,0} = (R_1/d)^2[f_{1,\lambda}], \tag{4.3}$$

and f_1 is the flux of the primary star, $k(\lambda - V) \equiv E(\lambda - V)/E(B - V)$ is the normalized extinction curve, $R(V) \equiv A(\lambda)/E(B - V)$ is the ratio of extinction at V to reddening, d is the distance to the binary and R_1 is the primary physical radius. Since the secondary is not detected in the spectrum it was not considered in the fit. For further information about the fitting procedure see Mennickent et al. (2010a).

The parameters $T_{\rm eff}$ and $\log g$ obtained in Section 4.3.2 were used to obtain a synthetic spectrum with metallicity −2 from the grid of BT-NextGen (AGSS2009) spectra available at the Spanish Virtual Observatory[5] and the parameters R_1/d and $E(B - V)$ were the free parameters. We minimized the χ^2 between the observed SED and the synthetic spectrum and converted to absolute units using the distance to the LMC of μ_{LMC} = 18.493 ± 0.008 mag (Pietrzyński et al. 2013).

The result of the fit gives $R_1 = 61 \pm 10\,R_\odot$ and $E(B-V) = 0.039 \pm 0.089$, compatible with the excess derived from the Hα emission strength in Sec. 4.4. The radius and surface gravity give $M_1 = 0.6 \pm 0.4$ M$_\odot$. The fit and the data are shown in Fig. 4; the small infrared excess remaining at WISE W_1 and W_2 bands could indicate emission from circumstellar material. The obtained radius excludes the main sequence nature for the primary, as expected from the large brightness of this cool star located in the LMC.

[5]http://svo.cab.inta-csic.es/main/index.php

Table 4.4: Heliocentric radial velocities for ELHC 10. Residuals from the best fit function are indicated as $O - C$.

Phase	Y II (4 883.7 Å) (km s^{-1})	$O - C$ (km s^{-1})	Ba II (4 934.1 Å) (km s^{-1})	$O - C$ (km s^{-1})	Ba II (5 853.7 Å) (km s^{-1})	$O - C$ (km s^{-1})	Ca I (5 857.5 Å) (km s^{-1})	$O - C$ (km s^{-1})
0.04	232.919 ± 0.112	1.016	231.587 ± 0.485	-0.317	231.623 ± 0.059	-0.281	234.234 ± 0.219	2.330
0.22	195.037 ± 0.010	-1.392	194.793 ± 0.004	-1.636	194.252 ± 0.083	-2.176	194.193 ± 0.523	-2.236
0.25	198.663 ± 0.131	0.221	198.880 ± 0.448	0.438	199.516 ± 1.132	1.074	201.210 ± 1.527	2.768
0.47	269.915 ± 0.117	0.711	267.977 ± 0.028	-1.228	269.933 ± 0.052	0.729	271.836 ± 0.566	2.632
0.62	322.264 ± 0.187	-0.604	321.525 ± 1.301	-1.342	322.760 ± 0.049	-0.108	322.510 ± 0.220	-0.358

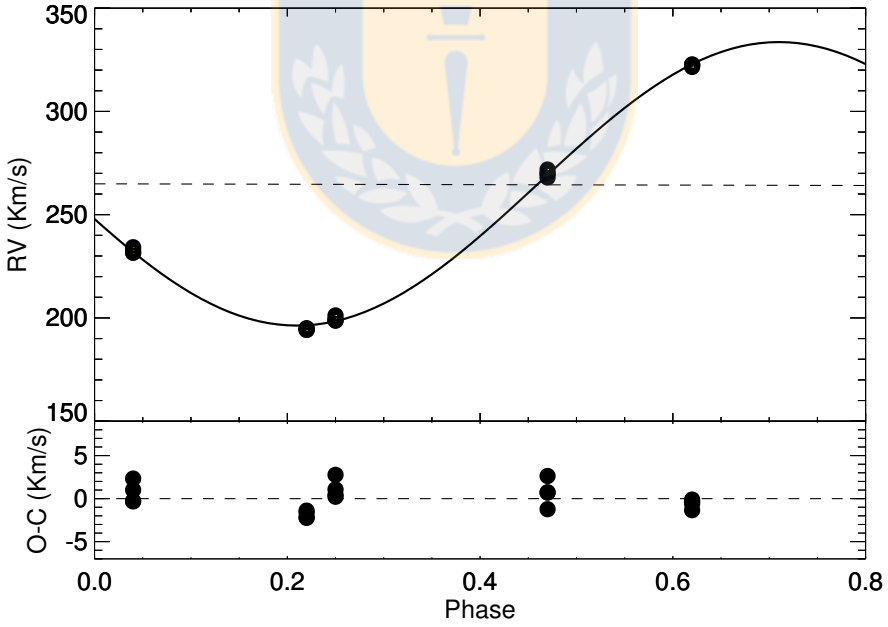

Figure 4.7: *Upper panel*: radial velocities of ELHC 10 phased with a period 219.9 days and the best-fitting solution. The horizontal dashed line marks the corresponding systemic velocity. *Bottom panel*: residuals from the fit.

4.3.4 Radial velocity study of photospheric lines

The optical and near-infrared spectrum of ELHC 10 is dominated by metallic lines of the F-type primary. The spectral lines are redshifted by amounts of roughly 3 Å, typical for LMC stars. Interesting, some metallic lines are split in discrete absorption components (Fig. 4.6). Line identification was made by comparing line positions with theoretical line wavelengths (Kurucz 1993). Radial velocities (RVs) were measured by calculating the positions of the line centre with a Gaussian fit using the IRAF *SPLOT* task. In the case where lines were blended, we employed a deblending method to isolate the components by fitting multiple gaussians to the observed profiles. We performed this task with the *IRAF* deblending 'd' routine available in the *SPLOT* package.

Firstly, we measured RVs of lines clearly representative of the primary motion. The four absorption lines used for this purpose were Ba II 4934.1 and 5853.7 Å, Ca I 5857.5 Å and Y II 4883.7Å. These lines were chosen because they are "well behaved", i.e. they are not too weak to be measured, they are not contaminated by telluric features, they are not blends with lines from other elements, the lines are almost always symmetrical in comparison with the other metallic lines and they do not show additional discrete absorption components similar to other metallic lines in the optical spectra of ELHC 10. In Table 4.4 we report the RVs determined for each of these lines. The measures reflect very well the orbital motion of the primary (Fig. 4.7).

We assume a circular orbit and fit the RVs with a sine function of the form:

$$RV = \gamma + K \sin\left[2\pi(\Phi + \Phi_0)\right]. \tag{4.4}$$

Considering all velocities with equal statistical weight we find a system velocity $\gamma_1 = 264.935 \pm 0.432$ km s^{-1}, semi-amplitude $K_1 = 68.639 \pm 0.563$ km s^{-1} with rms 6 km s^{-1} and phase shift $\Phi_0 = -0.460 \pm 0.01$. The existence of a small phase shift between the spectroscopic and photometric ephemerides is compatible with the fact that we use the ephemerides for the very minimum of the light curve, which is shifted by about +0.05 from the minimum of the light curve assuming symmetrical eclipse.

We reviewed the spectra throughout the spectral range. But, there is no indication for the secondary component even at the minimum. In the spectra, only features of the primary star and DAC's contributions are present, as can be see in Table 4.5.

4.3.5 Radial velocity study of non-photospheric lines

The other prominent lines seen in the spectra are due to Ca II, Na I and a large number of lines from Fe II, Ti II, Na I and Si II and other species. They display line splitting as discrete red or blue extra absorptions depending on the phase in which the spectrum was obtained. These DACs were denominated RACs or BACs; they are not due to another stellar component because their variable morphology is incompatible with this assumption. Once the orbital motion of the primary was determined, DACs were clearly identified in the lines. In this section we report the RV measurements of these DACs.

For the present study we selected 202 prominent lines to obtain accurate radial velocities. The result of this procedure is summarized in Table 4.5. We give the average RV of the primary, along with the velocity of the additional components for each ion. The internal error, measured by weighting the internal *rms* of individual ions in photospheric lines, usually do not exceed ± 3 km s^{-1}. In Fig. 4.8, we show the distribution of relative velocity between the main (photospheric) component (V_{Main}) and its associated RAC or BAC ($V_{Rac/Bac}$).

We performed a non-linear least squares fit to the DAC velocity distributions using a gaussian function of the form:

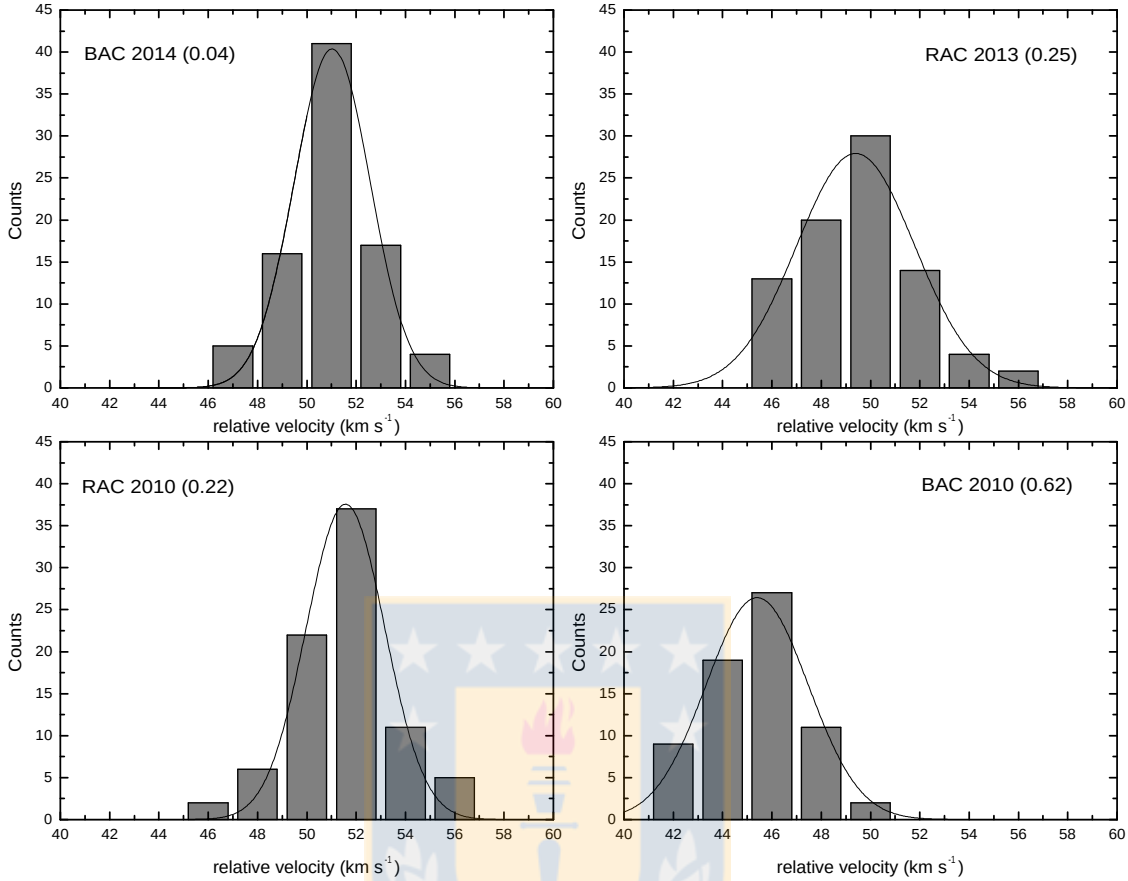

Figure 4.8: Distributions of radial velocities (absolute values) of the associated RAC/BAC relative to the stellar line component at different orbital phases. The best gaussian fits to the distributions are also shown. Their parameters are given in Table 4.6.

$$y = A \exp\left(- \frac{(x - x_c)^2}{2w^2} \right). \tag{4.5}$$

The coefficients A, x_c and w are given in Table 4.6. We notice relatively narrow distributions and that the velocity of blue or redshifted absorptions are always near ± 50 km s^{-1}, except at $\Phi_o = 0.62$ when they are around -45 km s^{-1} (Fig. 4.8). The orbital variability of radial velocities for some non-photospheric lines will be discussed in Section 4.3.7.

We also find narrow absorption components at velocity 252 km s^{-1} at the Si II 6347 and 6371 Å lines. These absorptions are visible only at main eclipse, they have $FWHM \sim 3$ km s^{-1} and are shifted by -8 km s^{-1} with respect to the velocity of the system center of mass; they might be produced in a slowly expanding disc surrounding the binary. In addition, we discard the origin in the supergiant because of the very narrow line width, not comparable with all the photospheric lines in the spectrum. However, we cannot discard an origin in the accretion disc.

Table 4.5: Summary of heliocentric radial velocities (in km s^{-1}) for the spectra in seasons 2010, 2012, 2013 and 2014. We give the velocity of the main component followed by the velocity of the associated RAC / BAC relative to this component. The number of lines used in the averages is listed between parentheses. Errors reflect the rms of the RVs per lines within an ion. Note that at phase 0.47 (season 2012) no RAC / BAC were observed.

Ion	2014 (BAC) $\Phi_0 = 0.04$	2010 (RAC) $\Phi_0 = 0.22$	2013 (RAC) $\Phi_0 = 0.25$	2012 $\Phi_0 = 0.47$	2010 (BAC) $\Phi_0 = 0.62$
Ba II	232 ± 1 (4); 51 ± 2 (3)	195 ± 1 (4)	199 ± 1 (4)	269 ± 1 (4)	321 ± 1 (4)
Ca I	234 ± 3 (3); 47 (1)	198 ± 3 (3); 53 (1)	199 ± 3 (3); 55 (1)	271 ± 3 (3)	324 ± 2 (3); 46 (1)
Ca II	220 ± 1 (2)	210 ± 19 (2)	217 ± 29 (2)	271 ± 15 (2)	...
Cr II	232 ± 1 (9); 50 ± 2 (4)	195 ± 2 (9); 50 (1)	198 ± 1(9); 46 (1)	268 ± 3 (9)	321 ± 2 (9); 46 (1)
Fe I	232 ± 1 (20); 50 ± 3 (12)	195 ± 2 (20); 51 ± 2 (14)	198 ± 2(20); 49 ± 3 (14)	267 ± 2 (20)	322 ± 2 (20); 47 ± 2 (10)
Fe II	233 ± 2 (26); 50 ± 2 (26)	194 ± 2 (28); 51 ± 2 (28)	198 ± 2(28); 49 ± 3 (28)	267 ± 2 (28)	323 ± 2 (26); 45 ± 2 (26)
Mg I	234 ± 1 (5); 51 ± 1 (3)	195 ± 2 (5); 49 ± 1 (3)	198 ± 2(5); 47 ± 1 (3)	267 ± 1 (5)	323 ± 1 (5); 44 ± 1 (3)
Mg II	231 (1)	195 ± 2 (2)	196 ± 1 (2)	265 ± 4 (2)	321 (1)
Na I	233 ± 1 (2); 51 ± 1 (2)	192 ± 1 (2); 55 ± 1 (2)	198 ± 1 (2); 49 ± 1 (2)	266 ± 1 (2)	323 ± 1 (2); 45 ± 2 (2)
Sc I	234 (1); 53 (1)	196 (1); 51 (1)	200 (1); 50 (1)	267 (1)	324 (1); 42 (1)
Sc II	234 (1); 53 (1)	196 (1); 52 (1)	198 (1); 48 (1)	266 (1)	323 (1); 41 (1)
Si II	233 ± 1 (6); 52 ± 1 (3)	194 ± 4 (6); 45 (1)	197 ± 4 (6); 41 (1)	268 ± 3 (6)	321 ± 1 (6); 44 ± 1 (1)
Sr II	235 ± 1 (2); 52 ± 3 (2)	196 ± 4 (2); 51 ± 6 (2)	199 ± 3 (2); 49 ± 7 (2)	268 ± 3 (2)	324 ± 1 (2); 42 ± 2 (2)
Ti I	233 (3); 51 ± 2 (3)	196 ± 1 (3); 51 ± 2 (3)	198 ± 1 (3); 49 ± 1 (3)	269 ± 1 (3)	322 ± 1 (3); 46 ± 1 (3)
Ti II	233 ± 1 (19); 51 ± 2 (19)	195 ± 3 (24); 51 ± 1 (23)	199 ± 4 (24); 49 ± 2 (23)	267 ± 2 (24)	323 ± 1 (19); 45 ± 2 (19)
Y II	232 ± 1 (6); 51 ± 2 (3)	194 ± 2 (6); 51 ± 1 (2)	196 ± 2 (6); 50 ± 2 (2)	267 ± 3 (6)	323 ± 1 (6); 46 ± 1 (1)
Mean (km s^{-1})	233 ± 3; 51 ± 2	195 ± 4; 51 ± 2	198 ± 5; 49 ± 3	267 ± 2	323 ± 1; 45 ± 1
Weighted mean (km s^{-1})	231; 51	193; 50	197; 48	266	323; 45

Table 4.6: Coefficient of the Gaussian fits (Eq. 4.5) shown in Fig. 4.8

Phase	x_c	w	A
0.04	51.028 ± 0.159	1.547 ± 0.138	40.360 ± 3.300
0.22	51.568 ± 0.140	1.598 ± 0.137	37.564 ± 2.775
0.25	49.398 ± 0.338	2.396 ± 0.362	27.915 ± 3.405
0.62	45.401 ± 0.206	2.074 ± 0.211	26.432 ± 2.279

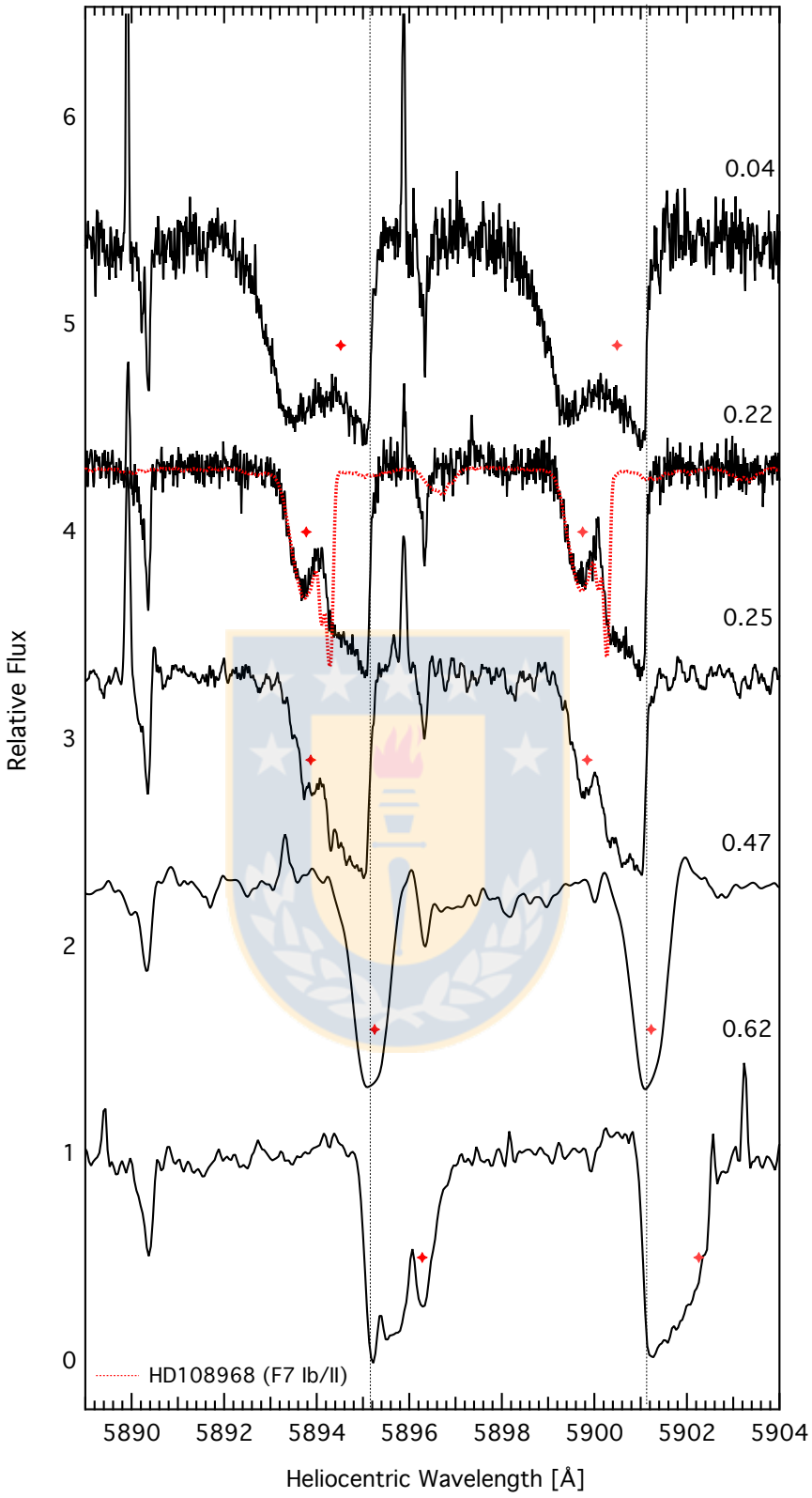

Figure 4.9: Na I D 1 and D 2 lines as a function of the heliocentric wavelength. The dashed lines mark our systemic velocity of 265 km s^{-1} for each line, the red points indicate the photospheric velocity of the F-supergiant star. The spectrum of the standard HD 108968 is overplotted as illustration at phase 0.22. It is possible to observe the separated contributions due to stellar and circumstellar media in 5 890 Å and 5 896 Å. The labels in the upper right of each spectrum indicate the orbital phase.

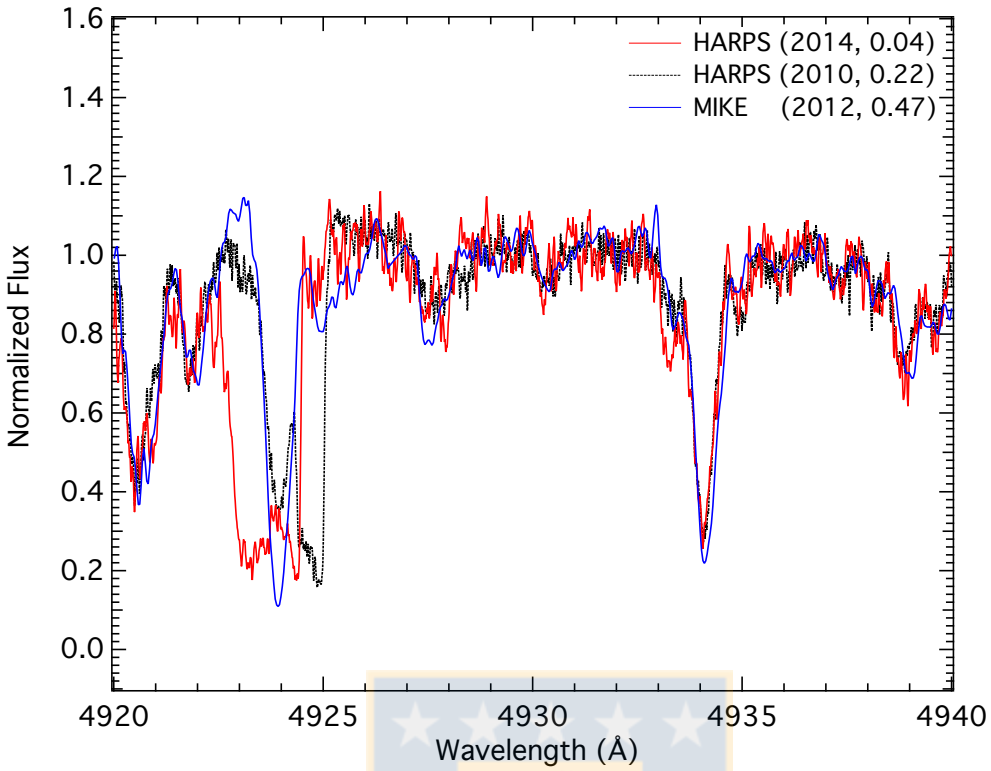

Figure 4.10: The Fe II 4923 Å and Ba II 4934 Å lines show the apparition of RACs and BACs and drastic changes with orbital phase in Fe II 4923 Å, whereas Ba II 4934 Å is less affected by circumstellar material. Note the almost constant line strength independent of the phase. The spectra are shown in the primary velocity frame.

4.3.6 Na I D-line profiles

Perhaps the most interesting parts of the Na I D-line profiles are the discrete absorption components present at almost all orbital phases, appearing as red absorption components near quadrature (Φ = 0.22), disappearing near Φ = 0.47 and changing to blue absorption components from Φ = 0.62 to inferior conjunction (Φ = 0.04, Fig. 4.9). DACs in metallic lines follow the same behavior, and are generally of comparable strength and sometimes stronger than the main component. A triple Gaussian fit to the Na D lines at phases 0.22 and 0.25 gives a ratio of equivalent widths close to unity. The ratio of the sodium lines is equal to 2 for optically thin material and the ratio approaches unity for optically thick gas. Therefore the gas producing the Na D absorption must be optically thick. Because our star is located in the LMC, an important contribution of interstellar medium to the sodium lines would not be expected, due to the low metallicity. From the above we deduce that the material contributing to the extra absorption components in the Na D line comes from circumstellar material of high optical depth in the binary system.

Such behavior in the shape of the spectral features in Na I lines is very similar to the spectral features present in the Fe II and Ti II lines. But quite different are the changes in the shape of ions such as Ba II, Mg II and Ca I-II which usually do not show DACs (Fig. 4.10).

4.3.7 Fe I and Fe II profiles

The variations in the profiles in both Fe II 4923 and 5018 lines are hard to interpret in terms of simple changes in the stellar atmospheric parameters, such as the effective temperature, surface gravity and microturbulent

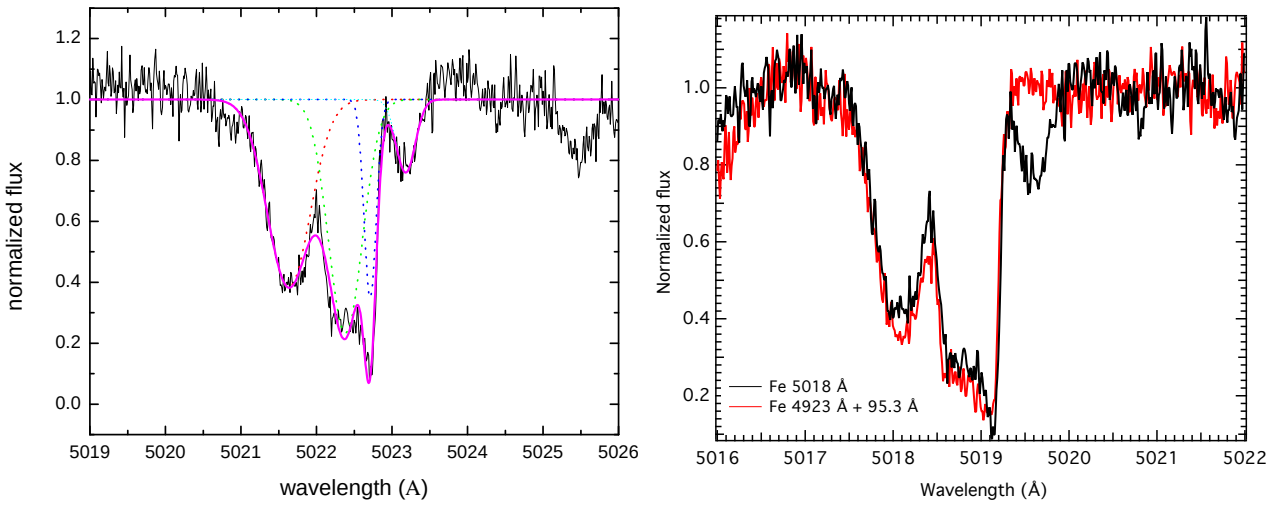

Figure 4.11: *Left panel:* Multiple Gaussian fit of the Fe II 5018 Å line revealing several discrete absorption components. *Right panel:* Overplotting of the Fe II 4923 Å and 5018 Å lines showing one additional red absorption component in Fe II 5018 Å. The 4953 Å line was redshifted by 95.3 Å. Both panels refer to the 2010 HARPS spectrum at $\Phi_o = 0.22$.

velocity (Fig. 4.11). Actually, multiple components in the iron lines, up to 4 components, can sometimes appear. These components are characterized by different line widths, revealing different physical conditions in the formation regions. A similar behavior (unexplained) is reported in the interacting binary candidate OGLE004633.76-731204.3 which harbors an A-type supergiant (Mennickent & Smith 2010). In Fig. 4.12 we show the radial velocities of 3 components of Fe II line at 5018 Å. It is clear how the photospheric line follows the primary motion, narrow stationary components remain stable with the velocity of the system center of mass, and DACs move from the blue to the red side of the photospheric line. A similar behavior is followed by DACs in other metallic lines.

The apparition of these variable and complex double-bottomed shapes in the profile of metallic lines in iron-groups elements, probably reflects large-scale motions with different radial velocities, in shock regions, possible representing by multiple layers in between the stars. In addition, these spectral characteristics appear and are stronger at or near quadratures and disappear during secondary eclipse, as evident in the 2012 spectrum in Figs. 4.9 and 4.10. All this behavior of features strongly modulated with the orbital period suggests that DACs are produced in gas streams inside the binary system.

4.3.8 Signatures of s-process elements and abundance determination

The s-process nucleosynthesis is characterized by the presence of elements created by slow neutron capture reactions in the absorption features of elements such as Ba II at 4554.03 Å, 5853.68 Å, 6141.72 Å, and 6496.89 Å, Sr II line at 4077.71 Å and 4215.52 Å (see, Pereira & Miranda 2007 and Kamath et al. 2014, for further details on identifying signatures of s-process enhancements in post-AGB stars).

The Ba II, Ba I and Sr II lines are present in our spectra and are stronger in the primary of ELHC 10 than in the F-type supergiant UVES-POP template spectrum. This fact suggests that s-process enrichment has taken place in the primary. In order to calculate the abundances of α-elements and s-process species, we used the MIKE spectrum obtained on February 07, 2012 for analysis. This observation was carried out near maximum light at a phase ($\Phi = 0.47$) corresponding to the superior conjunction of the post-AGB star, when its obscuration by the circumstellar disc and the contribution from secondary star should be minimal. Additional to this, the metallic lines at this phase do not present DACs and were nearly symmetric and hence easy to measure providing

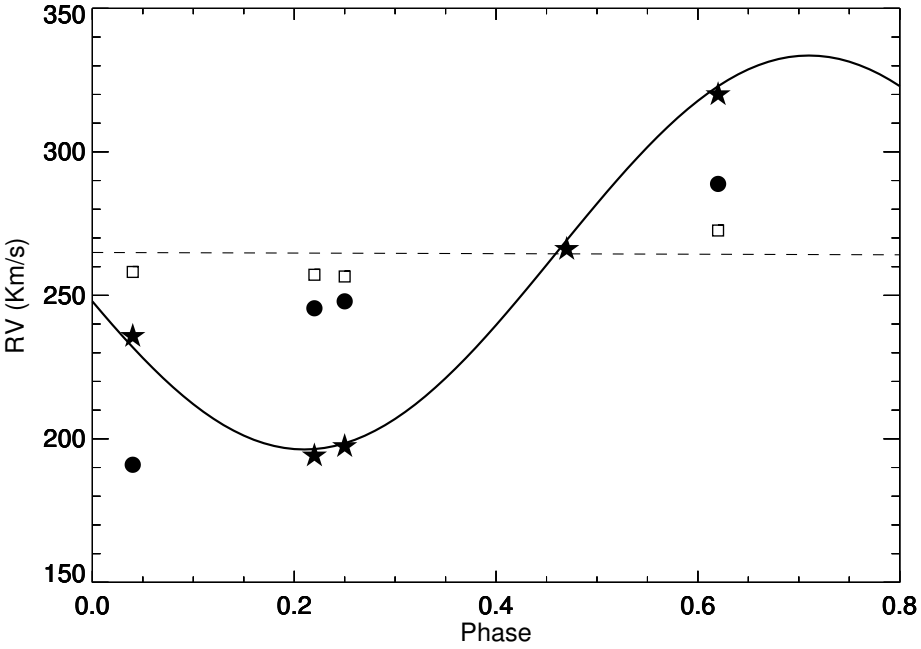

Figure 4.12: Radial velocities of Fe II lines at 5018 Å phased with a period 219.9 days and the best-fitting solution derived in Section 4.3.4. The horizontal dashed line marks the corresponding systemic velocity, star black points indicate the photospheric line velocity of the F-supergiant star, black points represent the velocity of the DACs and squares the velocities of narrow absorption components.

unblended lines (Fig. 4.13).

The abundances are calculated using suitable programs coupled with state-of-the-art atmospheric models (Sneden 1973; Kurucz 1993) using the LTE approximation, as usual in the abundance analysis of post-AGB stars (e.g. van Aarle et al. 2013). We used as input parameters the effective temperature and surface gravity derived from our light curve analysis (Section 4.4.2). Microturbulence velocity is obtained by removing any slope in the relation between the abundance from Fe I lines and the reduced EWs. Abundances for all the other elements are obtained from EW measurements. Usually cool stars show no evidence of significant rotation, so EWs are obtained from simple Gaussian fitting of spectral features. The NLTE effects should alter the ionization structure compared with the LTE model, but at the mild low metallicity and effective temperature of ELHC 10 this effect should be less than 0.1 dex for Fe I and 0.01 dex for Fe II (Mashonkina et al. 2011). In any case, the effective temperature derived by us comes from the comparison with the synthetic stellar spectra library, and does not depend on the LTE assumption.

The final abundance analysis of the ELHC 10 primary yields the parameters shown in Table 4.7, where Z is the proton number and N represents the number of lines used for the abundance determination of the species. The iron abundance [Fe I / H]= −0.38 is consistent with a star located in the low metallicity environment of the LMC.

The abundance pattern for the ELHC 10 primary is plotted in Fig. 4.14. The simple mean of the [X/Fe] ratio for the α-elements Si, S, Ca and Ti, is [α/Fe]= 0.40 ± 0.14, normal when compared with Galactic objects in this metallicity range, and consistent with the α-enhancement expected for LMC stars at their respective metallicities (Pompéia et al. 2008; Van der Swaelmen et al. 2013). In Fig. 4.14 we also compare the derived abundances of ELHC 10 with the abundances of J053253.51−695915.1, which is a post-AGB star confirmed in

Table 4.7: Abundances for ELHC 10. N represents the number of lines used for the abundance determination of the species. The uncertainties in $\log \epsilon$, $\log \epsilon_\odot$, [X/H] and [X/Fe] due to line to line scatter and model uncertainties were about 0.2 dex.

Species	N	$\log \epsilon$	$\log \epsilon_\odot$	[X/H]	[X/Fe]	Z
C I	2	8.72	8.52	0.20	0.58	6
Si I	1	7.56	7.55	0.01	0.39	14
S I	2	7.36	7.33	0.03	0.41	16
Ca I	3	6.19	6.36	-0.17	0.21	20
Sc II	2	2.97	3.17	-0.20	0.18	21
Ti II	2	5.19	5.02	0.17	0.55	22
Cr II	1	5.64	5.67	-0.03	0.35	24
Mn I	2	5.05	5.39	-0.34	0.04	25
Fe I	15	7.12	7.50	-0.38	...	26
Zn I	1	4.13	4.60	-0.47	-0.09	30
Y II	3	2.65	2.24	0.41	0.79	39
Zr II	1	2.73	2.60	0.13	0.51	40
Ba II	1	2.79	2.34	0.45	0.83	56
La II	1	1.67	1.26	0.41	0.79	57
Nd II	1	2.30	1.50	0.80	1.18	60
Eu II	1	1.03	0.51	0.52	0.90	63

the LMC (van Aarle et al. 2013). It is clear that the primary of ELHC 10 shows light s-process elements (magic neutron number 50) around Y and Zr which confirms the post-second dredge-up status of our star (van Winckel 2003).

As a by-product of our abundance analysis we calculated a microturbulence velocity of $\xi_t = 6.8 \pm 0.5$ km s^{-1} and an upper limit for the projected rotational velocity of 25 ± 5 km s^{-1}. The last figure comes from the width of the wings of the line profiles considering that a contribution of macro-turbulent velocity is also present.

4.4 Discussion

In this Section we calculate the system mass function using results of our radial velocity analysis and discuss the possible scenarios for the system that are compatible with the existing data.

4.4.1 On the nature of the primary star

Using the Stefan-Boltzmann law, the radius obtained from the SED fit and the spectroscopic temperature, the luminosity of the primary turns to be $L = 5970\,L_\odot$. Using $M_v = -4.7$ by de Wit et al. (2002) and neglecting the bolometric correction for a mid-F supergiant (Allen 2000) we get $L = 5970\,L_\odot$ and the previous figure is confirmed. We have compared the luminosity and temperature of the primary with the evolutionary tracks of single stars at metallicity $Z = 0.006$ provided by Georgy et al. (2013). The primary closely fits the model of an initially (and present) 8.1 $M_\odot$ star at an age of 3.18×10^7 yr but with a relatively large surface gravity $\log g = 1.79$ (Fig. 4.15). This high mass primary does not fit our results of a low mass and low surface gravity star inferred from the SED and the spectrum as given in Section 4.3.3.

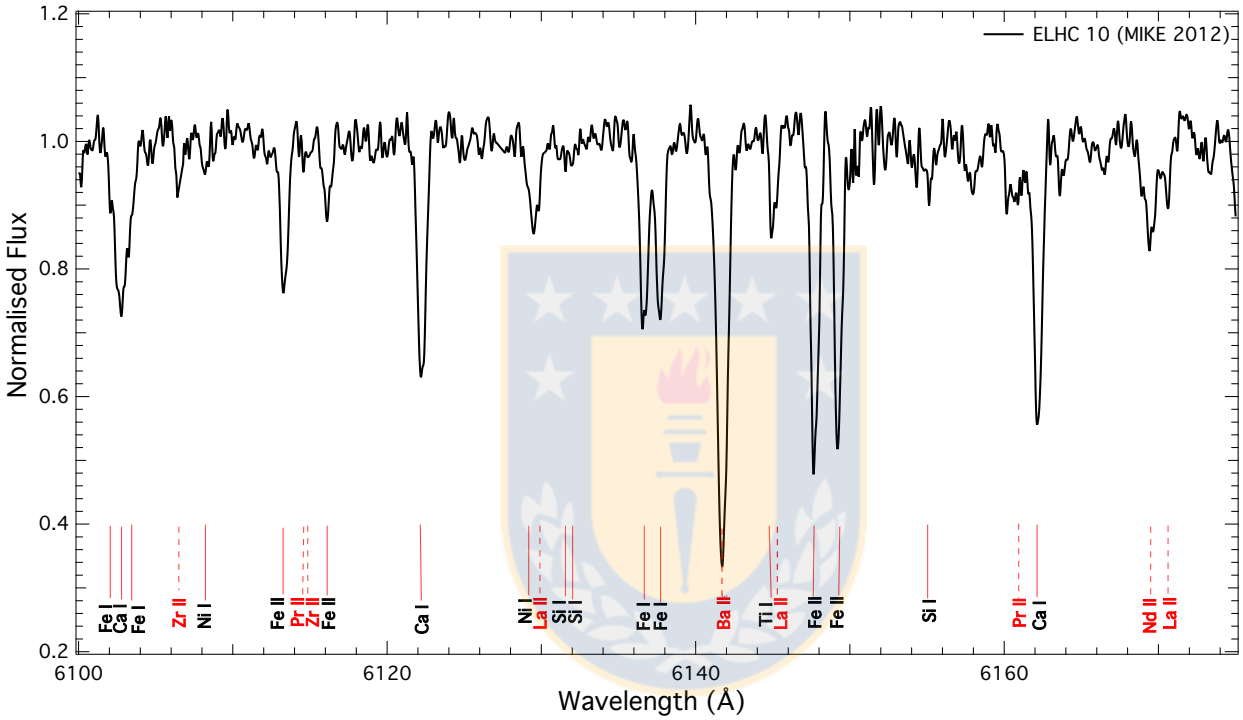

Figure 4.13: Complete line identification of this spectral region using the VALD database. Elements with atomic number Z smaller that 30 are indicated with a solid line, light s-process elements are indicated with a dashed line. This spectrum at phase $\Phi_o = 0.47$ was selected for abundance analysis due to the absence of DACs. It is shifted to match the laboratory wavelength of Ba II 6141.72 Å.

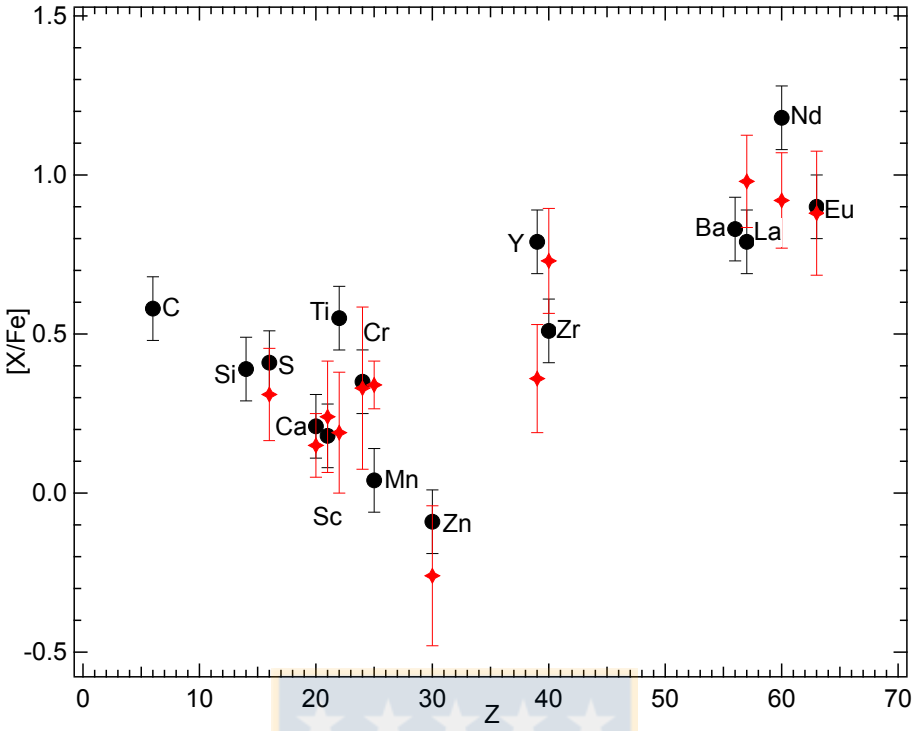

Figure 4.14: Derived abundance patterns for the primary of ELHC 10 (black points) in comparison with abundances for the same elements of the post-AGB star J053253.51−695915.1 (red points). Elements are labelled for clarity.

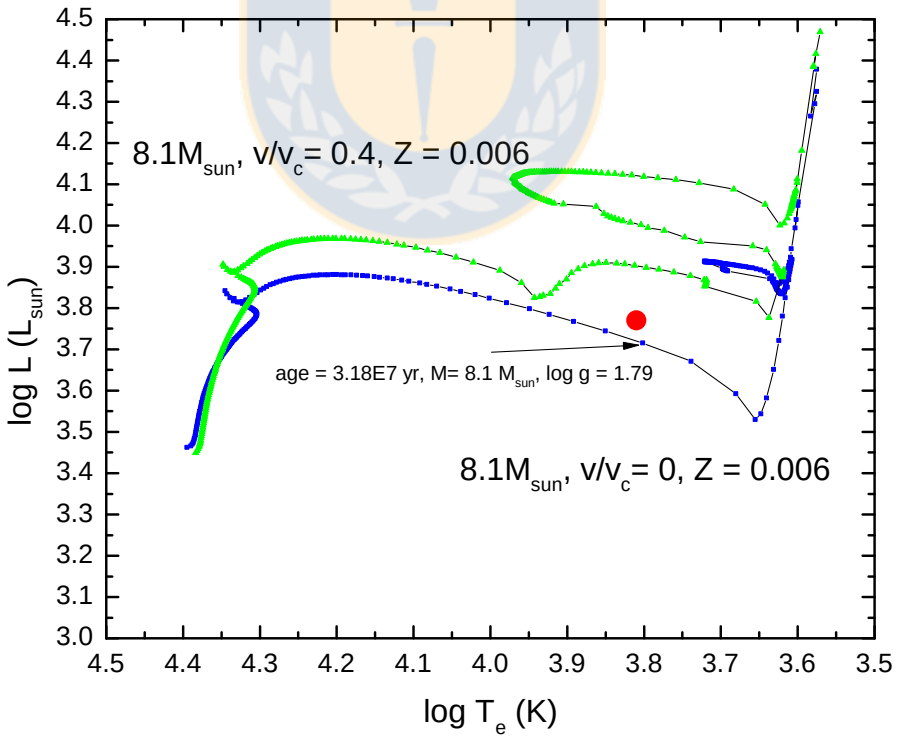

Figure 4.15: Position of ELHC 10 in the HR diagram. The location of ELHC 10 is shown with a red point in the diagram. The evolutionary tracks for single stars of initial mass 8.1 $M_{\odot}$ were taken from Georgy et al. (2013). We give the age, mass and surface gravity of the model closer to ELHC 10.

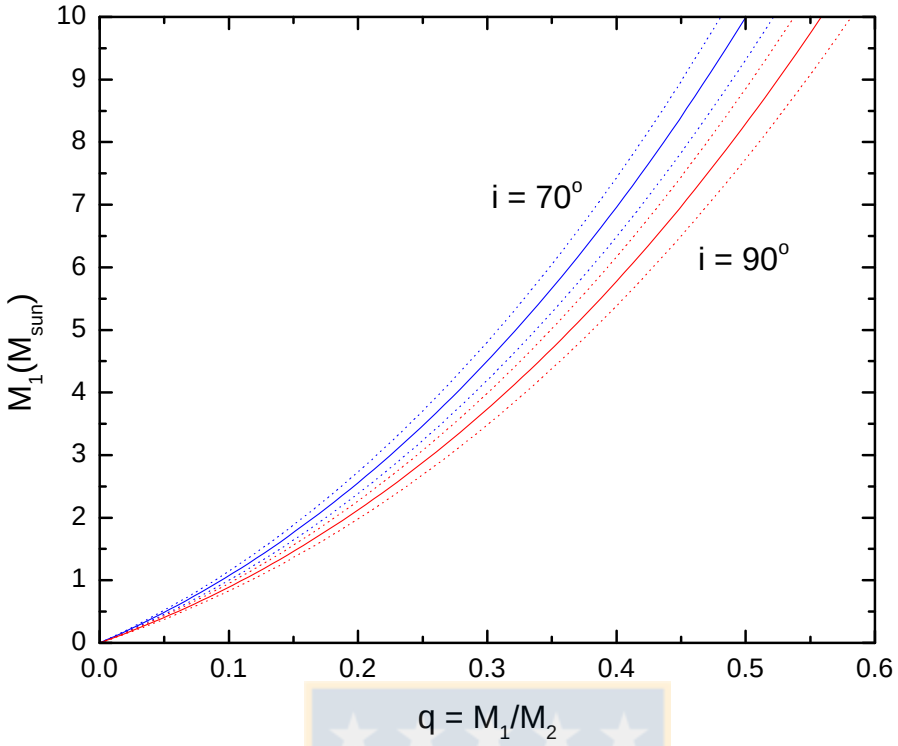

Figure 4.16: Primary mass versus mass ratio for different inclination angles according to the derived mass function. Dotted lines indicate the range due to the uncertainty in the mass function.

4.4.2 Constraints on the mass of the unseen secondary star and the semidetached case

We calculate the mass function $f(m)$ defined for a single-lined spectroscopic binary as (Hilditch 2001):

$$f(m) = \frac{M_1 sin^3 i}{q(1+q)^2} = 1.0361 \times 10^{-7} K_1^3 P \, \mathrm{M}_\odot, \tag{4.6}$$

where P is the orbital period in days, i is the inclination of the orbit and K_1 the primary radial velocity half-amplitude in km s^{-1}.

Assuming an eccentricity $e = 0$ and using our derived K_1 we get $f(m) = 7.37 \pm 0.55$ M$_\odot$. The possible masses for the secondary for a range of possible inclinations and primary masses, are shown in Fig. 4.16. It is clear that the secondary is always more massive that the primary. Since it is not detected either in the continuum or in the line spectrum probably it is hidden by the eclipsing structure.

Let's explore now the consequences of a possible semidetached configuration that should explain the existence of the eclipsing gray structure as a disc produced by mass transfer due to Roche-lobe overflow. Assuming that the primary fills its Roche lobe, their mean density should be constrained by the orbital period for $q \leq 0.8$ as (in our nomenclature $q = M_1/M_2$):

$$\bar{\rho} \approx 110 \, P_0^{-2} \mathrm{g \, cm^{-3}}, \tag{4.7}$$

where P_0 is the orbital period in hours (e.g. Frank et al. 2002). For ELHC 10 we find $\bar{\rho} = 3.9 \times 10^{-6}$ g cm^{-3}. Using this value, the radius derived in the previous section and assuming spherical symmetry we calculate a mass for the primary $M_1 \approx 0.625$ M$_\odot$. Surprisingly, this is very near the mass of a Post-AGB star with the observed luminosity. In fact, using the core mass versus luminosity relation for planetary nebula nuclei in the

horizontal part of the track by Vassiliadis & Wood (1994) we obtain 0.61 $M_\odot$, which roughly fits the low mass primary restriction derived in Section 4.3.2. With this mass we get a mass-ratio $q = 0.07$ (for $i = 90^o$) and a mass for the unseen secondary star $M_2 = 8.6\ M_\odot$, consisting of a main-sequence B2 V star.

4.4.3 Exploring the association with N120

The association with N120 yields interesting clues on the history of the system. N120 is a young association: the presence of H II regions and a SNR suggest an age of about 10 Myr (Laval et al. 1992). While it is true that this age is consistent with a main sequence B-type secondary, it is not consistent with the evolutionary stage of the low mass primary. There has not been enough time for the low mass primary to evolve to the observed supergiant stage. This is a strong argument to suspect that the primary has evolved from an initially higher mass star in an evolutionary channel strongly influenced by the presence of the binary companion. For instance, the primary could have lost significant amounts of matter by Roche lobe overflow during a semidetached stage as happens in Algols. This conjecture is consistent with the existence of massive post-AGB stars ($M \lesssim 8M_\odot$; Ventura et al. 2015). Since the amount of mass lost by the system during this process is impossible to know, we cannot reconstruct the history of the binary and the evolutionary track up to the progenitors.

We notice that the expected progenitor for a 0.62 $M_\odot$ post-AGB stars is 1.5 $M_\odot$ (De Smedt et al. 2012). It is impossible that this star has evolved to the current evolutionary stage as a single star if we assume the same age as the nebular complex N120.

4.4.4 Light curve modeling and system parameters

The irregular form of the main eclipse and the absence of spectral features of the secondary point to the existence of an accretion disc around it. This disc should be responsible for at least part of the infrared excess observed in the spectral energy distribution. In this section we develop the model for the light curve including the circumstellar disc plus the stellar components. We use subindexes h and c for parameters referring to the hot and cool star, respectively.

The fitting procedure

The light-curve fitting was performed using the Nelder-Mead simplex algorithm (see, e.g. Press et al. 1992) with optimizations described by Dennis et al. (1991), and the model of a binary system with a disc described in the Appendix A.

To obtain reliable estimates of the system parameters, a good practice is to restrict the number of free parameters by fixing some of them to values obtained from independent sources. We fixed the mass ratio to $q = 0.073$ and the stellar temperatures to $T_h = 20000$ K and $T_c = 6500$ K based on our spectroscopic results. The temperature of the hotter star (gainer), which is completely obscured by the accretion disc, was selected according to its estimated mass and the spectral type appropriate for a main sequence star of that mass, based on the tables of Lang (1992). To explore the sensitivity of our solution to the temperature of the gainer, we searched for the best solution with different values around $T_h = 20000$ K, and found that the solution is almost insensitive to the choice of the gainer temperature, which is to be expected since the gainer is totally hidden by the accretion disc.

In addition, we set the gravity darkening coefficients and the albedos of the gainer and the donor to $\beta_h = 0.25$, $\beta_c = 0.08$, and $A_h = 1.0$, $A_c = 0.5$ in accordance with von Zeipel's law for radiative envelopes (von Zeipel 1924) and complete re-radiation (Rafert & Twigg 1980) and (Lucy 1967) for the stars with convective

Table 4.8: Results of the analysis of ELHC 10 *BRI*-band light-curves obtained by solving the inverse problem for the Roche model with an large accretion disc completely obscuring the more-massive (hotter) gainer in critical non-synchronous rotation regime.

Quantity	B − band	R − band	I − band	Mean BRI
n	594	385	996	
$\Sigma(O-C)^2$	0.9589	0.7374	0.9743	
σ_{rms}	0.0402	0.0438	0.0313	
$q = \mathcal{M}_c/\mathcal{M}_h$	0.073	0.073	0.073	0.073
$i[^\circ]$	79.45	79.44	79.47	79.45 ± 0.4
F_d	0.723	0.722	0.729	0.725 ± 0.01
T_d[K]	2538	2403	2246	2400 ± 150
$d_e[a_{orb}]$	0.222	0.221	0.225	0.223 ± 0.002
$d_c[a_{orb}]$	0.139	0.142	0.141	0.141 ± 0.004
a_T	0.55	0.50	0.53	0.53 ± 0.03
F_h	1.000	1.000	1.000	1.000
T_h[K]	20000	20000	20000	20000
T_c[K]	6500	6500	6500	6500
$A_{hs} = T_{hs}/T_d$	1.88	1.81	1.87	1.85 ± 0.04
$\theta_{hs}[^\circ]$	19.6	18.4	16.8	18.3 ± 1.5
$\lambda_{hs}[^\circ]$	317.4	316.6	316.3	316.8 ± 0.6
$\theta_{rad}[^\circ]$	15.0	12.9	14.2	14.0 ± 1.1
$A_{bs1} = T_{bs1}/T_d$	1.88	1.83	1.86	1.86 ± 0.04
$\theta_{bs1}[^\circ]$	48.7	48.1	47.3	48.0 ± 0.7
$\lambda_{bs1}[^\circ]$	176.9	174.4	179.1	176.8 ± 2.4
$A_{bs2} = T_{bs2}/T_d$	1.70	1.71	1.60	1.67 ± 0.07
$\theta_{bs2}[^\circ]$	33.0	23.2	34.9	30.4 ± 7.2
$\lambda_{bs2}[^\circ]$	30.6	25.2	32.5	29.4 ± 4.2
Ω_h	57.72	57.72	57.72	57.72
Ω_c	1.872	1.872	1.872	1.872
$\mathcal{M}_h[\mathcal{M}_\odot]$	8.5	8.5	8.5	8.5 ± 0.1
$\mathcal{M}_c[\mathcal{M}_\odot]$	0.62	0.62	0.62	0.62 ± 0.01
$\mathcal{R}_h[R_\odot]$	6.8	6.8	6.8	6.8 ± 0.1
$\mathcal{R}_c[R_\odot]$	59.9	59.9	59.9	59.9 ± 0.1
$\log g_h$	3.7	3.7	3.7	3.7 ± 0.1
$\log g_c$	0.68	0.68	0.68	0.7 ± 0.1
M^h_{bol}	−4.76	−4.76	−4.76	−4.8 ± 0.1
M^c_{bol}	−4.61	−4.61	−4.61	−4.6 ± 0.1
$a_{orb}[R_\odot]$	320	320	320	320 ± 5
$\mathcal{R}_d[R_\odot]$	144.6	144.3	145.8	144.9 ± 1.0
$d_e[R_\odot]$	71.0	70.8	72.0	71.3 ± 0.7
$d_c[R_\odot]$	44.5	45.5	45.1	45.0 ± 0.5

FIXED PARAMETERS: $q = \mathcal{M}_c/\mathcal{M}_h = 0.073$ - mass ratio of the components, T_h = 20000K - temperature of the more-massive (hotter) gainer, $T_c = 6500K$ - temperature of the less-massive (cooler) donor, $F_c = 1.0$ - filling factor for the critical Roche lobe of the donor, $f_h = 230; f_c = 1.00$ - non-synchronous rotation coefficients of the gainer and donor respectively, $\beta_h = 0.25; \beta_c = 0.08$ - gravity-darkening coefficients of the gainer and donor, $A_h = 1.0; A_c = 0.5$ - albedo coefficients of the gainer and donor.

Quantities: n - number of observations, $\Sigma(O-C)^2$ - final sum of squares of residuals between observed (LCO) and synthetic (LCC) light-curves, σ_{rms} - root-mean-square of the residuals, , $q = \mathcal{M}_c/\mathcal{M}_h$ - mass ratio of the components, i - orbit inclination (in arc degrees), $F_d = R_d/R_{yc}$ - disc dimension factor (ratio of the disc radius to the critical Roche lobe radius along y-axis), T_d - disc-edge temperature, d_e, d_c, - disc thicknesses (at the edge and at the center of the disc, respectively) in the units of the distance between the components, a_T - disc temperature distribution coefficient, $F_h = R_h/R_{zc}$ - filling factor for the critical Roche lobe of the hotter, more-massive gainer (ratio of the stellar polar radius to the critical Roche lobe radius along z-axis), $A_{hs,bs1,bs2} = T_{hs,bs1,bs2}/T_d$ - hot and bright spots' temperature coefficients, $\theta_{hs,bs1,bs2}$ and $\lambda_{hs,bs1,bs2}$ - spots' angular dimensions and longitudes (in arc degrees), θ_{rad} - angle between the line perpendicular to the local disc edge surface and the direction of the hot-spot maximum radiation, $\Omega_{h,c}$ - dimensionless surface potentials of the hotter gainer and cooler donor, $\mathcal{M}_{h,c}[\mathcal{M}_\odot]$, $\mathcal{R}_{h,c}[R_\odot]$ - stellar masses and mean radii of stars in solar units, $\log g_{h,c}$ - logarithm (base 10) of the system components effective gravity, $M^{h,c}_{bol}$ - absolute stellar bolometric magnitudes, a_{orb} $[R_\odot]$, $\mathcal{R}_d[R_\odot]$, $d_e[R_\odot]$, $d_c[R_\odot]$ - orbital semi-major axis, disc radius and disc thicknesses at its edge and center, respectively, given in the solar radius units.

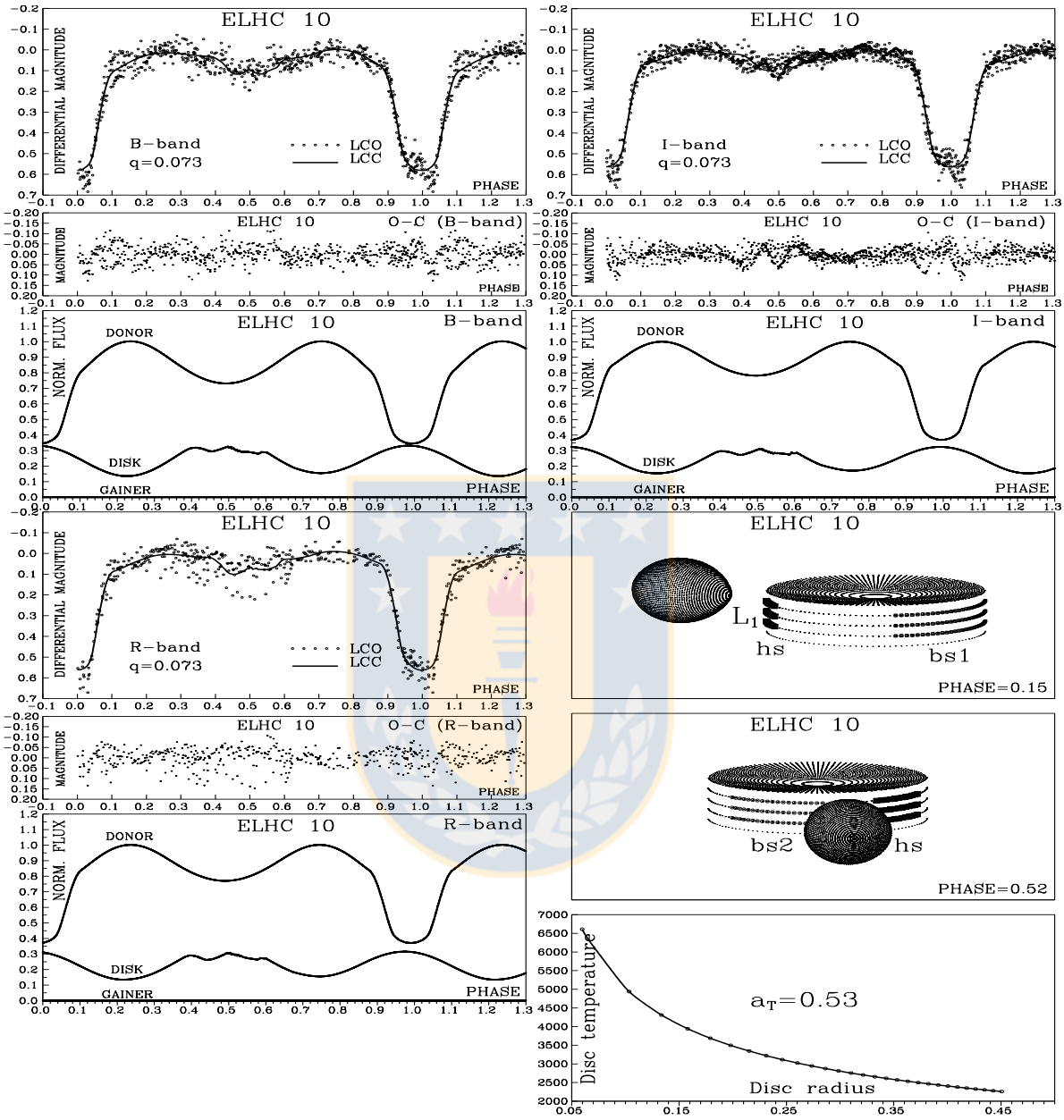

Figure 4.17: Observed (LCO) and synthetic (LCC) light-curves of the system ELHC 10 obtained by analyzing *BRI*-band photometric observations; final O-C residuals between the observed and optimum synthetic light curves; fluxes of donor, gainer and of the accretion disc, normalized to the donor flux at phase 0.25; the views of the optimal model at orbital phases 0.15 and 0.52, obtained with parameters estimated by the light curve analysis and the accretion disc temperature distribution along the disc radius.

envelopes. The limb-darkening for the components was calculated in the way described by Djurašević et al. (2010).

The possible values of free parameters are constrained by imposing the lowest and highest values which seem reasonable based on the previous studies of this binary. Here are the ranges for the fitted parameters: inclination: 70.0 to 90.0 degrees; disc dimension factor (the ratio of the disc radius and the radius of the critical Roche lobe along the y-axis): 0.5 to 0.9; disc edge temperature: 2500 to 5000 K; disc edge thickness: 0.1 to 0.3 (in units of a_{orb}); disc center thickness: 0.01 to 0.15 (in units of a_{orb}); the exponent of the disc temperature distribution: 0.1 to 0.75. After the first fit, these ranges were decreased according to the results of the first iteration.

Our code treats the rotation of the donor as synchronous ($f_c = 1.0$) and assumes that the donor has filled its Roche lobe (i.e. the filling factor of the donor was set to $F_c = 1.0$). It is expected that the accreted material from the disc would transfer enough angular momentum to increase the rotation rate of the gainer to the critical velocity (Packet 1981; de Mink et al. 2007). In our study a proper estimation of the gainer's non-synchronous rotation parameter is not possible, because it is completely hidden by the accretion disc. Given this situation, we looked for a non-synchronous rotation parameter for the gainer that would make its effective radius fall in the critical rotation regime equal to the radius expected in a main sequence star with the gainer's mass, and according to the tables of Lang (1992). This procedure suggests that a reasonable value for the non-synchronous rotation parameter would be $f_h = 230$, which would make a star of 8.5 solar masses have an effective radius of 6.8 solar radii. Although it might seem that this value is extremely large, it should be noted that, given the orbital period of 219 days, it results in a rotation rate that is typical for B stars. In any case, the adopted value of the non-synchronous rotation parameter for the gainer doesn't affect the other parameters of the model in a significant way, since the star is enveloped by the accretion disc and does not contribute to the total flux of the system.

A preliminary analysis of the observations showed that a hot spot region indeed improved the fit but could not explain the light-curve asymmetry completely. By introducing two additional bright spots (bs1 and bs2), larger than the hot spot and located on the disc edge at nearly the opposite sides of the disc ($\lambda_{bs1} \approx 177°$ and $\lambda_{bs2} \approx 29°$), the fit become much better. The longitude λ is measured clockwise (as viewed from the direction of the +Z-axis, which is orthogonal to the orbital plane) with respect to the line connecting the star centers (+X-axis), in the range $0° - 360°$.

The bright spots in the model attempt to approximate the spiral structure of the disc, predicted by hydrodynamical calculations (Heemskerk 1994). The tidal force exerted by the donor star causes a spiral shock, producing one or two extended spiral arms in the outer part of the disc. The bright spot at $\lambda_{bs1} \sim 177°$ can also be interpreted as a region where the disc significantly deviates from circular shape. Moreover, this is a region where we can expect loss of matter from the gas stream and the disc through the L_3 Lagrangian point, forming some kind of a circumbinary shell. Inhomogeneities in such a structure would affect the radiation of the system, and could explain the variations in total light.

The optimal model of ELHC 10 has the inclination angle well constrained to $i \sim 79°$, and contains a thick accretion disc around the hotter, more massive component. With a radius of $R_d \sim 150\ R_\odot$, the disc is more than twenty times larger than the central star, whose radius is $R_h \sim 6.8\ R_\odot$. The disc is of notably concave shape, with central thickness of $d_c \sim 45\ R_\odot$ and the thickness at the edge of $d_e \sim 71\ R_\odot$. The temperature of the disc increases from $T_d = 2400$ K at its edge, to ~ 12100 K at the center, according to Eq. A.1, with the temperature profile exponent of $a_T \sim 0.53$. The effective temperature of the disc is significantly higher than the temperature at its edge.

We modeled the asymmetry of the light curve very well by incorporating three regions of enhanced radiation

on the accretion disc: the hot spot (hs), and two bright spots (bs1 and bs2). The hot spot (hs) is situated at longitude $\lambda_{hs} \sim 317°$, roughly between the components of the system, at the place where the gas stream falls onto the disc. The temperature of the hot spot is approximately 85% higher then the disc edge temperature ($T_d \sim 2400$ K), i.e. $T_{hs} \sim 4440$K.

However, to achieve a good fit of the model to the observations, it was necessary to include two bright spots in the model too. The first bright spot (bs1), representing the first spiral arm of the disc, is located on the disc edge at nearly the opposite side from the hot spot ($\lambda_{bs1} \sim 177°$), and is of larger size than the hot-spot. The second bright spot (bs2) is located at longitude $\lambda_{bs2} \sim 29°$ and has a temperature of about 67% higher then the disc edge temperature. It can be interpreted as the second spiral arm in the disc. Note that the active regions on the accretion disc are located in such a way that might also be interpreted as outflow of matter through the Lagrangian points L_2 and L_3.

The achieved fit of our model light-curves (LCC) to the observations (LCO) is shown in Fig. 4.17, which also shows the O-C residuals and the individual synthetic fluxes of the components (donor, gainer, disc) normalized to the donor brightness at orbital phase 0.25. The main contribution comes from the donor, because the more massive gainer star is completely obscured by the large accretion disc. The disc contributes approximately 15% of the donor flux at maximum light. The appearance of ELHC 10 in orbital phases 0.15 and 0.52 is illustrated in Fig. 4.17, with the phases chosen so as to show the components and the bright spots on the disc. The parameters of the optimal model are listed in Table 4.8. Small differences are found between the solutions for the individual B, R and I passband light curves, and we adopt the mean *BRI* solution as the representative one.

The values obtained, especially the masses and radii, are consistent with the figures estimated in previous sections. Only the primary surface gravity ($\log g = 0.7 \pm 0.1$) is smaller than the spectroscopic value ($\log g = 2.0 \pm 0.5$) probably due to the coarse grid used in the analysis. The lower g is more significant since it is consistent with the primary mass and radius. We notice that the disc temperature, higher than sublimation temperatures, is compatible with a gas disc rather than a dusty disc.

Variations in the shape of the light curves around the secondary minimum indicate that the accretion disc parameters (e.g. radius, temperature), the gas flow (hot line), and the active regions (bright spots related to the spiral arms or/and the disc shape deviation from the simple cylindric approximation), are continuously changing, probably because of fluctuations in the outflow from the donor. This is especially evident in the I-band curve.

Whereas a disc flux contribution of 15% at maximum light in optical wavelengths is more or less consistent with our earlier results of a small disc contribution to the SED model and absence of significant veiling in the primary lines, we notice that during main eclipse the disc flux contribution increases to $\sim 50\%$. At this phase the spectral lines of the primary do not weaken (Fig. 4.11). This fact does not have a trivial explanation, but we speculate that during eclipse part of the disc superior atmosphere could act like a pseudo photosphere near the primary, increasing the optical depth and the line strength.

On the other hand, our light curve model cannot discriminate between an accretion powered disc or a disc heated by the secondary. However, if the disc is accretion powered, its luminosity of about 15% the primary luminosity implies a mass accretion rate of 4.2×10^{-5} $M_\odot$ yr^{-1}, according to standard formulae of steady-state accretion discs (Frank et al. 2002).

4.4.5 Hα emission and circumbinary disc

Hα is the most intense line in the spectra and shows a double-peak emission, broad wings extending from 6557 to 6582 Å and a mean separation of the blue and red peak of ≈ 115 km s^{-1} with the blue peak approximately

Table 4.9: Hα equivalent widths, intensities of the blue and red emission peaks normalized to the underlying continuum, intensity of the central depression, RV of the overall profile, peak separation, full width at half-maximum and circumstellar reddening caused by the Hα emitting envelope (Dachs et al. 1988).

Phase	Instrument	-EW (Å)	$I_V/I_{Cont.}$	$I_R/I_{Cont.}$	$I_C/I_{Cont.}$	RV_{mean} (km s^{-1})	ΔV_{peak} (km s^{-1})	FWHM (km s^{-1})	$E^{CE}_{(B-V)}$ (mag)
0.04	HARPS (2014)	25.5	6.19	5.91	0.42	260	112	304	0.05
0.22	HARPS (2010)	26.0	4.31	4.24	0.33	260	118	269	0.05
0.25	HARPS (2013)	22.8	5.07	5.04	0.45	259	114	244	0.05
0.47	MIKE (2012)	24.5	6.03	6.30	0.29	260	112	247	0.05
0.62	ECHELLE (2010)	21.3	3.98	4.34	0.19	262	110	234	0.04

equal to the red peak. The Hα emission is characterized by several parameters whose values are given in Table 4.9. The strong Hα double-peak emission is consistent with the presence of an emitting disc. The central absorption component in the Hα profile remains with the same radial velocity in spite of changes in the radial velocity of the primary over the years (see Fig. 4.18 and Table 4.9). The same occurs for the position of the violet and red emission peaks. The velocity of the central core is -5 ± 1 km s^{-1}, blue shifted from the systemic velocity, i.e. at velocity 260 km s^{-1}. The constancy of this velocity is possible if (i) the disc is around a star considerably more massive than the primary, therefore it performs small (undetected) motions around the system center of mass or (ii) most of the emission comes from a slowly expanding circumbinary disc extending beyond the binary to considerable distances, producing a column density large enough to produce the almost stationary Hα central absorption. In the following we give arguments favoring this last possibility.

Emission from a circumbinary disc is consistent with the fact that the velocity of the Hα central absorption is practically the same as the velocity of the nebular complex N 120 C4 and C5 that are close to our star; viz. 260 km s^{-1} (Section 4.2.2). It is also consistent with the detection of stationary N II 6548, 6583 Å forbidden emission lines, which are commonly attributed to low density material in the circumstellar environment. It is possible that the Hα emitting disc extends into the interstellar medium to zones of low density where forbidden emission lines are produced. The circumbinary disc should be optically thin, to explain the steep Balmer emission decrement, and contribute with free-free emission to the system at infrared wavelengths (Fig. 4.5). In addition, the large Hα central absorption indicates strong self-absorption, this is possible if the disc is coplanar (or almost coplanar) with the binary.

In Section 4.4.2 we get a binary orbital separation of $320\,R_\odot$, i.e. about $5.3\,R_1$. If the Hα emission is produced in a Keplerian disc then the half-peak separation ($V_k \sin i$) gives the keplerian velocity at a representative radius r given by:

$$r = \frac{GM}{V_k^2}. \tag{4.8}$$

Using a total mass of 9.1 $M_\odot$ (Section 4.4.2) and $V_k \sin i = 56.6$ km s^{-1} we get:

$$r = 541\,R_\odot \sin^2 i. \tag{4.9}$$

For an inclination of 79 degree (Section 4.4.2) we get a disc radius of $8.7\,R_1$ i.e. 1.6 times the orbital separation. Since the mass of the primary is relatively low, the disc radius does not change assuming the orbit only around the secondary star in the previous calculation. Based on this result, we conclude that the double-peaked emission in Hα originates from material orbiting in a circumbinary disc.

The presence of emission at the Hα profile wings with high projected velocities suggests that the inner disc

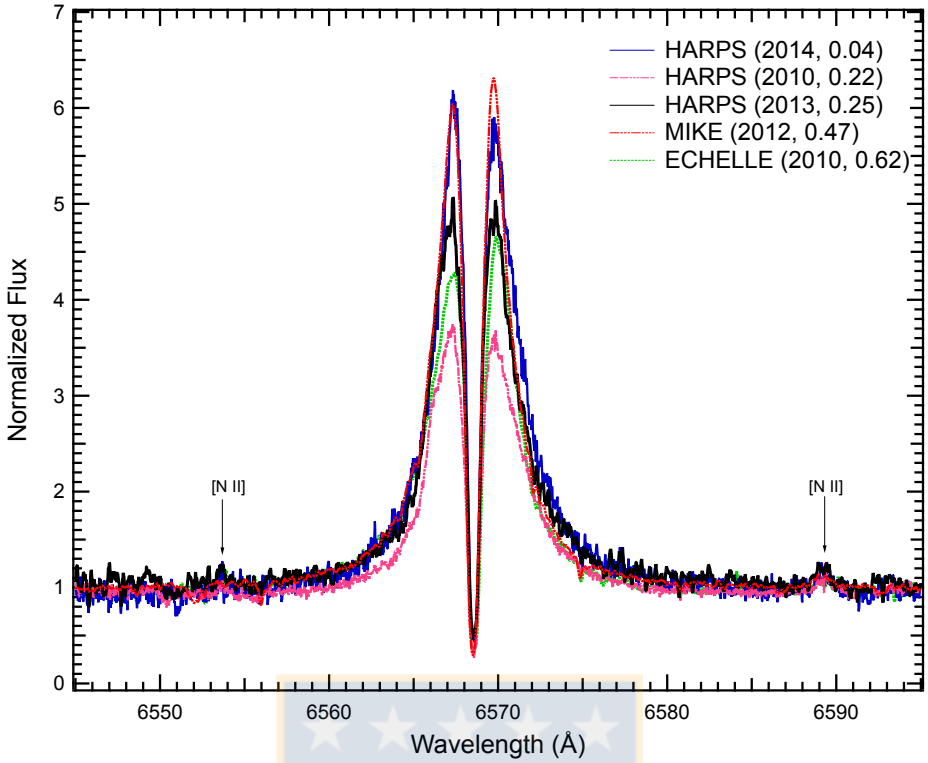

Figure 4.18: The HARPS (2010, 2013, 2014), MIKE (2012) and ECHELLE (2010) spectra showing Hα profile and N II emission lines. Fluxes are normalized to the continuum and heliocentric corrections have been applied.

rim extends inside the binary. In fact, using Eq. 4.8 with $V_k \sin i = 300$ km s^{-1} we obtain a disc inner radius of about 16 $R_\odot$, well inside the binary system. However, in this case the profile emission wings should show the orbital motion and this is not observed. This is possible if the disc is not Keplerian, but significant amounts of angular momentum are being supplied at the inner boundary from the binary through equatorial outflows (discussed in Section 4.5) causing super-Keplerian velocities. The blue-shifted Hα absorption core supports this view of an outflowing disc. In this case the disc extension should be larger than predicted by Eq. 4.9, as expected from the presence of forbidden emission lines. We notice that electron scattering might also explain the broad emission wings (Poeckert & Marlborough 1979). Since it is very hard to measure radial velocities for the broad wings with the needed accuracy, we cannot discard this interpretation.

The circumbinary disc analyzed in this section is different from the circumstellar disc included in the light curve model. A limitation of our light curve model is that it does not include the contribution of the circumbinary disc nor gas streams. However, the Balmer emission decrement suggests that the circumbinary disc is optically thin and therefore its contribution at the continuum should be minor compared with light sources considered in the model. The relatively good fit obtained supports this view. Coexistent circumstellar and circumbinary discs have been also found in other post-AGB binaries (Gorlova et al. 2012, 2015; Hillen et al. 2013, 2014, 2015).

4.4.6 Line splitting, binary interaction and mass loss

Line splitting is a very particular property of ELHC 10. It is observed in metallic lines, especially lines of Fe I, Fe II and Ti II, but disappears near secondary minimum at $\Phi_o = 0.47$. Line splitting are not observed in Ba II, Ca I, Mg II and Si II lines except during main eclipse at phase $\Phi_o = 0.04$ (at least Ba II and Si II that are

spectrally covered at this phase). Line splitting occurs in the form of DACs displaced to the red or blue side of the photospheric line. In this section we offer a possible explanation for this phenomenon. Since the number of available spectra is limited, our picture is still speculative, but it can be tested and developed further in case new observations become available.

Line splitting has been observed in lines of heavy elements in post-AGB stars with C-rich circumstellar environments and explained by structured atmospheres (Klochkova 2015). For instance, in V 5112 Sgr the Ba II line profiles are split in multiple components (Klochkova 2013). The case of ELHC 10 is different, since its primary is not carbon-rich and the alternated visibility of DACs during the orbital cycle exclude any interpretation in terms of an structured envelope. In fact, lines formed in a structured envelope around the primary should follow the primary motion during the orbital cycle with a blue velocity shift, but not move from the red to the blue side of a line formed in the photosphere. In addition, we do not observe DACs in ELHC 10 only in s-process elements, as in V 5112 Sgr, but also in metallic lines of light elements.

In ELHC 10 DACs are probably formed by occultation of the primary photosphere by dense and extended gas regions co-rotating with the binary. This view is supported by the fact that they are not observed around secondary eclipse (Φ = 0.47 and 0.54). The problem is trying to figure out how these regions are distributed in the binary system. Is there evidence of gas streams physically connected with the accretion disc? The existence of a disc hot spot could indicate that a gas stream coming from L_1 hits the disc, as usual in other semidetached binaries. This gas stream faces the observer after main eclipse, potentially explaining the BAC observed at Φ = 0.04. However, at Φ = 0.22 and 0.25, i.e. near first quadrature, we observe RACs, suggesting the presence of material that is falling down onto the primary. Has this material bounced back from the stream-disc impact region? At present it is not clear. Then after secondary eclipse, at Φ = 0.62, BACs are observed, possibly associated with outflow from the disc bright spot bs2 or eventually with mass loss through the L_2 point, or both. On the other hand, the disc bright spot bs1 could be associated with material escaping through the L_3 point. Alternatively, the BAC observed during main eclipse could also be explained by this stream. Mass loss through L_2 and L_3 could feed the Hα emitting circumbinary disc. This is consistent with Na D and Si II absorptions seen almost at the same velocity as the system centre of mass. Furthermore, systemic mass loss is consistent with the small expansion velocity detected in the circumbinary disc suggesting that material of high angular momentum is being supplied at their inner boundary. The final clarification of the gas flows in this binary will require a denser set of high resolution spectra than available at present.

In this context we notice that line splitting has been observed in the He I 5875 Å line of the interacting binary HD 170582 (Mennickent et al. 2015), and interpreted as evidence of absorption by a gas flow near L_1. Evidence for interaction has also been observed in the Galactic post-AGB star BD+46^o 442, an evolved binary with gas streams, jets and disc (Gorlova et al. 2012). Contrary to ELHC 10, this last system shows strong orbital variability at the Hα emission; this line has been interpreted as formed in the disc around the secondary and the Hα blue-shifted absorption in terms of a disc jet (Gorlova et al. 2012).

4.5 Conclusion

70 high probability and 1337 candidate post-AGB LMC stars have been catalogued by van Aarle et al. (2011). About half of them are probably binaries, a distinction made based on the shape of the spectral energy distribution, indicating a stable and likely Keplerian disc. This is a surprising result, since one could expect that the residual material from the AGB mass loss should be found in an expanding envelope. Therefore, it has been suggested that the formation of a circumbinary disc plays a major role in the evolution of post-AGB systems (Van Winckel 2007). Very few of these binaries have been studied in detail. To our knowledge, ELHC 10

could be the first post-AGB binary identified in the Large Magellanic Cloud, and the post-AGB binary with the highest progenitor mass and the highest companion mass known.

We have found convincing evidence that ELHC 10 is a semi-detached long-period binary system consisting of a post-AGB star and an unseen, unevolved B-type companion surrounded by a large and geometrically thick disc. A critical point in our view is the assumption that the primary follows the core-mass versus luminosity relationship for post-AGB stars; this allows us to infer the primary mass from the observed luminosity. We support this assumption based on the following points: (i) the abundance pattern of ELHC 10 is similar to that shown by other post-AGB systems, (ii) the primary luminosity is low for identifying it with a more massive yellow supergiant, nor do we find P-Cygni profiles or pulsations typical of this class of objects and (iii) a more massive primary, along with the system mass function, should imply a too luminous secondary, which is discarded due to its non-detection in the spectrum. Besides that, the assumed primary mass and derived radius nicely fit the requirement of a semidetached binary that is consistent with the evidence of stellar interaction. The very likely membership to the young nebular complex N120 suggests that the only way for the primary to have arrived to the observed advanced evolutionary stage is from an initially much more massive star. Significant mass loss could have occurred recently by mass transfer due to Roche lobe overflow in a semidetached binary. Since the amount of mass lost by the system during this process is impossible to know, we cannot reconstruct the history of the binary and the evolutionary track up to the progenitors. In our model the whole system is surrounded by a circumbinary gas disc, which is revealed by a prominent stationary Hα double emission line. Our determined system parameters are given in Table 4.8.

The post-AGB star of ELHC 10 has a mass of 0.62 $M_\odot$ and radius 59.9 $R_\odot$, and is the more evolved star in the system. This implies that once it was the more massive star of the binary pair and subsequently experienced substantial mass loss probably by Roche lobe overflow onto the secondary as happens in Algols. The accretion disc and the circumbinary disc can be residuals of the earlier or present evolution of the progenitor. Therefore, it is posible that their evolution has not been typical for a single isolated star of the same temperature and luminosity, since in this case the progenitor is expected to be of about only 1.5 $M_\odot$. Actually, we have found evidence that the systems is in a semi-detached stage with the primary transferring mass onto the secondary through an accretion disc. Evidence for gas streams connecting the binary with the circumbinary disc have also been found. The above suggests that a low-mass post-AGB star can be formed in a different way that a single post-AGB star, which posses a solar-mass progenitor. In fact, our study shows that a low-mass post-AGB star can also be formed from a massive post-AGB star (e.g. Ventura et al. 2015) that subsequently suffers mass transfer in a binary system.

We fit the *BRI*-band photometric observations using a model including a geometrically and optically thick accretion disc. The accretion disc in our model is of concave shape and extends to roughly 70% of the critical Roche lobe for the gainer. The asymmetry of the light curve is successfully modeled by incorporating three active regions on the accretion disc: a hot spot (hs), and two bright spots (bs1 and bs2), which in turn represent the “hot line" and two spiral arms of the disc, the deviations of the disc from a circular shape, or the outflow of matter from the system through Lagrangian points L_2 and L_3. Properties of the disc are given in Table 4.8. We have no way to estimate the disc mass, but it likely contains a fraction of the mass lost by the donor during earlier evolutionary stages.

We discovered line splitting of metallic lines in ELHC 10, characterized by discrete absorption components observed alternatively at the blue and red side of the photospheric line profiles during the orbital cycle. These DACs are similar in appearance to those observed in carbon-rich post-AGB stars (Klochkova 2015), but cannot be interpreted easily as evidence for structured atmosphere as done by this author for carbon-rich post-AGB systems. On the contrary, DACs observed in ELHC 10, can be interpreted as evidence for gas streams; one

carrying material from the primary onto the circumstellar disc and others bringing material from the system into the circumbinary disc. This view is independently corroborated by the bright and hot spots found in the disc through the light curve analysis. This scenario is consistent with the evidence for a slowly expanding circumbinary disc derived from the blue-shifted Hα central absorption and the detection of narrow blue-shifted stationary absorption lines. Notoriously, Ba II and Si II lines do not show DACs except during main eclipse, when the observer faces the gas stream from the donor star. As this stream brings the chemical signature of the primary, whereas others streams bring material with disc chemical composition, this fact could indicate a different chemical enrichment in donor and disc, something possible if the donor has experienced recently important chemical changes. On the other hand, the strength of DACs, sometimes comparable to the strength of photospheric lines, implies that large amounts of material are being transferred in the streams.

Our study provides evidence that circumbinary discs in post-AGB stars can be formed by binary star interaction and outflows through the outer Lagrangian points. This is a very important insight, since hitherto the process of disc formation in post-AGB stars has remainned obscure. For instance, (Livio & Soker 1988) and Sandquist et al. (1998) showed that the disc can be the result of the AGB evolution after engulfing the companion with a common envelope. Another scenario proposes a disc-like structure formed by wind accretion (Mastrodemos & Morris 1999). Finally, the disc can be the result of interaction between the AGB wind and the disc jet (Akashi & Soker 2008). While these scenarios can be possible at some evolutionary stage, the current observations of ELHC 10 favour equatorial mass loss through the outer Lagrangian points as the mechanism of circumbinary disc formation. This is consistent with Roche-lobe overflow and the presence of a large and thick disc surrounding the secondary star. The kind of outflows that possibly explain the DACs have been predicted by hydrodynamical simulations of gas dynamics in close interacting binaries (Bisikalo et al. 2003; Sytov et al. 2007).

Chapter 5

Concluding remarks

The main objective of this thesis was to provide some clues into of the star formation process and cluster evolution in the LMC and additional to this, determine whether there is any metallicity effects on the star formation process. To this end, we used the instrument Wide Field Imager (WFI) in its slitless spectroscopic mode in order to identify the Hα emission-line objects (from low to high mass, not evolved to evolved) in the LMC star-formation region NGC 1850 and its surrounding field. Thus, the spatial localization of the various populations of our sample has also been studied with this field centered on the cluster NGC 1850, in particular for the emission-line stars, the young stars, and the evolved giant star populations.
On the other hand, we give important clues about the mass-loss and mass-transfer process in the DPV stars and post-AGB stars and as a consequence, we established that binary interaction and mass outflows can be invoked as the general cause for the circumbinary discs detected in post-AGB stars and the absence of orbital-period change in DPV systems.

The conclusions on each of the individual case studies are already summarized at the end of each Chapter, and therefore we would like to give the general impression of our work and most unbiased overall conclusion of each part.

In the first part of this thesis work, we used WFI slitless Hα spectroscopy in order to find emission-line objects in the LMC cluster NGC 1850. Sixty-four emission-line stars were found and classified using different methods. Cross-correlation with the OGLE and MACHO database allowed us to associate these emission-line objects with homogeneous photometric data, allowing us identify the evolutionary stage of the objects.
From this reliable stellar classification of the stars in the LMC NGC 1850 region, we studied their spatial and stellar evolution properties and their different populations. We found that at least two different events of triggered star formation have occurred in the NGC 1850 cluster.
The star formation history of NGC 1850 is very complex and requires large-scale triggering mechanisms such as shocks and compression of the associated H II region due to expanding of supergiant shells surrounding older OB associations. The observations suggest that the star-formation has taken place as a sequential process in the border of the shell and in its local background. This feature is characterized in the cluster by a high concentration of emission-line stars and young stellar objects found by us using Hα slitless spectroscopy, which is encompassed in the border of the shell.

In the second part of this thesis work, we have focused on a deep analysis of the physical properties and evolutionary route of the first DPV system studied in detail in the LMC from its photometric and spectroscopic

characteristics. Our main results of this part of the work can be summarized as follows:

The analysis of high-resolution spectra together with the application of a sophisticated light curve model has allowed us to derive orbital parameters and physical properties such as stellar masses, radii, luminosities and the effective temperatures for the first DPV system studied definitively in the LMC. The best fit to the orbital light curve requires a non-stellar component that was modelled with a geometrically thin and optically thick disc model. Moreover, the stability of the orbital light curve suggest that the stellar plus disc configuration remain stable during the long cycle. Therefore, the variability of the optically thick disc is not the main source for the long cycle. This scenario is consistent with the results found in four other DPVs systems studied in the Milky Way galaxy. We explored the evolutionary stage of OGLE05155332-6925581. We find the system in a semidetached configuration and at a stage of rapid mass transfer with an age of 476 million years. This evolutionary stage is consistent with the reported existence of a circumprimary accretion disc. On the other hand, we speculate that mass outflows through the Lagrange L_2 and L_3 points, could extract angular momentum from the system in order to balance the mass exchange and produce a relatively constant orbital period, even at high mass transfer rate regimes. Another important part is that, our studies indicate that the DPV phenomenon is observed at different evolutionary stages: Case A for V393 Sco and DQ Vel and Case B for OGLE 05155332-6925581 and AU Mon, but always during or after a main mass transfer burst.

Finally, we have found a photometrically variable object in the Large Magellanic Cloud showing interesting photometric and spectroscopic properties. The chemical analysis that was carried out in this thesis, based on high-resolution spectra confirmed the post-AGB status of ELHC 10, which was until now uncertain. From this and other analyses discussed in Chapter 4, we have shown that ELHC 10 is a long-period binary system consisting of a post-AGB star and an unseen, unevolved B-type companion surrounded by a large and geometrically thick disc.

On the other hand, the prominent stationary Hα double emission line, disclose an stable Keplerian disc, which from the peak separation, must be puffed-up to cover a large opening angle for the central star and was formed by binary star interaction and outflows through the outer Lagrangian points. This post-AGB system did not evolve on single star evolutionary tracks and it must have suffered a phase of strong interaction with the companion while the primary star was a giant. This is very important, since hitherto the process of the formation of stable Keplerian disks in post-AGB stars is not well understood.

In addition, we found many types of peculiarities, splitting, asymmetries and discrete absorption components displaced from their parent metallic lines. The effect is maximal in the iron lines whose profiles are split into two or three components, which can be interpreted as evidence for gas streams, one carrying material from the primary onto the circumstellar disc and the other bringing material from the system into the circumbinary disc. This scenario is consistent with the Roche-lobe overflow, the present of a large thick disc surrounding the secondary star, which possibly cannot accumulate more mass. Another possible explanation given by Gorlova et al. (2015), for these characteristics in the line profiles, would be the light of the primary that is reflected off the inner wall of the disc and scattered into our line of sight, which will move in the opposite direction from the star and disappear during the superior conjunction of the giant star, which is very common among post-AGB stars with dusty discs.

Therefore, the global picture which emerges of the third part of this research is that, there are binary stars which are born in a system which is too small to accommodate to a full grown AGB star, which during a phase of strong interaction can form stable and compact Keplerian circumbinary disks, similar to protoplanetary disks around young stellar objects. This is a very important insight, since the disc plays a lead role in the dynamical and chemical evolution of the system. The formation and evolution of such a dusty disc is a fundamental ingre-

dient in the final evolution of binary stars, which open a new avenue to exploring some of the open questions in the evolution of these objects.

5.1 Future work

To end this thesis, we discuss some future work in the fields addressed here. Some projects have already been initiated, while others should be in the near future. We have found interesting science cases that we wish to address with our observations. These observations were obtained with the FLAMES instrument in MEDUSA mode, and within an international collaboration together with the group of Massive stars of the European Southern Observatory (ESO) directed by Dr. Christophe Martayan.

5.1.1 Emission-line stars as tracers of star formation episodes

We started an extensive multi-wavelength study, including radial velocity monitoring, high-spectral resolution optical and infrared studies of 250 emission-line stars in two fields of SGS complex 6 using VLT-FLAMES observations, see Fig. 5.1. The principal motivation in this complementary research is to determine accurate spectral types for these stars and detect massive binary systems via variations in their radial velocities. From this, we will investigate their nature and we will examine in detail the local environment where they are found. Thereby, we will obtain clear information about whether different patterns and histories of star formation in this SGS complex. A close examination will give us the information, where the actual star formation is triggered by the advancing of the local ionization fronts or whether, the compression mechanisms may take place, showing if the very young ELS are predominantly located in a region around the expanding SGS irradiated by photo-ionization from the cluster with H II regions, as expected in the age-spatial segregation scenario in the NGC 1850 region. Clearly, to get a full comprehension of the atmospheric structure and dust species in the discs of these ELS sample, the second-generation VLT instrument (available in 2017-2020), will bring a better coverage in the medium infrared range, which will provide observational constraints of unprecedented detail.

5.1.2 Long-term variability in LMC-DPV system

We need recall that DPVs system show two linked photometric variabilities: a short-term modulation which is related to the orbital motion of the binary and a second observed long-term variability which is redder, not strictly constant and whose origin is uncertain. We need to gather data covering several long-term cycles to investigate the nature of the enigmatic long-term periodicity observed in OGLE05155332−6925581. Previous studies in V393 Sco, DQ Vel and AU Mon along their long-term cycles, indicate that the source of the enigmatic long-term variability is not related to physical changes in the stars or in the accretion discs and must be restricted to a region above/below the orbital plane. This scenario is supported by the fact that the non-orbital variabilities found in the V393 Sco, DQ Vel and AU Mon spectra are dependent on the long-term phase (Mennickent et al. 2012b; Barría et al. 2014). Additional to this, Balmer emission strenght in V393 Sco and DQ Vel, increases at the high state and the central absorption decreases. Two scenarios support this variability pattern: an extra emission taking place at the high state of the system such as a wind whose intensity can be modulated with the long-term variability, or an attenuation of the total light of the system at the minimum of the long-term periodicity, for instance by some kind of periodic mass loss episodes. We cannot exclude that both mechanisms can indeed operate together as is the case for OGLE05155332−6925581 discussed in Chapter 3. For these reasons we need to continue investigating this system.

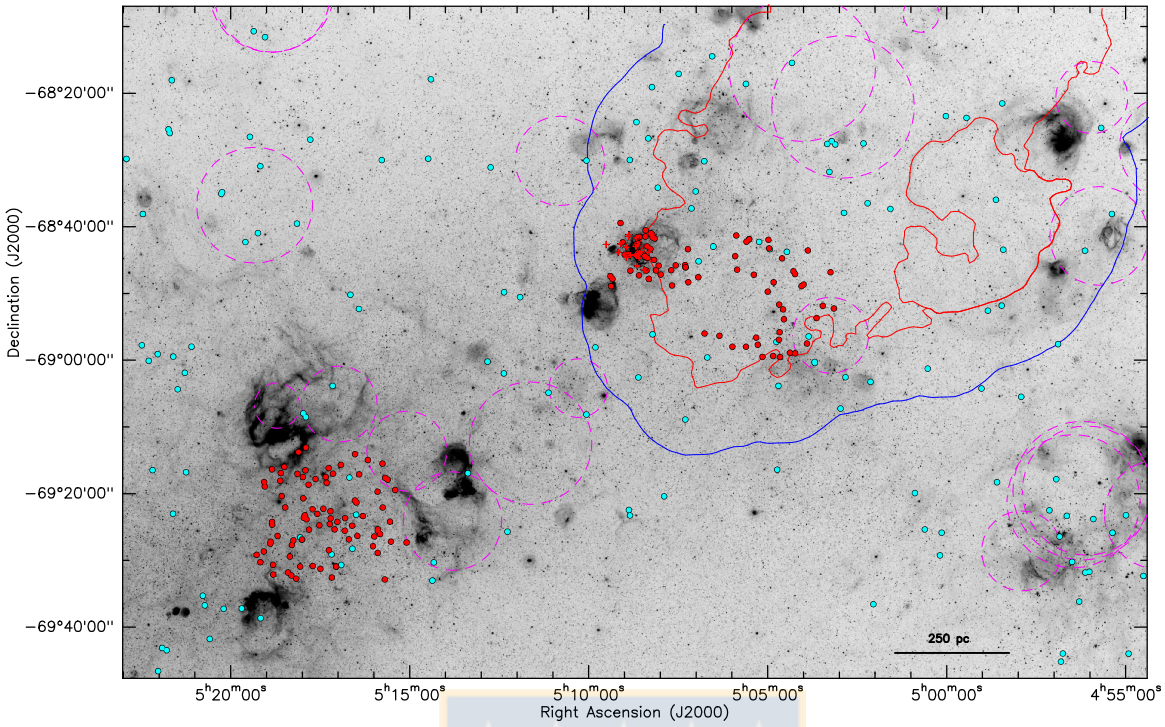

Figure 5.1: The red points are ELS's around of the SGS complex 6 and their background zone with multi-epoch optical spectra obtained by us, the green point are ELS's from Reid & Parker (2012). SGS complex 6 is overlaid on MCELS Hα image. Dashed circles are the H I "giant shells" from Kim et al. (1999) . North is up, east to the left.

5.1.3 Binary post-AGB stars

We have seen that ELHC 10 is an interacting post-AGB binary with many characteristics for further study. A more detailed study is necessary, especially we must have long-term observations at high angular resolutions, which will help us to clarify the relation between the characteristics and evolution of the circumbinary and circumstellar environment in ELHC 10. Also, we have chosen 70 post-AGB objects with spectral energy distributions compatible with circumbinary Keplerian passive discs, considering the catalog of de Ruyter et al. (2006) and the further extensions for the LMC and SMC given by van Aarle et al. (2011) and Kamath et al. (2014). All these objects show SEDs displaying large IR excess with dust excess starting near sublimation temperature, irrespective of the temperature of the central star. When there is long wavelength data available, these objects show a second bump in their SEDs, indicative of larger sized grains. These objects have been interpreted as binaries, but this needs confirmation by a long-term study of radial velocities. In particular we are interested in their RV behavior during the orbital cycle, determining if they can be used as diagnostics for outflowing gas streams connecting the binary system with the circumbinary disc through the outer Lagrangian points, as we proposed for ELHC10. Hence we will establish if binary interaction and mass outflows can be invoked as the general cause for the circumbinary discs detected in post-AGB stars. We will perform a systematic, chemical study of post-AGB binaries. The combination of the deduced abundance patterns, and the position of the objects in the HR diagram will allow for unprecedented, direct tests regarding this evolutionary phase. The low metallicity of the Magellanic Clouds ensures that non- LTE effects have to be taken into account when determining the abundance patterns to reduce the errors on the obtained values. This part still needs to be investigated. Additionally, an abundance analysis of these objects will allow testing of the poorly understood binary evolution channels, although the direct proof of the high binarity rate will be an observational moni-

toring challenge. The ultimate goal of this project is to make significant progress in our understanding of the associated s-process nucleosynthesis, and to better comprehend the evolution of binary post-AGB stars.

Appendix A

The model of the accretion disc

The basic elements of the binary system model with a plane-parallel accretion disc and the corresponding light-curve synthesis procedure are described in detail in Djurašević (1992, 1996). The disc is geometrically and optically thick and its edge is approximated by a cylindrical surface. In the current version of the model (Djurašević et al. 2008), the thickness of the disc can change linearly with radial distance, allowing the disc to take a conical shape (that can be convex, concave or plane-parallel). The geometrical properties of the disc are determined by its radius (R_d), its thickness at the edge (d_e) and the thickness at the center (d_c). This way of approximating the shape of the accretion disc is justified by the current hydrodynamical modeling of mass transfer in close binary systems - (see, e.g., Bisikalo et al. 2000; Harmanec et al. 2002; Nazarenko & Glazunova 2003, 2006a,b).

The cylindrical edge of the disc is characterized by its temperature, T_d, and the conical surface of the disc by the radial temperature distribution of the α-disc (Frank et al. 2002):

$$T(r) = T_d \left[\frac{R_d}{r}\right]^{a_T}. \tag{A.1}$$

or also, assuming that the disc is in physical and thermal contact with the gainer, so the inner radius and temperature of the disc are equal to the temperature and radius of the star ($\mathcal{R}_h$, T_h). In this way, we can describe the temperature distribution by the following law given by (Djurašević et al. 2008):

$$T(r) = T_d + (T_h - T_d)\left[1 - \left(\frac{r - R_h}{R_d - R_h}\right)^{a_T}\right] \tag{A.2}$$

The temperature of the disc at the edge (T_d) and the temperature exponent (a_T), as well as the radii of the star (R_h) and the disc (R_d) are free parameters, determined by solving the inverse problem.

The model of the binary can be refined by introducing active regions on the edge of the accretion disc. The active regions have higher local temperatures so their inclusion results in a non-uniform distribution of radiation. The existence of such regions (hot and bright spots), can be explained by the gas dynamics of interacting binaries - (see, e.g., Heemskerk 1994; Bisikalo et al. 1998, 2000, 2005; Harmanec et al. 2002; Nazarenko & Glazunova 2003, 2006a,b). Based on these investigations of systems with accretion discs, we recently updated our model to allow inclusion of up to three such active regions: the hot spot (hs) and two bright spots (bs1 and bs2). Including active regions in the model leads to significant improvements in the quality of the fit to observations.

These regions are characterized by the following parameters: $A_{hs,bs} = T_{hs,bs} / T_d$ - the hot and bright spot temperature coefficients, $\theta_{hs,bs}$ and $\lambda_{hs,bs}$ - the spot's angular dimensions and longitudes (in arc degrees) and θ_{rad} -

the angle between the line perpendicular to the local disc edge surface and the direction of the hot spot's maximum radiation. The longitude λ is measured clockwise (as viewed from the direction of the +Z-axis, which is orthogonal to the orbital plane) with respect to the line connecting the star centers (+X-axis), in the range 0 – 360 degrees (see Djurašević et al. 2010, for more details). These parameters are also determined by solving the inverse problem.

The hot spot in our model is a rough approximation of the 'hot line" which forms at the edge of the gas stream flowing from the donor to the disc (Bisikalo et al. 2003). Due to the infall of an intensive gas stream, the disc surface in the region of the hot spot becomes deformed as the material accumulates at the point of impact, producing a local distribution of radiation which deviates from the uniform azimuthal distribution. In the model, this deviation is described by the angle $\theta_{\rm rad}$. Depending on $\theta_{\rm rad}$, the maximum of the hot spot flux can be slightly shifted in the orbital phase, changing the light-curve asymmetry around the secondary maximum and in the region of the primary minimum.

One possible limitation of the code at its present implementation is the lack of a detailed treatment for the donor irradiation by the disc part facing the donor, including hotspot. This effect could be potentially important in close binaries with a large difference in stellar and disc temperatures. However, it should be a second-order effect compared with the stellar and disc flux contributions (including donor irradiation by the gainer) already implemented in the code. This is demonstrated in the very good fit obtained with the orbital multiwavelength light curves in Chapters 3 and 4.

Bibliography

Akashi, M. & Soker, N. 2008, New Astronomy, 13, 157

Alcock, C., Allsman, R. A., Alves, D. R., Axelrod, & MACHO Collaboration. 1999, PASP, 111, 1539

Alves, D. R. 2004, NewAR, 48, 659

Ansari, R. & EROS Collaboration. 2001, in Astronomical Society of the Pacific Conference Series, Vol. 237, Gravitational Lensing: Recent Progress and Future Go, ed. T. G. Brainerd & C. S. Kochanek, 235

Baade, D., Meisenheimer, K., Iwert, O., et al. 1999, The Messenger, 95, 15

Badenes, C., Hughes, J. P., Bravo, E., & Langer, N. 2007, ApJ, 662, 472

Bagnulo, S., Jehin, E., Ledoux, C., et al. 2003, The Messenger, 114, 10

Barría, D., Mennickent, R. E., Graczyk, D., & Kołaczkowski, Z. 2014, A&A, 567, A140

Barría, D., Mennickent, R. E., Schmidtobreick, L., et al. 2013, A&A, 552, A63

Bayo, A., Rodrigo, C., Barrado Y Navascués, D., et al. 2008, A&A, 492, 277

Benacquista, M. J. & Downing, J. M. B. 2013, Living Reviews in Relativity, 16, 4

Bertin, E. & Arnouts, S. 1996, A&AS, 117, 393

Bessell, M. S. & Brett, J. M. 1988, PASP, 100, 1134

Bisikalo, D. V., Boyarchuk, A. A., Chechetkin, V. M., Kuznetsov, O. A., & Molteni, D. 1998, MNRAS, 300, 39

Bisikalo, D. V., Boyarchuk, A. A., Kaigorodov, P. V., & Kuznetsov, O. A. 2003, Astron. Rep., 47, 809

Bisikalo, D. V., Harmanec, P., Boyarchuk, A. A., Kuznetsov, O. A., & Hadrava, P. 2000, A&A, 353, 1009

Bisikalo, D. V., Kaigorodov, P. V., Boyarchuk, A. A., & Kuznetsov, O. A. 2005, Astronomy Reports, 49, 701

Bohannan, B. & Epps, H. W. 1974, A&AS, 18, 47

Book, L. G., Chu, Y.-H., Gruendl, R. A., & Fukui, Y. 2009, AJ, 137, 3599

Bujarrabal, V., Castro-Carrizo, A., Alcolea, J., & Van Winckel, H. 2015, A&A, 575, L7

Carrera, R., Gallart, C., Aparicio, A., & Hardy, E. 2011, AJ, 142, 61

Carrera, R., Gallart, C., Hardy, E., Aparicio, A., & Zinn, R. 2008, AJ, 135, 836

Castelli, F. & Hubrig, S. 2004, A&A, 425, 263

Catelan, M. 2009, Ap&SS, 320, 261

Cardelli, J. A., Clayton, G. C., & Mathis, J. S. 1989, ApJ, 345, 245

Cignoni, M., Tosi, M., Sabbi, E., Nota, A., & Gallagher, J. S. 2011, AJ, 141, 31

Cioni, M.-R., Loup, C., Habing, H. J., et al. 2000, A&AS, 144, 235

Claret, A. 2004, A&A, 424, 919

Coelho, P., Barbuy, B., Meléndez, J., Schiavon, R. P., & Castilho, B. V. 2005, A&A, 443, 735

Cox, D. P. & Smith, B. W. 1974, ApJL, 189, L105

Dachs, J., Kiehling, R., & Engels, D. 1988, A&A, 194, 167

Dawson, J. R., McClure-Griffiths, N. M., Wong, T., et al. 2013, ApJ, 763, 56

de Mink, S. E., Pols, O. R., & Glebbeek, E. 2007, in American Institute of Physics Conference Series, Vol. 948, Unsolved Problems in Stellar Physics: A Conference in Honor of Douglas Gough, ed. R. J. Stancliffe, G. Houdek, R. G. Martin, & C. A. Tout, 321–325

de Mink, S. E., Sana, H., Langer, N., Izzard, R. G., & Schneider, F. R. N. 2014, ApJ, 782, 7

De Ruyter, S. 2005, PhD thesis, Institute of Astronomy, Katholieke Universiteit Leuven, Belgium

de Ruyter, S., van Winckel, H., Dominik, C., Waters, L. B. F. M., & Dejonghe, H. 2005, A&A, 435, 161

de Ruyter, S., van Winckel, H., Maas, T., et al. 2006, A&A, 448, 641

De Smedt, K., Van Winckel, H., Karakas, A. I., et al. 2012, A&A, 541, A67

de Vaucouleurs, G. & Freeman, K. C. 1972, Vistas in Astronomy, 14, 163

de Wit, W. J., Beaulieu, J. P., & Lamers, H. J. G. L. M. 2002, A&A, 395, 829

de Wit, W. J., Beaulieu, J. P., Lamers, H. J. G. L. M., Coutures, C., & Meeus, G. 2005, A&A, 432, 619

Dennis, J. E., Jr., & Torczon, V. 1991, SIAM Journal on Optimization, 1, 448

Desmet, M., Frémat, Y., Baudin, F., et al. 2010, MNRAS, 401, 418

Diago, P. D., Gutiérrez-Soto, J., Fabregat, J., & Martayan, C. 2008, A&A, 480, 179

Djurašević, G. 1992, Ap&SS, 196, 267

Djuraševic, G. 1992, Ap&SS, 197, 17

Djurašević, G. 1996, Ap&SS, 240, 317

Djurašević, G., Latković, O., Vince, I., & Cséki, A. 2010, MNRAS, 409, 329

Djurašević, G., Vince, I., Antokhin, I. I., et al. 2012, MNRAS, 420, 3081

Djurašević, G., Vince, I., & Atanacković, O. 2008, AJ, 136, 767

Djurašević, G., Yılmaz, M., Baştürk, Ö., et al. 2011, A&A, 525, A66

Dong, S., Katz, B., Prieto, J. L., et al. 2014, ApJ, 788, 41

Dougherty, S. M., Waters, L. B. F. M., Burki, G., et al. 1994, A&A, 290, 609

Dufton, P. L., Langer, N., Dunstall, P. R., et al. 2013, A&A, 550, A109

Duquennoy, A. & Mayor, M. 1991, A&A, 248, 485

Eggleton, P. 2006, Evolutionary Processes in Binary and Multiple Stars

Ekström, S., Meynet, G., Maeder, A., & Barblan, F. 2008, A&A, 478, 467

Elmegreen, B. G. 1998, in Astronomical Society of the Pacific Conference Series, Vol. 148, Origins, ed. C. E. Woodward, J. M. Shull, & H. A. Thronson, Jr., 150

Evans, C. J., Taylor, W. D., Hénault-Brunet, V., et al. 2011, A&A, 530, A108

Fischer, P., Welch, D. L., & Mateo, M. 1993, AJ, 105, 938

Fitzpatrick, E. L. 1986, AJ, 92, 1068

Frank, J., King, A., & Raine, D. J. 2002, Accretion Power in Astrophysics: Third Edition

Frankowski, A. & Jorissen, A. 2007, Baltic Astronomy, 16, 104

Garrido, H. E., Mennickent, R. E., Djurašević, G., et al. 2013, MNRAS, 428, 1594

Georgy C., Ekström S., Granada A., Meynet G., Mowlavi N., Eggenberger P., Maeder A., 2013, A&A, 553, A24

Gielen, C., van Winckel, H., Min, M., Waters, L. B. F. M., & Lloyd Evans, T. 2008, A&A, 490, 725

Gielen, C., van Winckel, H., Reyniers, M., et al. 2009, A&A, 508, 1391

Gilmozzi, R., Kinney, E. K., Ewald, S. P., Panagia, N., & Romaniello, M. 1994, ApJL, 435, L43

Goodricke, J. 1783, Royal Society of London Philosophical Transactions Series I, 73, 474

Gorlova, N., Van Winckel, H., Gielen, C., et al. 2012, A&A, 542, A27

Gorlova, N., Van Winckel, H., Ikonnikova, N. P., et al. 2015, MNRAS, 451, 2462

Grison, P., Beaulieu, J.-P., Pritchard, J. D., Tobin, W., & Ferlet. 1995, A&AS, 109, 447

Gruendl, R. A. & Chu, Y.-H. 2009, ApJS, 184, 172

Habing, H. J. & Olofsson, H., eds. 2003, Asymptotic giant branch stars

Harmanec, P., Bisikalo, D. V., Boyarchuk, A. A., & Kuznetsov, O. A. 2002, A&A, 396, 937

Harris, J. & Zaritsky, D. 2009, AJ, 138, 1243

Hauschildt, P. H., Allard, F., & Baron, E. 1999, ApJ, 512, 377

Heemskerk, M. H. M. 1994, A&A, 288, 807

Henize, K. G. 1956, ApJS, 2, 315

Hennekemper, E., Gouliermis, D. A., Henning, T., Brandner, W., & Dolphin, A. E. 2008, ApJ, 672, 914

Herbst, W. & Shevchenko, V. S. 1999, AJ, 118, 1043

Hernández, J., Calvet, N., Hartmann, L., et al. 2005, AJ, 129, 856

Herwig, F. 2005, ARA&A, 43, 435

Hilditch, R. W. 2001, An Introduction to Close Binary Stars

Hillen, M., de Vries, B. L., Menu, J., et al. 2015, A&A, 578, A40

Hillen, M., Menu, J., Van Winckel, H., et al. 2014, A&A, 568, A12

Hillen, M., Verhoelst, T., Van Winckel, H., et al. 2013, A&A, 559, A111

Höfner, S. 2009, in Astronomical Society of the Pacific Conference Series, Vol. 414, Cosmic Dust - Near and Far, ed. T. Henning, E. Grün, & J. Steinacker, 3

Huang, W. & Gies, D. R. 2006, ApJ, 648, 580

Humphreys, R. M., Davidson, K., Grammer, S., et al. 2013, ApJ, 773, 46

Iqbal, S. & Keller, S. C. 2013, MNRAS, 435, 3103

Jorissen, A. 2003, in Asymptotic giant branch stars, by Harm J. Habing and Hans Olofsson. Astronomy and astrophysics library, New York, Berlin: Springer, 2003, p. 461, ed. H. J. Habing & H. Olofsson, 461

Jorissen, A., Frankowski, A., Famaey, B., & van Eck, S. 2009, A&A, 498, 489

Kamath, D., Wood, P. R., & Van Winckel, H. 2014, MNRAS, 439, 2211

Kato, D., Nagashima, C., Nagayama, T., et al. 2007, PASJ, 59, 615

Kim, S., Chu, Y.-H., Staveley-Smith, L., & Smith, R. C. 1998, ApJ, 503, 729

Kim, S., Dopita, M. A., Staveley-Smith, L., & Bessell, M. S. 1999, AJ, 118, 2797

Kitchin, C. R. 2004, Astronomy Now, 18, 24

Klochkova, V. G. 2013, Astronomy Letters, 39, 765

Klochkova, V. G. 2015, ArXiv e-prints[[arXiv]1502.06705]

Kovtyukh, V. V. 2007, MNRAS, 378, 617

Kurucz, R. 1993, SYNTHE Spectrum Synthesis Programs and Line Data. Kurucz CD-ROM No. 18. Cambridge, Mass.: Smithsonian Astrophysical Observatory, 1993., 18

Lambert, D. L., Hinkle, K. H., & Luck, R. E. 1988, ApJ, 333, 917

Lamers, H. J. G. L. M., Beaulieu, J. P., & de Wit, W. J. 1999, A&A, 341, 827

Landau, L. D. & Lifshitz, E. M. 1962, The Classical Theory of Field

Landolt, A. U. 1983, AJ, 88, 439

Landolt, A. U. 1992, AJ, 104, 340

Lang, K. R. 1992, Science, 257, 1148

Laval, A., Rosado, M., Boulesteix, J., et al. 1992, A&A, 253, 213

Lejeune, T. & Schaerer, D. 2001, A&A, 366, 538

Lenz, P. & Breger, M. 2005, Communications in Asteroseismology, 146, 53

Lewis, K. T., Burrows, D. N., Hughes, J. P., et al. 2003, ApJ, 582, 770

Livio, M. & Soker, N. 1988, ApJ, 329, 764

Luck, R. E., Bond, H. E., & Lambert, D. L. 1990, ApJ, 357, 188

Lucy, L. B. 1967, Zeitschrift für Astrophysik, 65, 89

Maeder, A. 1987, A&A, 178, 159

Maeder, A. & Meynet, G. 2001, A&A, 373, 555

Martayan, C., Baade, D., & Fabregat, J. 2010a, A&A, 509, A11

Martayan, C., Baade, D., & Fabregat, J. 2010b, The Messenger, 139, 29

Martayan, C., Baade, D., Hubert, A.-M., et al. 2008, in 2007 ESO Instrument Calibration Workshop, ed. A. Kaufer & F. Kerber, 595

Martayan, C., Zorec, J., Frémat, Y., & Ekström, S. 2010c, A&A, 516, A103

Martínez González, M. J., Asensio Ramos, A., Manso Sainz, R., Corradi, R. L. M., & Leone, F. 2015, A&A, 574, A16

Martins, F., Hillier, D. J., Bouret, J. C., et al. 2009, A&A, 495, 257

Mashonkina, L., Gehren, T., Shi, J.-R., Korn, A. J., & Grupp, F. 2011, A&A, 528, A87

Massey, P. 2002, ApJS, 141, 81

Mastrodemos, N. & Morris, M. 1998, ApJ, 497, 303

Mastrodemos, N. & Morris, M. 1999, ApJ, 523, 357

Mathis, J. S. & Lamers, H. J. G. L. M. 1992, A&A, 259, L39

McCray, R. & Kafatos, M. 1987, ApJ, 317, 190

McKee, C. F. & Ostriker, J. P. 1977, ApJ, 218, 148

Meaburn, J. 1980, MNRAS, 192, 365

Meixner, M., Gordon, K. D., Indebetouw, R., et al. 2006, AJ, 132, 2268

Mennickent, R. E. 2014, PASP, 126, 821

Mennickent, R. E., Assmann, P., Pietrzyński, G., & Gieren, W. 2005, in Astronomical Society of the Pacific Conference Series, Vol. 335, The Light-Time Effect in Astrophysics: Causes and cures of the O-C diagram, ed. C. Sterken, 129

Mennickent, R. E., Djurašević, G., Cabezas, M., et al. 2015, ArXiv e-prints[[arXiv]1501.04532]

Mennickent, R. E., Djurašević, G., Kołaczkowski, Z., & Michalska, G. 2012a, MNRAS, 421, 862

Mennickent, R. E., Kołaczkowski, Z., Djurasevic, G., et al. 2012b, MNRAS, 427, 607

Mennickent, R. E., Kołaczkowski, Z., Graczyk, D., & Ojeda, J. 2010a, MNRAS, 405, 1947

Mennickent, R. E., Kołaczkowski, Z., Michalska, G., et al. 2008, MNRAS, 389, 1605

Mennickent, R. E., Pietrzyński, G., Diaz, M., & Gieren, W. 2003, A&A, 399, L47

Mennickent, R. E., Pietrzyński, G., Gieren, W., & Szewczyk, O. 2002, A&A, 393, 887

Mennickent, R. E. & Rosales, J. 2014, Information Bulletin on Variable Stars, 6116, 1

Mennickent, R. E. & Smith, M. A. 2010, MNRAS, 407, 734

Mennickent, R. E., Smith, M. A., Kołaczkowski, Z., Pietrzyński, G., & Soszyński, I. 2010b, PASP, 122, 662

Meschin, I., Gallart, C., Aparicio, A., et al. 2014, MNRAS, 438, 1067

Meyer, M. R., Calvet, N., & Hillenbrand, L. A. 1997, AJ, 114, 288

Nazarenko, V. V. & Glazunova, L. V. 2003, Astronomy Reports, 47, 1013

Nazarenko, V. V. & Glazunova, L. V. 2006a, Astronomy Reports, 50, 369

Nazarenko, V. V. & Glazunova, L. V. 2006b, Astronomy Reports, 50, 380

Oestreicher, M. O. & Schmidt-Kaler, T. 1996, A&AS, 117, 303

Packet, W. 1981, A&A, 102, 17

Palmer, D. M. 2009, ApJ, 695, 496

Pfahl, E.; Rappaport S, Podsiadlowski P; Spruit H., 2002, ApJ, 574, 364

Pereira, C. B. & Miranda, L. F. 2007, A&A, 462, 231

Peters, G. J. 1994, in Astronomical Society of the Pacific Conference Series, Vol. 56, Interacting Binary Stars, ed. A. W. Shafter, 384

Petrie, R. M. 1960, Annales d'Astrophysique, 23, 744

Pietrzyński, G., Graczyk, D., Gieren, W., et al. 2013, Nature, 495, 76

Podsiadlowski, P. & Joss, P. C. 1989, Nature, 338, 401

Podsiadlowski, P., Joss, P. C., & Hsu, J. J. L. 1992, ApJ, 391, 246

Poeckert, R. & Marlborough, J. M. 1979, ApJ, 233, 259

Poleski, R., Soszyński, I., Udalski, A., et al. 2010, Acta Astron., 60, 179

Pompéia, L., Hill, V., Spite, M., et al. 2008, A&A, 480, 379

Porter, J. M. & Rivinius, T. 2003, PASP, 115, 1153

Poveda, A., Allen, C., & Parrao, L. 1982, ApJ, 258, 589

Press, W. H., Teukolsky, S. A., Vetterling, W. T., & Flannery, B. P. 1992, Numerical recipes in FORTRAN. The art of scientific computing

Rafert, J. B. & Twigg, L. W. 1980, MNRAS, 193, 79

Rappaport, S., Verbunt, F., & Joss, P. C. 1983, ApJ, 275, 713

Rattenbury, N. J., Wyrzykowski, Ł., Kostrzewa-Rutkowska, Z., et al. 2015, MNRAS, 447, L31

Reid, W. A. & Parker, Q. A. 2012, MNRAS, 425, 355

Rivinius, T. and Carciofi, A. C. and Martayan, C. 2013, A&ARv, 21, 69

Rest, A., Suntzeff, N. B., Olsen, K., et al. 2005, Nature, 438, 1132

Sabbi, E., Lennon, D. J., Gieles, M., et al. 2012, ApJL, 754, L37

Sabogal, B. E., Mennickent, R. E., Pietrzyński, G., & Gieren, W. 2005, MNRAS, 361, 1055

Sbordone, L. 2005, Memorie della Societa Astronomica Italiana Supplementi, 8, 61

Selman, F., Melnick, J., Bosch, G., & Terlevich, R. 1999, A&A, 347, 532

Skrutskie, M. F., Cutri, R. M., Stiening, R., Weinberg, M. D., & Schneider. 2006, AJ, 131, 1163

Smith, R. C. & MCELS Team. 1999, in IAU Symposium, Vol. 190, New Views of the Magellanic Clouds, ed. Y.-H. Chu, N. Suntzeff, J. Hesser, & D. Bohlender, 28

Sneden, C. A. 1973, PhD thesis, THE UNIVERSITY OF TEXAS AT AUSTIN.

Soberman, G. E., Phinney, E. S., & van den Heuvel, E. P. J. 1997, A&A, 327, 620

Soszyński, I., Udalski, A., Szymański, M. K., et al. 2009, Acta Astron., 59, 239

Stellingwerf, R. F. 1978, ApJ, 224, 953

Sytov, A. Y., Kaigorodov, P. V., Bisikalo, D. V., Kuznetsov, O. A., & Boyarchuk, A. A. 2007, Astronomy Reports, 51, 836

Szczerba, R. & Górny, S. K., eds. 2001, Astrophysics and Space Science Library, Vol. 265, Post-AGB Objects as a Phase of Stellar Evolution

Szymanski, M. & Udalski, A. 1993, Acta Astron., 43, 91

Szymanski, M. K. 2005, Acta Astron., 55, 43

Taylor, M. 2011, STILTS: Starlink Tables Infrastructure Library Tool Set, Astrophysics Source Code Library

Terlevich, E. 1987, MNRAS, 224, 193

Thomas, J. D. 2012, PhD thesis, The University of Toledo

Tokovinin, A. A. 1997, A&AS, 124, 75

Udalski, A., Kubiak, M., & Szymanski, M. 1997, Acta Astron., 47, 319

Udalski, A., Paczynski, B., Zebrun, K., et al. 2002, Acta Astron., 52, 1

Udalski, A., Szymanski, M., Kubiak, M., et al. 2000, Acta Astron., 50, 307

Udalski, A., Szymanski, M., Kubiak, M., et al. 1998a, Acta Astron., 48, 1

Udalski, A., Szymanski, M., Kubiak, M., et al. 1998b, Acta Astron., 48, 147

Udalski, A., Szymanski, M. K., Soszynski, I., & Poleski, R. 2008, Acta Astron., 58, 69

van Aarle, E., Van Winckel, H., De Smedt, K., Kamath, D., & Wood, P. R. 2013, A&A, 554, A106

van Aarle, E., van Winckel, H., Lloyd Evans, T., et al. 2011, A&A, 530, A90

van der Marel, R. P., Alves, D. R., Hardy, E., & Suntzeff, N. B. 2002, AJ, 124, 2639

Van der Swaelmen, M., Hill, V., Primas, F., & Cole, A. A. 2013, A&A, 560, A44

van Rensbergen, W., De Greve, J. P., De Loore, C., & Mennekens, N. 2008a, A&A, 487, 1129

van Rensbergen, W., De Greve, J. P., De Loore, C., & Mennekens, N. 2008b, VizieR Online Data Catalog, 348, 71129

van Rensbergen, W., de Greve, J. P., Mennekens, N., Jansen, K., & de Loore, C. 2011, A&A, 528, A16

van Winckel, H. 2003, ARA&A, 41, 391

Van Winckel, H. 2007, Baltic Astronomy, 16, 112

Van Winckel, H., Mathis, J. S., & Waelkens, C. 1992, Nature, 356, 500

Van Winckel, H., Waelkens, C., & Waters, L. B. F. M. 1995, A&A, 293, L25

van't Veer, F. & Maceroni, C. 1992, In Binaries as Tracers of Stellar Formation

Vassiliadis, E. & Wood, P. R. 1994, ApJS, 92, 125

Venn, K. A. & Lambert, D. L. 1990, ApJ, 363, 234

Ventura, P., Karakas, A. I., Dell'Agli, F., et al. 2015, MNRAS, 450, 3181

von Zeipel, H. 1924, MNRAS, 84, 702

Wade, R. A. & Horne, K. 1988, ApJ, 324, 411

Waelkens, C., Van Winckel, H., Waters, L. B. F. M., & Bakker, E. J. 1996, A&A, 314, L17

Walborn, N. R., Maíz-Apellániz, J., & Barbá, R. H. 2002, AJ, 124, 1601

Wallace, P. T. & Gray, N. 2003, Starlink User Note, 5

Waters, L. B. F. M., Trams, N. R., & Waelkens, C. 1992, A&A, 262, L37

Watson, C. A., Dhillon, V. S., Rutten, R. G. M., & Schwope, A. D. 2003, MNRAS, 341, 129

Wisniewski, J. P. & Bjorkman, K. S. 2006, ApJ, 652, 458

Witt, A. N., Vijh, U. P., Hobbs, L. M., et al. 2009, ApJ, 693, 1946

Wong, T., Hughes, A., Ott, J., et al. 2011, ApJS, 197, 16

Wood, P. R. & Zarro, D. M. 1981, ApJ, 247, 247

Wright, E. L., Eisenhardt, P. R. M., Mainzer, A. K., et al. 2010, AJ, 140, 1868

Yamaguchi, R., Mizuno, N., Onishi, T., Mizuno, A., & Fukui, Y. 2001a, ApJL, 553, L185

Yamaguchi, R., Mizuno, N., Onishi, T., Mizuno, A., & Fukui, Y. 2001b, PASJ, 53, 959

Yoon, S.-C., Langer, N., & Norman, C. 2006, A&A, 460, 199

Zacharias, N., Urban, S. E., Zacharias, M. I., et al. 2004, AJ, 127, 3043

Zaritsky, D., Harris, J., Thompson, I. B., & Grebel, E. K. 2004, AJ, 128, 1606

Zorec, J., Frémat, Y., Martayan, C., Cidale, L. S., & Torres, A. F. 2007, in Astronomical Society of the Pacific Conference Series, Vol. 361, Active OB-Stars: Laboratories for Stellare and Circumstellar Physics, ed. A. T. Okazaki, S. P. Owocki, & S. Stefl, 539